Performance Studies of Multifunctional Pt/Pd Monolithic Catalysts for Hydrocarbon Oxidation Emission Control

A Dissertation

Presented to

the Faculty of the Department of Chemical and Biomolecular Engineering

University of Houston

In Partial Fulfillment

of the Requirements for the Degree

Doctor of Philosophy

in Chemical Engineering

By

Gregory S. Bugosh

May 2015

Performance Studies of Multifunctional Pt/Pd Monolithic Catalysts for Hydrocarbon Oxidation Emission Control

Gregory S. Bugosh

Approved:

Chair of the Committee
Dr. Michael P. Harold
Professor and Chair
Chemical and Biomolecular Engineering

Committee Members:

Dr. William S. Epling
Associate Professor
Chemical and Biomolecular Engineering

Dr. Dan Luss
Professor
Chemical and Biomolecular Engineering

Dr. Stanko R. Brankovic
Associate Professor
Electrical and Computer Engineering

Dr. James K. Meen
Research Associate Professor
Department of Chemistry

Dr. Suresh K. Khator, Associate Dean,
Cullen College of Engineering

Dr. Michael P. Harold, Professor and Chair,
Chemical and Biomolecular Engineering

Acknowledgments

First, I would like to thank my advisor Dr. Michael Harold for his support and guidance through the years. I also thank the members of my dissertation committee for their time and feedback: Dr. William Epling, Dr. Dan Luss, Dr. Stanko Brankovic, and Dr. James Meen. I am also thankful for my current and former co-workers at the Texas Center for Clean Engines, Emissions and Fuels (TxCEF).

Thanks are also in order to the City of Houston and the Texas Commission on Environmental Quality (TCEQ) for financial support in the early years of the Texas Diesel Testing and Research Center (now TxCEF). BASF is acknowledged for providing the catalyst samples. The unnamed third party is recognized for the opportunity to test their propriety catalyst formulations and the accompanying financial support. Also, thanks to the University of Houston and the Department of Chemical and Biomolecular Engineering.

I am especially grateful for the love and support I receive from my wife Laura. I also thank my family and friends for providing encouragement.

Performance Studies of Multifunctional Pt/Pd Monolithic Catalysts for Hydrocarbon Oxidation Emission Control

An Abstract

of a

Dissertation

Presented to

the Faculty of the Department of Chemical and Biomolecular Engineering

University of Houston

In Partial Fulfillment

of the Requirements for the Degree

Doctor of Philosophy

in Chemical Engineering

By

Gregory S. Bugosh

May 2015

Abstract

The catalytic aftertreatment of combustion engine exhaust is critically important to their continued use from both environmental and economic standpoints. This dissertation investigates the performance of multifunctional Pt/Pd monolithic oxidation catalysts for hydrocarbon emission control. This is accomplished through several related yet distinct studies.

First, addition of zeolite beta was investigated with aim of improving cold-start performance. Focus was placed on hydrocarbon (HC) storage and light-off behavior. Dodecane (C12) and carbon monoxide (CO) were used as representative pollutants. Individual reactant feeds, co-feeds, and pre-storage experiments provided insight into the effects of additional zeolite on catalyst performance. Increased zeolite loading subsequently increased the C12 storage capacity. The zeolite did not have a notable effect on the light-off behavior for single component feeds. Pre-storing HC had an inhibitory effect on the CO-light-off and the co-feed of C12 and CO increased the CO light-off temperatures even further.

Next, the construction of a spatially resolved capillary-inlet sampling system for in-channel concentration measurements is described. A study on propylene oxidation was conducted and the newly built sampling technique was utilized. A monolith reactor model was used to simulate the propylene oxidation reaction system in terms of effluent conversions and propylene concentration profiles. The model and data show good agreement.

Evaluation of third party proprietary catalysts (oxidation and NSCR) was performed utilizing a more complex feed stream. The performance of these metallic

substrate catalysts was compared to the model Pt/Pd catalyst, followed by additional experiments to develop a more fundamental understanding. For NSCR testing, the optimum O_2 feed to convert both NOx and HC/CO was dependent on temperature. Increased methane conversion at low O_2 feed concentrations prompted further investigation.

Finally, methane oxidation by Pt/Pd monolith was examined over a wide range of temperatures and oxygen feed concentrations. A clockwise hysteresis loop exists in the rich regime consisting of two stable steady-states of methane conversion. The high steady-state conversion branch is eclipsed by multiple higher methane conversion branches that are transient in nature. The methane consumption observed under lean conditions is insensitive to the oxygen concentration and is classical lean methane oxidation on PdO. Spatially resolved capillary-inlet mass spectrometry (SpaciMS) measurements were utilized to reveal oxidation and partial oxidation reaction zones within the monolith catalyst. During operation in the rich regime, a front oxidative zone and downstream partial oxidation/reforming zone co-exist.

Table of Contents

List of Figures

List of Tables

Nomenclature

BEA	Zeolite beta
BET	Brunauer-Emmett-Teller method of measuring surface area
C12	Dodecane
CARB	California Air Resources Board
CNG	Compressed natural gas
CO	Carbon monoxide
CO_2	Carbon dioxide
DOC	Diesel oxidation catalyst
DPF	Diesel particulate filter
EDS	Energy dispersive spectroscopy
EPA	Environmental Protection Agency
FTIR	Fourier transform infrared spectroscopy
GHSV	Gas hourly space velocity
HC	Hydrocarbon
H_2O	Water
LNG	liquefied natural gas
Mass Spec	Mass spectrometer
N_2	Nitrogen
NMHC	Non-methane hydrocarbon
NMOG	Non-methane organic gas
NO	Nitric oxide
NO_2	Nitrogen dioxide
NOx	oxides of nitrogen, including NO and NO_2

NSCR	Non-selective catalytic reduction
NSR	NOx storage and reduction
O_2	Oxygen
Pd	Palladium
PM	Particulate matter
Pt	Platinum
SCR	Selective catalytic reduction
t	time
T_{50}	Temperature at which 50% conversion is attained (light-off)
TCEQ	Texas Commission on Environmental Quality
TEM	Transmission electron microscopy
TxCEF	Texas Center for Clean Engines, Emissions and Fuels
TxLED	Texas Low Emission Diesel
WGS	Water-gas shift

1. Introduction

Energy. Environment. Economics. Collectively these concepts form a triple bottom line that drives much of the world's industrial and research activities, as well as many individuals' personal ambitions. The concepts are also at the motivational root of this dissertation. Fossil fuels and combustion engines continue to dominate the energy and transportation markets. The resulting emissions negatively impact the environment and our health. Large sums of money are at play in a multitude of ways surrounding the current system and the economic implications cannot be ignored.

The United States used 98 quadrillion BTUs (quads) of energy in 2014, of which 80 quads were fossil fuels (petroleum, coal, and natural gas) and only ~10 quads were from renewable sources, according to the U.S. Energy Information Administration (EIA) [1]. The transportation sector is particularly dependent on liquid fuels and is seeking increases in fuel economy in both the light-duty and heavy duty sectors [2, 3]. This focus can potentially impact the emissions controls system design from weight reduction and space minimization standpoints. Ever tightening emission standards [4] and the high cost of the precious metals utilized to catalytically treat the emissions provide continued motivation for research and innovation.

The focus of the work presented here pertains to diesel or lean-burn engines, specifically the aftertreatment of unburned exhaust hydrocarbons by catalytic oxidation. Focus is also turned toward the treatment of methane slip emissions as the use of natural gas as a transportation fuel is expected to grow.

1.1 Diesel

Diesel engines have historically been used in heavy-duty applications, such as long-haul trucks, construction equipment, locomotive engines, and the like due to their high torque, durability, and fuel efficiency. Diesel engines are also gaining in popularity for light-duty applications such as passenger cars. This is especially true in Europe, which can be attributed in part to Europe's higher fuel prices and less strict air pollution regulations which favor diesel use over gasoline (although that is changing with the new, more stringent Euro VI legislation [5]).

Diesel engines burn diesel fuel and utilize compression ignition (i.e. no spark plugs). An indicator of how well the diesel fuel will combust under compression ignition is the cetane number, a measurement of ignition delay (higher number indicated less ignition delay and is generally considered better). Also, essentially all diesel engines used for transportation utilize a turbocharger, making use of the exhaust gas flow to spin a turbine, and the other side of the turbine boosts the air pressure fed to the engine and increases the power and responsiveness of the engine.

Diesel engines are generally more fuel efficient than comparable gasoline engines and also generally produce more torque (but less horsepower). Diesel engines use a higher compression ratio than gasoline engines, so they must be built to withstand higher pressure, which contributes to their increased durability, but this adds cost to their construction. Diesel engines also use excess air, meaning more air than is stoichiometrically required to completely burn the fuel, in order to help burn the fuel completely.

In contrast to diesel engines, gasoline engines (carbureted or fuel injected) add the fuel to the cylinder first, which then gets compressed by the piston, and then the spark plug ignites the fuel. Gasoline engines use nearly the exact amount of air required to burn the fuel, called the stoichiometric ratio. In practice, it is difficult to use the precise amount of air and fuel, so as a result the engine operates by fluctuating back and forth between too much air (fuel lean) and not enough air (fuel rich). Gasoline has an octane number, with higher numbers meaning it can be compressed more without igniting (ignition prior to the spark is undesirable). Performance engines, usually found in sports cars or luxury cars, have higher compression ratios than normal gasoline engines, and require the more expensive higher octane gasoline (premium gasoline). Undesired ignition in the cylinder can damage the engine and is called "knock" due to the characteristic sound.

Cleaning up diesel exhaust is more difficult than gasoline exhaust due to the particulate matter (soot) and also the excess air used (lean combustion). The soot needs to be trapped by a filter, which is then periodically regenerated. The excess air used means there is oxygen remaining in the exhaust, which makes it very difficult to treat NOx emissions, because to convert the NOx to nitrogen (N_2) oxygen must be removed (i.e. a chemical reduction). A gasoline engine can use a 3-way catalytic converter to treat CO, HC, and NOx (the three pollutant types) but a diesel engine needs a DOC to clean the CO and HC, a lean NOx trap (LNT) or selective catalystic reduction (SCR) unit to clean the NOx, and a diesel particulate filter (DPF) to clean the soot.

Diesel engines produce less CO_2 than comparable gasoline engines because they can be more thermodynamically efficient. Additionally, diesel has a higher energy

density than gasoline. Fuel prices have been higher for diesel than gasoline in the U.S. in recent years due to the tax structure and also to the difficult removal of sulfur from the diesel fuel. The sulfur is removed so that it will not burn and generate SOx, which not only is a pollutant in and of itself, but also serves as a poison of the catalysts that carry out the exhaust aftertreatment.

Diesel engines continue to be developed to be more fuel efficient and produce less pollution. New and better materials/techniques make engine components lighter, stronger, and with tighter tolerances, which improves all aspects. Electronics have enabled more complex controls compared to the older mechanical control. Major developments include better fuel injectors that are supplied with higher pressure fuel and the use of multiple fuel injections per combustion event which improves efficiency, reduces pollution, and reduces noise.

1.1.1 DOC and HC control

As engine exhaust emission regulations continue to become more stringent [4], additional technological and economic pressures are placed on original equipment manufacturers. While internal combustion engine technology continues to become cleaner and more efficient, catalytic treatment of the exhaust is still needed and will be for the foreseeable future. The first aftertreatment reactor encountered by diesel engine exhaust is the diesel oxidation catalyst (DOC) [6]. The principal function of the DOC is the efficient, complete oxidation of engine-out carbon monoxide (CO) and unburned hydrocarbons (HCs). Other DOC roles include the oxidation of NO to NO_2, as well as conversion of deliberately-injected supplemental fuel through exothermic reactions for heat generation. These additional functions aid in downstream NOx reduction and

regeneration of the soot filter. The multifunctional nature of the DOC is clearly vital to the successful implementation of the engine aftertreatment system.

The active DOC component is typically a precious group metal (PGM), namely platinum (Pt) and palladium (Pd), which are very effective oxidation catalysts. The DOC operates at very high conversion (>90%) once sufficient exhaust temperatures have been reached. However, challenges remain for low temperature operation. During the "cold start" most of the engine-out hydrocarbons pass through the DOC unreacted and contribute significantly to the total HC measurement during emissions testing. The use of exhaust gas recirculation (EGR), intended to decrease engine-out NOx emissions, may, as a result, increase exhaust HC emissions. New diesel engines designed to produce less thermal NOx can result in lower exhaust temperatures, adding to the challenge. In addition, some new drive cycle tests include periods of low engine load that might lead to the DOC falling below the light-off temperature (quenching) and subsequently resulting in increased hydrocarbon emissions [7]. Looking ahead, emerging advanced combustion strategies will become more common, such as homogeneous charge compression ignition (HCCI), premixed charge compression ignition (PCCI), and reactivity controlled compression ignition (RCCI) [8]. These combustion technologies can decrease NOx and PM emissions while maintaining or improving fuel efficiency, however the HC and CO emissions generally increase, placing additional burden on the DOC. Finally, there is constant need to reduce the required amount of expensive precious metals for cost savings.

One approach to address the low-temperature hydrocarbon emission challenge is to incorporate a zeolitic component into the DOC washcoat. The zeolite serves as a trap

of higher molecular weight hydrocarbons while they are emitted at low temperatures below their catalytic ignition temperature. This transient approach stores the HC until the exhaust temperature increases to a level which causes their release and subsequent oxidation by the now warmer and more active catalyst.

Other cold-start improvement methods include: reducing heat capacity and mass of catalyst, closer placement to engine (but that can reduce catalyst life due to thermal degradation), engine methods – high speed starter, intake air flow (swirl) control, low mass high ignition spark plugs, injection/ignition timing, piston surface shape. The approach to address the low-temperature hydrocarbon emission challenge investigated in the first part of this dissertation (Chapter 2) is to incorporate a zeolitic component into the DOC washcoat. The study explores elements of cold-start hydrocarbon trapping, which can assist, or possibly compromise, the DOC's ability to satisfactorily oxidize the exhaust chemical species.

The HCs contained in real engine exhaust comprise a very complex mixture, so for purposes of conducting research, the synthetic exhaust mixture is simplified to fewer but broader categories of HCs based on shared properties. The main groupings are typically comprised of alkanes (including methane, ethane, propane, etc), olefins (ethylene, propylene), aromatics (benzene, xylene), and aldehydes (formaldehyde, acetaldehyde). Propylene is often selected as the HC of choice when focusing on the lighter, more reactive portion of the exhaust HCs. Propylene typically makes up 5 - 10% of the total HC in real exhaust on a ppm C basis [9–11]. The propylene and other HCs react with NOx in sunlight to produce harmful ozone and smog [12, 13].

1.2 Natural Gas

The use of natural gas (NG) as a transportation fuel in the liquefied (LNG) and compressed (CNG) forms is expected to grow. LNG and CNG vehicles generally have lower emissions of particulate matter (PM), SOx, and non-methane hydrocarbons (NMHC). Unfortunately, methane emissions from natural gas engines are much higher than diesel or gasoline fueled engines. Since methane does not contribute to ozone formation, vehicular emissions regulations have historically excluded methane from the HC limits, instead placing restrictions on NMHCs or non-methane organic gases (NMOG). However, methane is a potent greenhouse gas with a global warming potential more than 20 times that of CO_2 [14]. A consequence of this fact is the expected emergence of more stringent methane emissions regulations in the coming years. For this reason there is renewed interest in the development of improved catalytic converters for NG-powered vehicles.

While most hydrocarbons (HCs) and carbon monoxide (CO) emitted from internal combustion engines are readily abated by noble metal (Pt, Pd) catalyzed oxidation, CH_4 is notoriously non-reactive [15, 16]. Stoichiometric (spark-ignited) NG-powered combustion engines have a comparatively low exhaust concentration of O_2 (< 2%) so the three-way catalyst (TWC) is effective in simultaneously oxidizing CO and NMHC's and in reducing NOx. The much less reactive methane passes through a monolith comprising Pt/Al_2O_3 with little conversion at relevant space velocities (> 10k h^{-1}) and temperatures below 400°C [17]. In contrast, lean-burn NG vehicles generally utilize Pd-based catalysts, and the large excess of oxygen in the exhaust readily forms palladium oxide (PdO), which is quite active for methane oxidation [18, 19]. However, temperature

excursions that may occur are problematic since PdO decomposes at temperatures exceeding ~600°C even under oxidizing conditions [20, 21]. This can lead to a decrease in conversion due to the lower activity of metallic Pd. Indeed, the dynamics of the PdO/Pd interconversion can result in variations in the methane conversion with time-on-stream [22–26]. For example, it was reported that for Pd catalysts the CH_4 conversion depends on the direction of the change in feed composition [27, 28]. The transient behavior is exacerbated by catalyst deactivation primarily through Pd crystallite agglomeration at high temperature. The addition of Pt to Pd/PdO has been reported to inhibit this sintering [29]. Recent work has shown that bimetallic Pt-Pd catalyst formulations have improved thermal stability compared to Pt- or Pd-only catalysts [30]. Further, the emergence of "dual fuel" CNG + diesel powered engines means that Pt/Pd catalysts will be used for methane oxidation since this is the common composition of diesel oxidation catalysts (DOCs). For these reasons, Pt/Pd formulations are interesting catalyst candidates for methane oxidation in the exhaust of lean-burn vehicles.

1.3 Experimental Setup

The bench flow reactor setup (Fig. 1.1) includes mass flow controllers (MKS) for metering of cylinder-supplied gases (Praxair, Matheson), a quartz tube reactor within a tube furnace (Lindberg/Blue) and multiple thermocouples (Omega) for temperature monitoring and control. Custom vaporizers were constructed and supplied with liquid (HC or H_2O) by syringe pumps (Fisher Scientific 14-831-200) equipped with glass or plastic syringes of varying size (1-60 mL). The setup is controlled through National Instruments hardware running LabVIEW software.

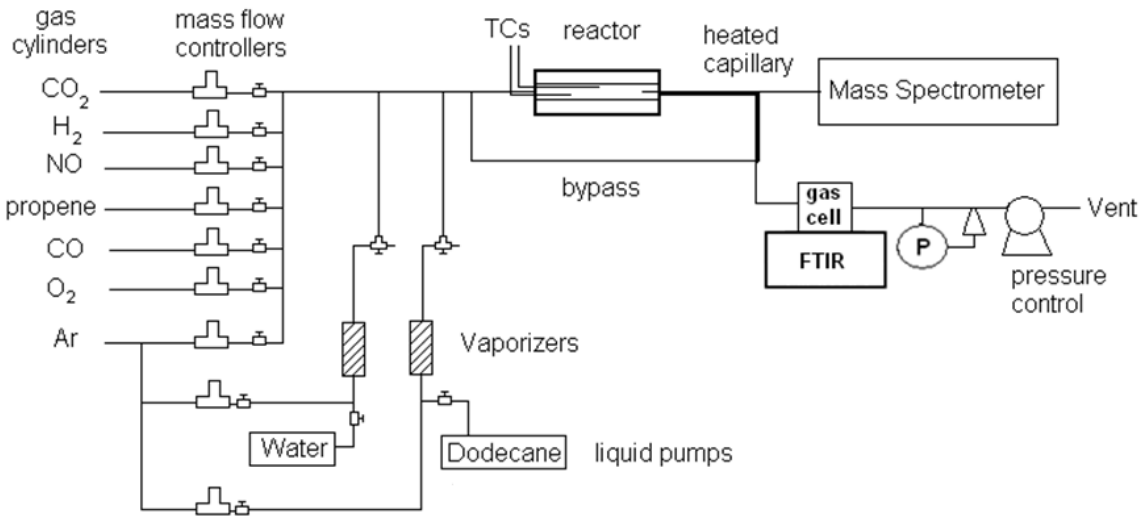

Figure 1.1 Experimental setup

Gas composition analysis was accomplished by FTIR (Thermo Scientific Nicolet 6700) equipped with a heated gas cell. Directly downstream of the gas cell is a pressure transducer and automated valve, followed by a pump, which maintain the gas cell at atmospheric pressure. The FTIR was used to measure concentrations in the bulk gas reactor effluent, as well as to confirm reactor feed concentrations through the use of a bypass line. Also utilized is a mass spectrometer (Pfeiffer GSD 301). Experimental temperatures were measured by type K 0.51 mm OD thermocouples. Custom end pieces were fabricated to accommodate the thermocouples and mass spectrometer capillary (Fig. 2.2, described further in Chapter 3 and Chapter 5). Catalyst temperature is measured at the approximate midpoint and the inlet feed gas temperature is measured 2 mm upstream of the front face of the catalyst. Heat tracing of post reactor lines minimized condensation. Experiments were primarily carried out using Ar as the diluent gas, although N_2 was used in some cases (Chapter 4). Typical gas hourly space velocity (GHSV) is 60,000 h^{-1} based on the overall monolith sample volume and standard conditions.

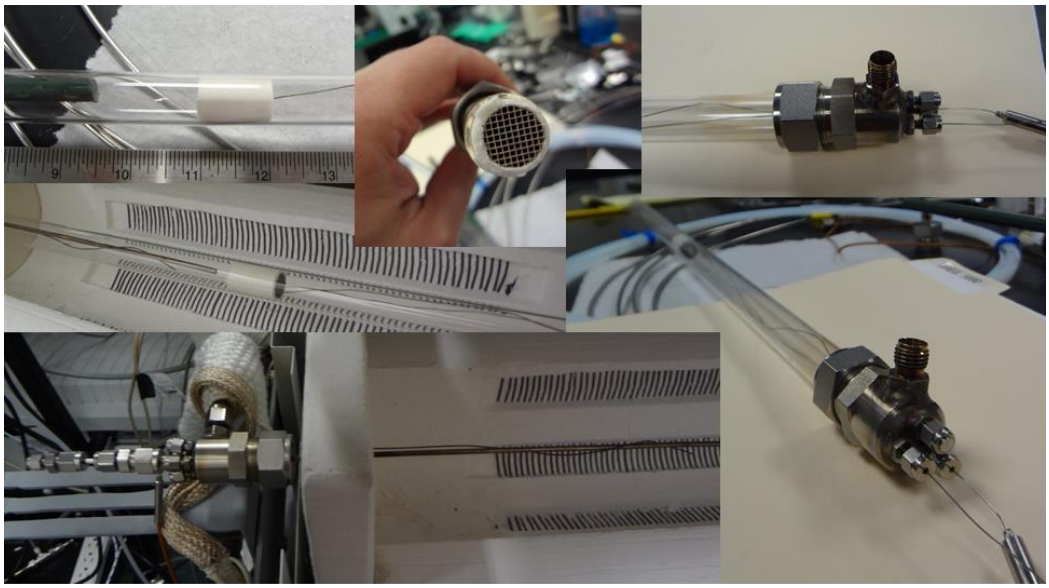

Figure 1.2 Collage of quartz reactor, custom end pieces and ceramic monolith catalyst

1.4 Catalysts

The catalysts used in this study are washcoated 400 cpsi (6 mil wall thinkness) cordierite monoliths containing Pt/Pd in a 2:1 ratio by weight (~1:1 molar ratio) on γ-Al_2O_3 alumina support (supplied by BASF, Iselin, NJ). The series of catalysts prepared for this work contain loadings as outlined in Table 1.1. Precious group metal (PGM) loading varies between 0 and 120 g/ft^3 and zeolite loading varies between 0 and 1 g/in^3. The catalysts arrived as sample cores of 1 inch diameter and 3 inches in length and were then cut to 0.5 inch diameter and 1 inch length using a diamond-tip cylindrical drill bit.

Table 1.1 Series of BASF catalysts

Sample #	Name	PGM load (g/ft^3)	Zeolite Beta Loading (g/in^3)	Bulk Alumina Loading (g/in^3)	Total Washcoat Loading (g/in^3)
1	D0-l	0	0.2	1.2	1.4
2	D0-m	0	0.5	1.2	1.7
3	D0-h	0	1	1.2	2.2
4	D60-0	60	0	0.7	1.4
5	D60-l	60	0.2	0.7	1.6
6	D60-m	60	0.5	0.7	1.9
7	D60-h	60	1	0.7	2.4
8	D90-0	90	0	0.35	1.4
9	D90-m	90	0.5	0.35	1.9
10	D120-0	120	0	0	1.4
11	D120-m	120	0.5	0	1.9

1.4.1 BET Characterization

To achieve the high catalytic activity required to treat vehicle exhaust emissions while keeping costs to a minimum the precious metals are deposited on a high surface area support. Catalysts and their support materials are thus often characterized by their specific surface area (m^2/g). Exhaust catalysts can also contain adsorbents to trap hydrocarbon emissions prior to reaching light-off temperature (see subsequent sections). High surface area is one parameter to quantify when searching for better performing adsorbents.

Surface area measurement is typically performed using the BET method, based on the 1938 publication by Brunauer, Emmett and Teller [31]. The method is named after their initials. The working principle of BET is that an inert gas will physically adsorb (physisorb) to the surface of the sample by van der Waals force, form a monolayer, and then form multilayers. The surface area of the monolayer can be determined by metering

the amount of gas (usually nitrogen) it takes to reach several relative pressures at constant temperature, the isotherm, and using the BET equation:

$$\frac{P_s}{V_A(P_0 - P_s)} = \frac{1}{V_M C} + \left[\frac{C-1}{V_M C}\right] \times \frac{P_s}{P_0}, \quad (1\text{-}1)$$

where P_s is the sample pressure, P_0 is the saturation pressure, V_M is volume of monolayer, V_A is volume adsorbed, and C is a constant related to enthalpy of adsorption.

A plot of $P_S/V_A(P_0\text{-}P_S)$ against P_S/P_0 should give a straight line with intercept of $1/V_MC$ and slope of $(C\text{-}1)/V_MC$. The slope and intercept are then used to calculate V_M.

$$S_{BET} = \frac{V_M \times N_A \times A_M}{M_V \times a}, \quad (1\text{-}2)$$

where S_{BET} = BET surface area, N_A is Avogadro's number, A_M is the cross sectional area occupied by each adsorbate molecule (0.162 nm^2 for nitrogen), M_V is the gram molecular volume (22414 mL), and ɑ is the mass of the sample.

The TxCEF lab owns and operates a Beckman Coulter SA 3100. This model has the capability to outgas up to 3 samples simultaneously. The reference and measured sample are submerged in liquid N_2 (77 K). The sample tube has a flat bottom for improved time to thermal equilibrium (more surface area for faster heat transfer). A quartz rod is also used to decrease dead volume, which improves accuracy and speeds up analysis time.

The BET surface area measurement can be a useful tool during the processes of increasing catalyst activity per mass of catalyst, reducing catalyst cost, minimizing reactor volume, increasing catalyst stability, maintaining quality control, or detecting changes in surface area resulting from use. A limitation of the BET method is that it cannot differentiate between surfaces, so the surface area measurement will be combined

support and precious metal surfaces. The analysis of precious metal surface area and dispersion can be done by performing chemisorption. The BET method also has the limitation that the sample size must fit into bottom of sample tube, which might necessitate sample destruction.

The BET measurement results for the BASF series of catalysts are listed in Table 1.2. The table reports the m^2/g sample, which is based on the total mass of the sample core, and the m^2/g washcoat, which takes into account the total washcoat loading, which varies as listed in Table 1.1.

Table 1.2 BET measurement results

Sample	PGM (g/ft^3)	Zeolite Beta loading($g/in^{3)}$	BET (m^2/g sample)	BET (m^2/g washcoat)
DOC1	0	0.2	37.0	134.7
DOC2	0	0.5	50.7	152.2
DOC3	0	1	70.6	163.6
DOC4	60	0	24.1	87.7
DOC5	60	0.2	28.0	89.4
DOC6	60	0.5	40.9	109.9
DOC7	60	1	69.8	148.3
DOC8	90	0	25.3	92.0
DOC9	90	0.5	48.7	130.8
DOC10	120	0	20.8	76.0
DOC11	120	0.5	45.4	121.8

A plot of the BET results as a function of zeolite loading is shown in Fig. 1.3. This reveals the trend of increasing BET surface area with increasing zeolite loading. This trend can be expected due to the high surface area of zeolite beta, ordinarily between 600-700 m^2/g [32].

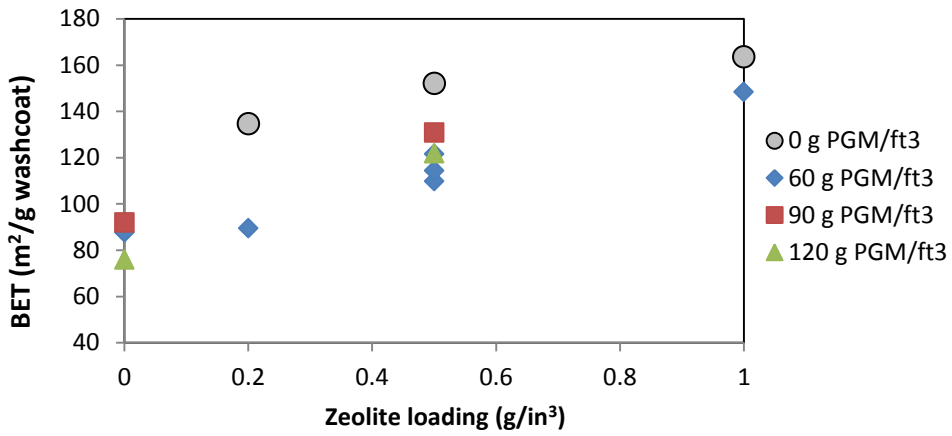

Figure 1.3 BET surface area dependence on zeolite loading

1.5 Research Objectives and Outline

The overarching objective of this dissertation is to elucidate the behavior of multifunctional Pt/Pd monolithic catalysts for HC emission control through performance studies. This is accomplished through several related yet distinct studies which comprise the chapters of this dissertation. The chapters do not appear in the chronological order that the experimental work was performed, but rather are arranged in a more logical flow to improve readability and understanding.

Chapter 2 investigates the performance of Pt/Pd/zeolite beta catalysts containing varying amounts of zeolite with a focus on HC storage and light-off behavior. Dodecane (C12) is used as the model HC and carbon monoxide (CO) is also utilized as it is a key criteria pollutant. Mixtures of C12 and CO yield insights into the effects of additional zeolite on catalyst performance. The intent of this study is to provide a systematic set of data that will advance the understanding of multi-functional DOCs containing a zeolitic hydrocarbon trap material.

Chapter 3 continues the oxidation theme but with a focus on propylene and also introduces a new measurement technique. The construction of a spatially resolved

capillary-inlet sampling system for in-channel concentration measurements is described. A study on propylene oxidation is then conducted and the newly built sampling technique is utilized. Additionally, the low-dimensional model formulation of Joshi et al. [33] is adapted to model the propylene effluent conversions as well as model the propylene concentration profiles through the catalyst. The model results are then compared to the experimentally-obtained data.

Chapter 4 reports on proprietary catalyst testing that were performed for a third party, which includes both oxidation and NSCR catalysts. This chapter has been approved for publication in this dissertation by the third party, provided their identity is not revealed. The reactant feed streams in this study are relatively complex, containing N_2, O_2, CO_2, H_2O, NO, NO_2 and a mixture of hydrocarbons, comprised of methane, ethane, ethylene, propane, propylene, and formaldehyde. A unique feature of the study is the use of a metal substrate rather than ceramic for the third party catalysts. The performance of the proprietary catalysts is then compared to the performance of a Pt/Pd catalyst, followed by additional experiments to develop a more fundamental understanding of the results. Interesting features of methane oxidation were first identified during this study.

The focus of Chapter 5 is methane oxidation by Pt/Pd monolith with steady-state and transient features examined over a wide range of temperatures and feed gas compositions. (This chapter is reproduced from a previously published work [34] with permission from Elsevier.) The methane conversion displays multiple states depending on temperature, oxygen concentration, and catalyst history. A clockwise hysteresis was observed in the rich regime whereupon lowering the O_2 feed below a critical value

resulted in light-off of the methane oxidation reaction. From this light-off state, the O_2 feed can be increased, leading to an increase in the methane conversion as well as the CO_2/CO product selectivity. Continuing to increase O_2 feed concentration, however, led to catalyst surface poisoning and quenching of the methane oxidation reaction. Transmission electron microscopy (TEM) and energy dispersive spectroscopy (EDS) revealed catalyst particles containing a distribution of Pt/Pd ratios. Additionally, spatially resolved capillary-inlet mass spectrometry (SpaciMS) measurements reveal oxidation and partial oxidation reaction zones within the monolith catalyst.

This dissertation finalizes with Chapter 6. This chapter includes conclusions from the preceding performance studies and makes several recommendations for further research.

2. Impact of Zeolite Beta on Hydrocarbon Trapping and Light-Off Behavior of $Pt/Pd/Al_2O_3$ Monolith Catalysts

2.1. Abstract

The incorporation of zeolite beta (BEA) on the performance of monolithic $Pt/Pd/Al_2O_3$ diesel oxidation catalyst (DOC) was investigated in terms of hydrocarbon (HC) storage capacity, light-off temperature, and conversion of stored HC to CO_2. Dodecane (C12) was employed as the model HC to elucidate BEA loading impact on catalyst light-off performance for CO and HC oxidation. With increased BEA loading level, the specific storage capacity of the catalyst samples subsequently also increased. Temperature ramp experiments revealed light-off behavior for individual reactant feeds (CO-only or HC-only) had negligible dependence on zeolite loading level. A HC pre-storage experiment procedure was developed to evaluate the catalysts retention of HC after storage was complete, how the remaining stored HC affects light-off performance, as well as how much stored HC was converted to the desired product CO_2. Co-feed experiments (HC + CO simultaneous feed) were also performed.

In addition to CO self-inhibition, it was found that stored C12 inhibited the CO light-off, while a co-feed of C12 with CO inhibited the CO light-off even further. This trend was consistent within each of the three zeolite loading levels. During both co-feed and HC pre-storage experiments the medium level of zeolite loading resulted in improved (decreased) CO light-off temperatures when compared to the zeolite-free base case catalyst. This beneficial effect is attributed to the zeolite providing alternative storage sites for the HC and thus mitigating the inhibition on the CO light-off by freeing up precious metal sites for CO oxidation. However, the highest zeolite loading catalyst displayed increased CO light-off temperature during HC pre-storage experiments, and no

change compared to the base case during co-feed experiments. This trend reversal for CO light-off temperature is attributed to the increased amount of stored HC causing an inhibitory affect that can overwhelm the beneficial effects of the additional zeolite. The HC pre-storage experiments also showed that the highest zeolite loading yielded the highest percentage of stored HC converting to CO_2, which can be an important consideration for the eventual real world application. This experimental study reveals the possible need to optimize the zeolite loading for the desired operating conditions/requirements regarding light-off temperatures and HC storage capacity/conversion.

2.2. Introduction

The concept of cold start HC trapping for vehicle emissions control has existed for many years. One example was outlined in a U.S. Patent (3,699,683), granted in 1972 to J. F. Tourtellotte et al. [35], describing a HC absorbent bed downstream of the catalyst that would collect the HC emissions during startup and then be bypassed as temperatures rose. The adsorbent bed would then be regenerated by recycling the HC back into the engine. Other emission control technologies proved more effective and economical during this early period of vehicle emission control, so HC traps were not further developed at that time.

In the 1990s, spurred on by CARB (California Air Resources Board) and EPA emissions legislations, efforts returned to the cold start trap concept. The HC storage capacity of silicalite was reported on by Otto et al. in 1991 [36], however it was determined that the required volume would be too large to be practical to meet the requirements of vehicles at that time. In 1992, U.S. Patent (5,140,811) granted to T.

Minami and T. Nagase of Toyota, Japan, outlined a HC trapping device upstream of the catalyst such that as the exhaust temperature increased the desorbed HCs would encounter the catalyst [37]. This system also incorporated a bypass so that once exhaust temperatures reached a certain high limit the trap would be removed from the exhaust stream pathway and protected from degradation due to high temperatures.

Another early system was developed at Southwest Research Institute by Heimrich et al. [38], which also relied on valves and a HC adsorbent bypass. This system demonstrated a 35% reduction in cold-start HC emissions. Engler et al. [39] at Degussa AG made a target of developing an on-stream adsorber system without bypass lines in order to eliminate the expense and complexity of controlled regeneration and the temperature/corrosion resistant valves. This work examined several zeolite materials and also demonstrated improvement in HC emissions for two gasoline powered vehicles, up to a 50% reduction in HC emissions during FTP-75 drive cycle testing.

Much of the initial work on utilizing zeolites for cold-start hydrocarbon emission control was done with a focus on gasoline engines [38–49]. A few differences between gasoline exhaust and diesel exhaust that can affect HC storage and light-off behaviors include the air to fuel ratio and the chemical composition of the HC mixture. Gasoline exhaust is typically fuel rich or near stoichiometric at start-up while diesel exhaust is in general always lean. Gasoline-powered vehicles are, however, sometimes equipped with secondary air injection, which can improve the cold-start light-off of the catalyst. The type of exhaust HCs are related to the fuel type/composition [50], with gasoline generally comprising aromatics and intermediate molecular weight hydrocarbons (C6 – C10) while

diesel HCs are typically larger and linear (C16-C24). The concepts and findings from gasoline exhaust are, however, generally applicable to the treatment of diesel exhaust.

Research on cold start hydrocarbon trapping continued through the 2000s by various automotive and emission control companies, including Nissan [10, 51–54], Ford [55, 56], Toyota [57–59], Engelhard [60], Johnson Matthey [61], Hitachi [62, 63], Honda [64], Zeolyst [65] and Hyundai [66]. Work was also carried out during this time period at several academic institutions [67–78]. These studies largely targeted either a proof-of-concept vehicle demonstration or an investigation of different adsorbent materials for potential use in HC-trapping systems.

Inoue and Mitsuishi of Nissan Motor Co. reported on the performance of a dual-layer catalyst (precious metal loaded onto zeolite layer) combined with several other engine and emissions technology changes/improvements intended to reduce HC and CO emissions for a gasoline engine vehicle [79]. They outfitted a model year 2008 Nissan Sentra with the technologies, subsequently producing less than 10% of the allowable limit for NMOG (non-methane organic gases), CO and NOx emissions for SULEV (super ultra-low emissions vehicle) on the FTP75 test cycle, while also improving fuel economy by 5%.

Currently, most commercial DOCs contain a zeolite hydrocarbon trapping component. For example, the DOCs from 16 passenger cars meeting the Euro 4 emission standard were examined by Raux et al. in 2009 and it was found that all of the catalyst samples contained a zeolite component [80]. With such a widespread adoption by the industry, the addition of zeolite to DOC formulations can be presumed to have a beneficial effect in real world practice, or at least no substantial negative effects. It can be

assumed that much of the research has been proprietary and therefore further publications on HC trapping can advance the body of knowledge.

Additionally, the negative impacts of high exhaust HC concentrations reach beyond simply exceeding the allowable HC emissions limits. Several recent studies examined the HC poisoning of SCR catalysts [81, 82] and provide relevant experimental evidence and insight on dodecane inhibiting the reaction rates for catalysts containing zeolites. Luo et al. [81] determined that the larger pore structure of a model Cu-beta zeolite catalyst sample was more significantly inhibited by HC than the state-of-the-art Cu-zeolite sample with smaller pores. Kumar et al. [82] investigated further and concluded that even the small-pore Cu-zeolite catalyst can be significantly poisoned by dodecane when temperatures are elevated to the 300° to 400°C range. The researchers found that thermally activated chemical transformations led to HC storage within the small pores which negatively impacted the NOx conversion.

There are relatively few studies in the open literature exploring fundamental issues regarding hydrocarbon trapping and its effects on multifunctional DOC operation. To this end, in this study we investigate DOC catalysts containing additional zeolite for HC trapping with a focus on the HC storage and light-off behavior of several model Pt/Pd/zeolite DOC catalysts that contain a range of amounts of the zeolite component. Dodecane (C12) is used as the model HC and carbon monoxide (CO) is also utilized as it is a key criteria pollutant. Mixtures of C12 and CO can shed insight into the effects of the additional zeolite on catalyst performance. It is anticipated that as the amount of additional zeolite in the washcoat is increased, the HC storage capacity will also increase. The effect of the zeolite loading on light-off temperatures is not as easy to predict. Thus,

the intent of this study is to provide a systematic set of data that will advance the understanding of multi-functional DOCs containing a zeolitic hydrocarbon trap material.

2.3. Experimental

A bench flow reactor system was utilized to evaluate the Pt/Pd/zeolite DOC monolith catalysts (Fig. 2.1). A custom vaporizer was constructed to provide a stable concentration of dodecane, with the liquid HC supplied by a syringe pump (Fisher Scientific 14-831-200) with a 1 mL capacity glass syringe (SGE). The boiling point of C12 is 214°C and the vaporizer was operated at 170°C. The reactor effluent gas concentrations of CO, dodecane (C12) and CO_2 were quantified by FTIR (Thermo Scientific Nicolet 6700) equipped with a heated gas cell. Additional details of the experimental setup are provided elsewhere [34].

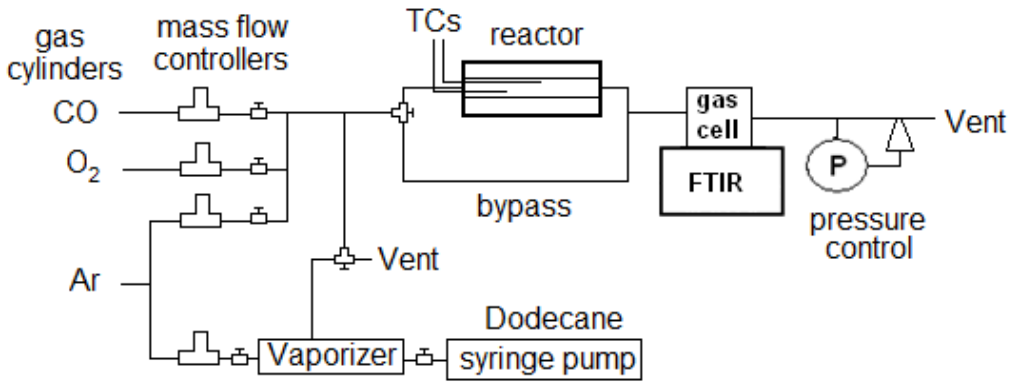

Figure 2.1 Experimental setup for hydrocarbon trapping and light off

The DOC catalyst samples used in this study were supplied by BASF (Iselin, NJ). The washcoated 400 cpsi cordierite monoliths (Table 2.1) contained 60 g/ft^3 precious metal in a Pt:Pd ratio of 2:1 by weight (~1:1 atomic ratio) on γ-Al_2O_3 support. The samples are differentiated by varying the zeolite beta (BEA) content (0 to 1 g/in^3) incorporated into the washcoat mixture. No zeolite is present in the D-0 catalyst, while D-0.5 contains 0.5 g/in^3 zeolite, and D-1 contains 1.0 g/in^3 zeolite. The sample cores were

cut to 0.5 inch diameter by 1 inch length and characterized by BET surface area measurement (Beckmann Coulter SA 3100). The surface area measurements have a positive correlation with zeolite loading level, which can be expected as BEA has a high surface area typically between 500-700 m^2/g [32, 83].

All experiments performed in this chapter employed a total gas flowrate of 3 L/min (GHSV= 56,000 h^{-1}). Temperature was recorded by a type K thermocouple located at the approximate midpoint of the catalyst sample. The catalyst sample was cleaned between experiments by temperature ramp to 500 °C while flowing 10% O_2 with balance argon.

Table 2.1 Catalyst details

Name	Alternate Name	PGM loading (g/ft^3)	BEA loading (g/in^3)	Alumina loading (g/in^3)	Total washcoat loading (g/in^3)	BET surface area (m^2/g sample)	BET surface area (m^2/g washcoat)
D-0	DOC4	60	0	0.7	1.4	24	88
D-0.5	DOC6	60	0.5	0.7	1.9	45	122
D-1	DOC7	60	1	0.7	2.4	70	148
PGM = Pt:Pd = 2:1 (g) ≈ 1:1 (mol), 400 cpsi, 6 mil wall							

Dodecane adsorption experiments were carried out by establishing a constant 100 ppm concentration of C12 through the bypass line (with 10% O_2 and Ar balance), then switching the gas feed to flow through the catalyst sample at room temperature. The effluent C12 concentration was measured continuously. The total amount of C12 stored by the catalyst sample was calculated by applying the equation:

$$\text{HC storage capacity} = \frac{Q(C_{Feed} - \int C(t)dt)}{m}, \qquad (2\text{-}1)$$

or more specifically

$$\text{HC storage capacity} = \frac{[Q(\sum_{t_{start}}^{t_{end}}(C_{Feed} - C_t) \times (t_t - t_{t-1})](\frac{\min}{60s})(\frac{1}{10^6\, ppm})(\frac{L}{1000cm^3})(\frac{170.33g}{mol})}{(\frac{22.4L}{mole})(m)},$$

where Q [sccm] is the total feed gas flowrate, C_{Feed} [ppm] is the feed HC concentration, C(t) [ppm] is the effluent HC concentration at time t [s], and m is the catalyst sample mass [g]. Since the catalyst sample weights are affected by the zeolite loading, a specific HC storage capacity was calculated to normalize the results. This specific capacity is based on the actual mass of the clean catalyst sample as well as the washcoat loading in order to calculate the amount of HC stored per gram of catalyst:

$$\text{washcoat specific HC storage capacity} = \frac{Q(\int (C_{Feed} - C(t))dt)}{(m)(wc)}. \qquad (2\text{-}2)$$

Light-off curves (conversion vs temperature) were acquired using a temperature ramp procedure (3 °C/min) to mimic vehicle exhaust warmup. A temperature ramp can give different results than steady-state operation due to inherent transient conditions and associated accumulation effects. Light-off curves were produced for single component feeds of CO and C12 (with 10% O_2 and balance Ar) as well as for co-feed experiments in which both CO and C12 reactants were fed simultaneously. A HC pre-storage procedure was also used to evaluate several parameters, including catalysts retention of HC after storage is complete, how the stored HC affects light-off performance of the catalyst, as well as how much of the stored HC is oxidized.

For the HC pre-storage experiments, the catalyst was first loaded with C12 to saturation, exactly as in the adsorption experiments. The C12 feed was then stopped and the stored C12 was allowed to desorb for 30 min under a flow of 10% O_2 and balance Ar. The vaporizer setup was equipped with a 3-way valve such that the flow of HC could be

diverted to vent and enabling a rapid reduction in the C12 feed concentration to zero while maintaining an O_2/Ar flow through the catalyst. The vaporizer carrier gas flow rate of 500 ml/min Ar was established through the main manifold within a few seconds of switching the vaporizer to vent. This enabled a reliable measurement of the C12 desorption from the catalyst after the C12 feed was cut off. Directly following the desorption period of 30 min, CO was introduced into the feed stream and the temperature ramp (3 °C/min) was initiated. The CO light-off curve in the presence of stored C12 was then acquired. Continued measurements of the C12 concentration also enabled an estimate of the amount of C12 stored, desorbed during 30 min purge, desorbed during temperature ramp, and the amount stored that converted to CO_2.

2.4. Results and Discussion

2.4.1. HC Trapping

The hydrocarbon trapping experiments verified the anticipated behavior that an increase in zeolite loading resulted in increased HC storage. As shown in Fig. 2.2, when the established flow of 100 ppm dodecane (C12) through the bypass line was diverted via the switching valve to the clean catalyst, the catalyst was subjected to a step change in C12 concentration. The catalyst sample stored a large fraction of the C12, which resulted in the noted drop in C12 effluent concentration. With time on stream the rate of HC storage decreased as the catalyst saturation increased until eventually the outlet concentration matched the inlet concentration, indicating the cessation of HC storage. The data in Fig. 2.2 clearly show the different behavior of the three catalyst samples.

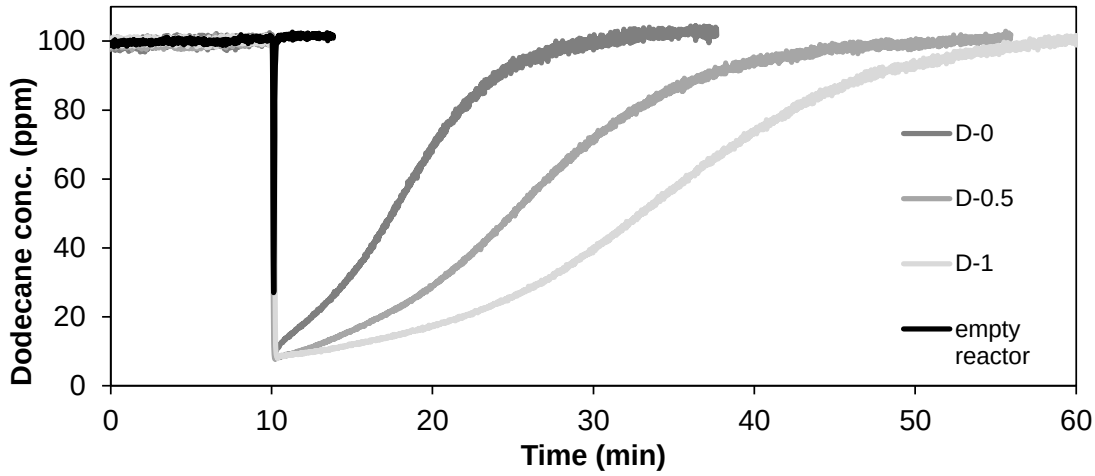

Figure 2.2 Effluent dodecane concentration during HC storage experiments (T=35 °C, 100 ppm C12, 10% O_2, balance Ar, GHSV=56,000 h^{-1})

The D-0 catalyst (Fig. 2.2 dark gray) exhibited some trapping behavior despite having no zeolite in the washcoat. However, the effluent dodecane concentration recovered quicker than the other two samples. The time between the start of C12 storage and saturation was approximately 20 min for the D-0 catalyst. Repeating the experiment three times yielded an average storage of 9.5 mg C12/gram of catalyst sample (std. dev. = 0.5 mg/g cat.), and a calculated specific storage capacity of 57.6 mg C12/g washcoat. Without any zeolite the dodecane must be primarily stored by physisorption on the high surface area alumina, as well as some storage on the precious metal crystallites.

The D-0.5 catalyst (Fig. 2.2 medium gray), which has a 0.5 g/in^3 BEA loading, stored more dodecane and took a longer time (35 min) to reach saturation. The medium zeolite loading catalyst averaged 18.1 mg C12/g of sample (94.4 mg C12/g washcoat). The D-1 catalyst (Fig. 2.2 light gray) with its 1.0 g/in^3 zeolite loading took a full 50 min for saturation, and averaged 26.8 mg C12/g of sample (107.2 mg C12/g washcoat). The increase in HC trapping capacity is consistent, increasing 9.0 mg/g of sample from the

zeolite-free catalyst to the medium loading and an additional 8.3 mg/g by the sample with the highest zeolite loading.

The shape of the adsorption curves contain information pertaining to the fundamental behavior of the catalyst at these conditions. The increasing concentration of effluent dodecane is relatively slow and gradual leading up to the eventual catalyst saturation. This indicates that that the storage itself is relatively slow. This is in contrast to a step-change behavior, which would indicate a very fast storage. In the case of a step-change behavior, the front portion of the monolith catalyst would saturate first, with no HC remaining to be adsorbed by the back portion. The storage takes place as a moving front through the catalyst until reaching the back portion and then a clear increase in HC is observed in the effluent, referred to as a "breakthrough". In the current case, the storage is relatively slow and the HC storage accumulates over time in a concentration gradient starting from high in the front to low in the back and high on the washcoat surface and low at the washcoat bottom.

Note that none of the catalyst samples reduced the C12 effluent concentration to zero, so there is no subsequent "breakthrough" time in the traditional sense. This is likely a limitation due to the rate of HC storage from the gas phase to the solid surfaces, which includes diffusion into the pore structure of the zeolite. The inability of the catalysts to reduce the C12 concentration to zero is not believed due to gas bypassing; i.e. where some portion of the flow is slipping through or around the catalyst sample without contacting it. During the oxidation experiments (explained in detail later) the CO and C12 reach ~100% conversion at high temperatures, therefore no bypass is occurring.

To insure a large portion of the measured HC trapping is not merely due to condensation of C12 on the cool reactor tube surfaces, experimental runs were performed with an empty reactor tube, with one empty run shown in black in Fig. 2.2. The momentary decrease in effluent C12 results in minimal HC trapping, and is calculated to be only 0.15 mg. This concentration drop is thought to be a result of the volume of gas in the reactor tube that is dodecane-free and which gets pushed downstream through the analyzer when the switching valve is first initiated.

Hydrocarbon trapping experiments were also conducted using a lower concentration of 50 ppm C12 during storage on the D-0 catalyst. A comparison of the effluent C12 during storage on the D-0 catalyst with concentrations of 50 ppm and 100 ppm C12 is shown as Fig. 2.3. The 50 ppm feed resulted in an average storage amount of 6.2 mg C12/g sample and took approximately 30 min to reach saturation. This is a decrease in the amount of HC stored compared to the same catalyst exposed to the 100 ppm C12 feed concentration. This indicates that the HC partial pressure affects HC storage capacity.

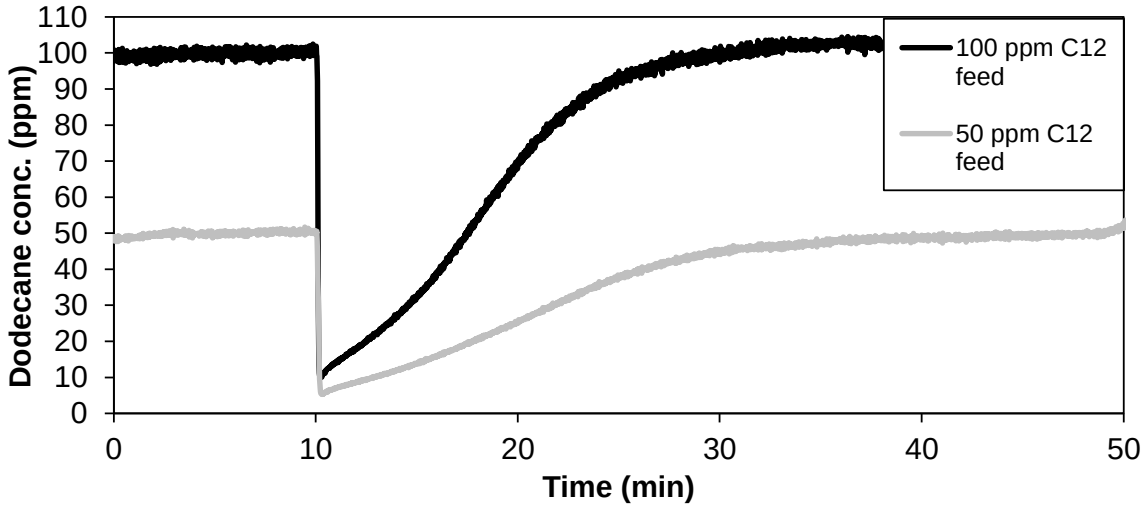

Figure 2.3 Effluent dodecane concentration during HC storage experiments (T=35°C, D-0 catalyst, 10% O_2, balance Ar, GHSV=56,000 h^{-1})

2.4.2. Light-off measurements

Single-component temperature ramp experiments were performed with the D-0 catalyst first to get baseline performance results. Classic light-off behavior was observed, as shown in Fig. 2.4. The 500 ppm feed of CO began to oxidize just above 100 °C, reached 15% conversion at 125 °C, and then very quickly climbed to 90% conversion at 133 °C, before its slower approach to complete conversion, resulting in the S-shaped curve. Increasing the feed concentration to 2000 ppm CO resulted in a qualitatively similar light-off curve; however it shifted to increased temperatures, thus displaying CO self-inhibition. The 15% conversion point was not reached until 155 °C, while 90% conversion was attained at 161 °C. The temperature at which 50% conversion was achieved (T_{50}) increased by 29 °C from 130 ° for 500 ppm CO to 159 ° for 2000 ppm CO.

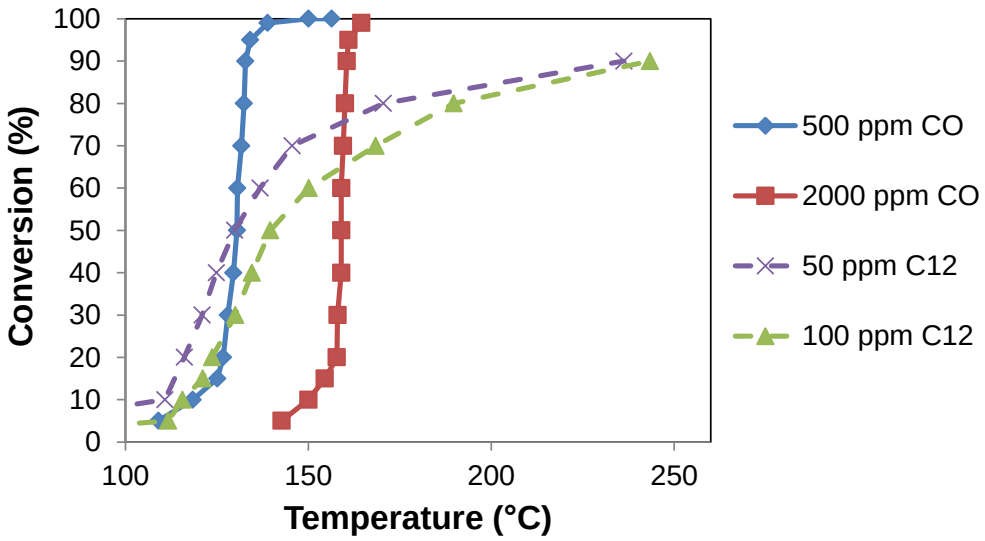

Figure 2.4 Single component light-off profiles for D-0 catalyst (10% O_2, 3°C min^{-1} ramp rate, GHSV=56,000 h^{-1}).

The light-off curves for C12 (Fig. 2.4) were notably less steep than the CO oxidation curves. The C12 mixtures also required higher temperatures to reach high

conversion. For example, a feed of 50 ppm C12 through the D-0 catalyst began to react at relatively low temperature (Fig. 2.4, x markers), reaching 10% conversion at 111 °C. The C12 conversion continued to increase nearly linearly with temperature, reaching T_{50} at 130 °C (and intersecting the 500 ppm CO curve). A further temperature increase led to diminished increases in conversion, with the 50 ppm C12 feed reaching 90% conversion at 236 °C. Doubling the C12 feed concentration to 100 ppm shifted the light-off curve (▲ markers), with T_{50} = 140°C, an increase of 10°C compared to the 50 ppm C12 feed. Further analysis revealed that at low conversions (<20%) the C12 feed concentration had no effect on reaction rate, indicating a zero order dependency on C12 in the low temperature kinetic regime.

Comparing the single component light-off curves for all three catalyst samples, displayed in Fig. 2.5, makes it apparent that the additional zeolite does not have a significant effect on catalyst performance at the conditions used in this study. As shown in Fig. 2.5, the T_{50} for 500 ppm CO aligns at ~119 °C for every zeolite loading level. At the increased concentration of 2000 ppm CO, the self-inhibition on the oxidation reaction rate appears to affect each catalyst formulation equally, with T_{50} at ~147 °C. This is an interesting result, as the increase in zeolite loading and the accompanying increase in washcoat thickness might be presumed to increase the diffusional resistance and thus reduce the reaction rate. That the CO light-off curves are not differentiated between catalyst samples implies that the precious metal loading is the primary contributor to the catalyst performance. Single component feeds of 100 ppm C12 also align closely, with T_{50} ranging between 140 °C and 145 °C.

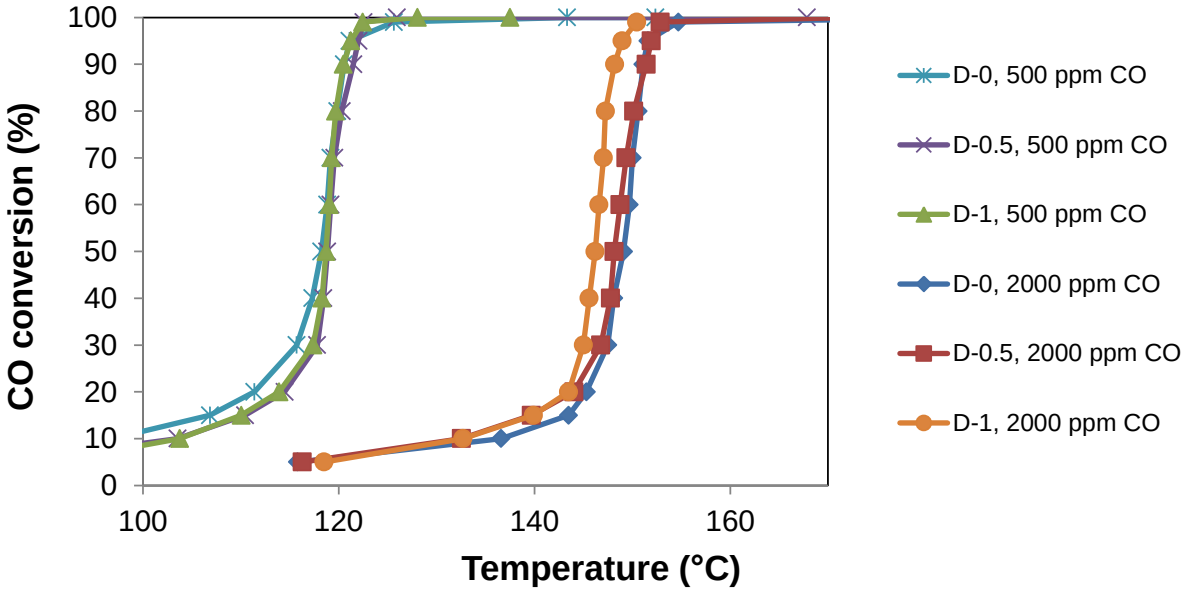

Figure 2.5 Light-off behavior for 500 ppm CO and 2000 ppm CO with D-0, D-0.5 and D-1 catalysts (10% O_2, 3 °C min^{-1} ramp rate, GHSV=56,000 h^{-1}).

2.4.3. Co-feed Experiments

When both reactants (CO and C12) were fed simultaneously, interspecies inhibition effects were identified. The CO-only light-off curves for D-0 were compared to the CO light-off curve during co-feed with 100 ppm C12 in Fig. 2.6. The data show that the presence of C12 in the feed mixture has an inhibitory effect on the CO oxidation rate for this catalyst when following a temperature ramp procedure. The T_{50} for 500 ppm CO during co-feed of 100 ppm C12 is 138 °C, which is an increase of 20 °C over the 500 ppm CO-only light-off temperature. Also evident in Fig. 2.6 is that inhibition due to 100 ppm C12 is not as detrimental to the CO light-off as the increased CO concentration of 2000 ppm.

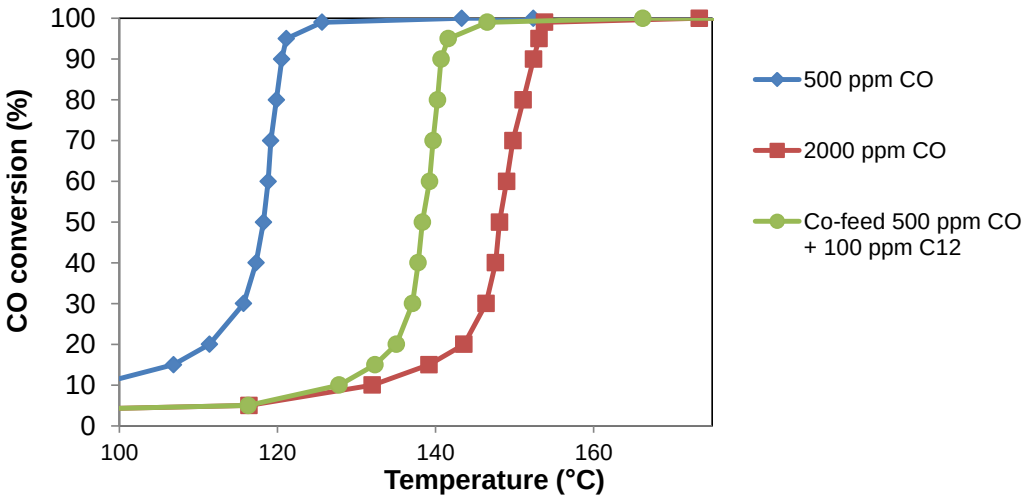

Figure 2.6 Effect of co-fed 100 ppm C12 on 500 ppm CO light-off for D-0 catalyst (10% O_2, 3 °C min^{-1} ramp rate, GHSV=56,000 h^{-1}).

The C12 light-off curves for a single component feed of 100 ppm C12 and the co-feed of 100 ppm C12 with 500 ppm CO are shown in Fig. 2.7. Instead of causing a shift in light-off temperature while maintaining the same shape and curvature, as was seen for CO, the co-feed has a more complex effect on the C12 light-off. Clearly there is an inhibitory effect at lower temperatures, as the 10% conversion mark is not reached until 139 °C, which is an increase of 23 °C compared to the C12-only light-off. From this point the C12 conversion during co-feed climbs rather abruptly, while the C12-only conversion increased more gradually. During the co-feed the C12 conversion reached T_{50} at 142 °C, only 2 °C higher than the C12-only feed. The higher temperature portion of each curves are similar.

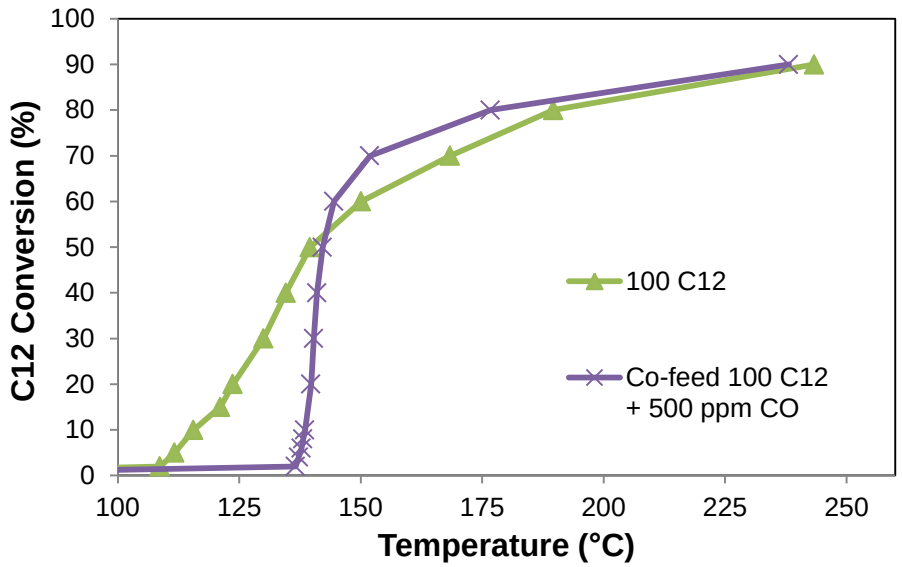

Figure 2.7 Effect of co-fed 500 ppm CO on 100 ppm C12 light-off for D-0 catalyst (10% O_2, 3 °C min^{-1} ramp rate, GHSV=56,000 h^{-1}).

To examine the light-off behavior during the co-feed experiments in more detail, the outlet concentrations of CO, C12 and CO_2, as well as catalyst temperature, are plotted for a typical experiment in Fig. 2.8. The feed of dodecane vapor was first stabilized at 100 ppm in the bypass line and then the valve was switched at the 65 min mark to conduct the HC storage until the sample was saturated. The temperature of the catalyst increased slightly during this trapping period even though the reactor furnace was open to the room temperature laboratory. This is attributed to the feed gas stream being heat traced upstream of the reactor, thus carrying some heat into the reactor. After the C12 had saturated the catalyst, which is indicated by the outlet C12 concentration matching the inlet concentration, 500 ppm CO was admitted to the feed stream, and a few minutes later the temperature ramp was initiated.

As the temperature began to rise, the effluent concentration of C12 increased above the 100 ppm level due to desorption of some C12 stored on the catalyst, demonstrating that the storage capacity of the catalyst decreased as temperature

increased. At t = 120 min the temperature reached ~100 °C and the effluent C12 concentration returned to ~100 ppm, indicating the bulk of the desorption was completed and the C12 inlet concentration matched the outlet concentration again. Carbon dioxide began to appear at 120 min, presumably due to the oxidation of CO. The rate of the CO oxidation increased with temperature, with the reduction in CO concentration mirroring the increase in CO_2 concentration. A sharp decrease in CO concentration occurred at 131 min as the reaction achieved light-off, with T_{50} occurring at 137 °C.

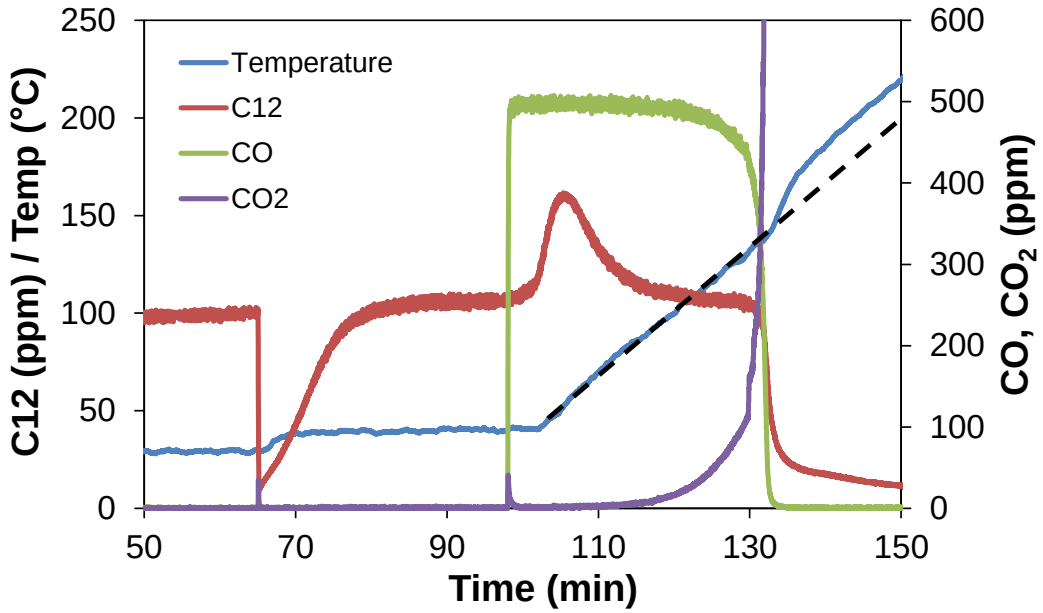

Figure 2.8 Co-feed experiment with 500 ppm CO and 100 ppm C12 with D-0 catalyst (10% O_2, GHSV=56,000 h^{-1}).

At the same time as the CO light-off event, the C12 concentration decreased sharply, with the notable result being a sharp increase in CO_2 concentration, which goes off the scale in Fig. 2.8. The explanation for this rapid increase in the C12 oxidation reaction rate at the time of CO light-off is the increased availability of catalyst sites, which are no longer poisoned by CO. Looking back at the Fig. 2.7 data, it is now evident that during the co-feed the CO inhibits the C12 reaction at low conversion and the rapid

increase in C12 conversion aligns with the CO light-off. The enhancement in C12 conversion during the co-feed that occurs at C12 conversions greater than 50% is likely a temperature effect. As shown in Fig. 2.8, the measured temperature after the light-off is above the linear temperature ramp (dotted line); this is attributed to the exothermic reactions taking place. While Fig. 2.7 does plot measured temperature vs conversion, temperature gradients likely exist and the temperature is measured at the midpoint of the catalyst. During the co-feed experiment, any continued increase in temperature downstream of the measurement point compared to the single component experiment will increase the rate of the C12 oxidation reaction. This increase in rate can more than offset the potentially lower temperature in the front portion of the catalyst, and is likely the reason for the enhancement in C12 conversion during co-feed at high conversions in Fig. 2.7.

2.4.4. Pre-storage experiments

The HC pre-storage experiments, which follow the procedure described in the experimental section, elucidate several features. First, the catalyst's ability to retain HC after completion of the HC storage is evaluated by purging with 10% O_2/Ar for 30 min and measuring the amount of HC that desorbs. This is a measure of the affinity of the HC to the adsorption sites. Second, the effect of the remaining stored HC on the catalyst's CO light-off performance is measured. This is a measure of the coupling between HC sorption and the extent of competitive adsorption. Third, the amount of the initially stored HC that is converted to CO_2 (rather than desorbing or forming other HC products) is calculated. This is a measure of the catalytic HC oxidation activity and storage/release features of the catalyst.

Results for a typical pre-storage experiment are shown in Fig. 2.9. The data show the vaporized C12 concentration being stabilized at 100 ppm through the bypass, and then at 72 min the switching valve is actuated to begin the HC storage on the catalyst sample. After reaching HC saturation (effluent C12 concentration reaches 100 ppm) the C12 feed is stopped at 99 min, leading to desorption of C12 from the catalyst during the half hour purge. During purging/desorption the effluent C12 concentration declines to 3 ppm at the 129 min mark, at which point 500 ppm of CO is added to the feed stream and the temperature ramp is initiated. As the temperature is increased, a small desorption peak of C12 is apparent prior to the light-off of CO, and the production of CO_2 soon follows. There were no carbon containing species detected other than C12, CO, and CO_2, indicating that the C12 does not decompose or otherwise react to form other HC species under the conditions of these tests. Repeating the pre-storage light-off experiment several times with each catalyst sample yielded consistent results in terms of CO light-off curves and HC storage, desorption and conversion.

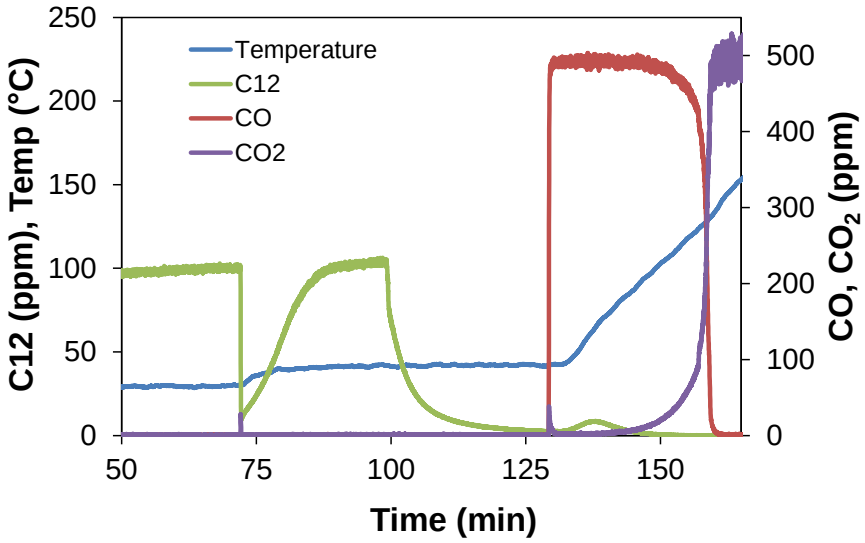

Figure 2.9 HC pre-storage experiment showing 100 ppm C12 storage followed by 30 min desorption, then 500 ppm CO temperature ramp (10% O_2, 3°C min^{-1} ramp rate, D-0 catalyst, GHSV=56,000 h^{-1}).

An important and interesting result from the HC pre-storage experiments is the effect of stored HC on the CO light-off curve. Shown in Fig. 2.10 are the CO light-off curves for the D-0 catalyst, displaying a clear inhibition effect on the 500 ppm CO light-off when there is stored C12 (x) when compared to the single reactant 500 ppm CO feed (diamonds). The data also reveal that the inhibition due to stored C12 is less than the inhibition due to the co-feed of C12 (circles). The light-off curve for 2000 ppm CO only feed is included for further context. The progressive increase in T_{50} CO light-off temperatures from the 500 ppm CO only feed (118 °C) to the 500 ppm CO with stored C12 (129 °C) to the co-feed 500 ppm CO + 100 ppm C12 (138 °C) can be attributed to an increasing inhibitory effect of C12.

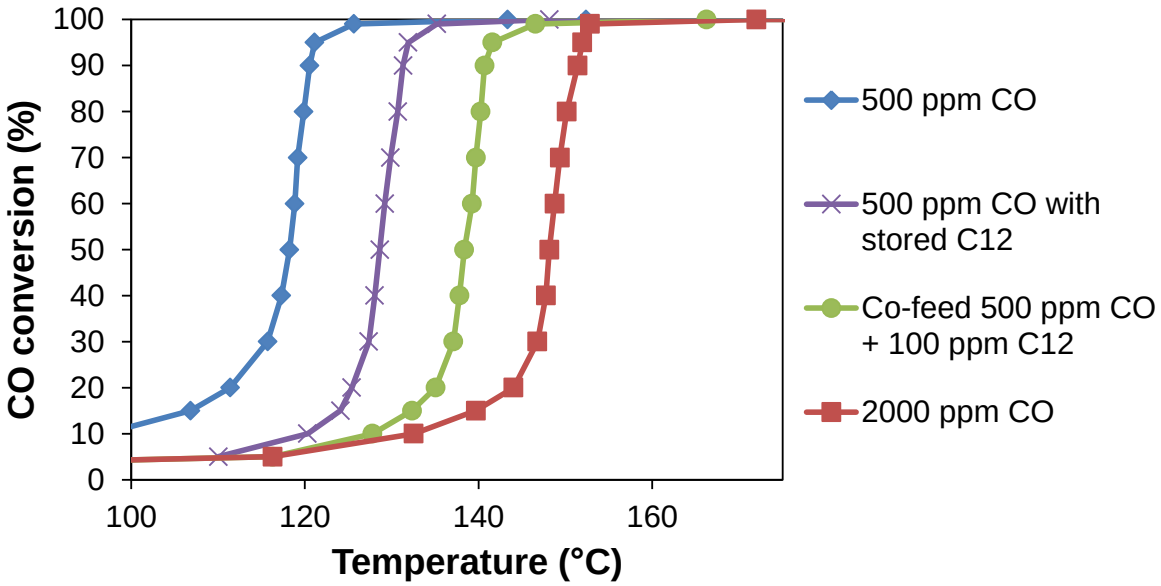

Figure 2.10 CO light-off curves for D-0 catalyst including results of pre-store C12 experiments (10% O_2, 3 °C min^{-1} ramp rate, GHSV=56,000 h^{-1}).

2.4.5. Zeolite loading effects on co-feed and pre-storage experiments

As shown earlier, the zeolite loading did not have a significant effect on the light-off temperatures for single reactant feeds of CO or C12. The C12 co-feed and pre-storage experiments for the catalyst samples containing zeolite indicated that C12 can inhibit the

CO oxidation light-off. Specifically, the extent of inhibition followed C12 co-feed > C12 pre-store > CO-only. However, the amount of temperature shift was not consistent across different catalyst samples and therefore led to catalyst differentiation based on zeolite loading. Shown in Fig. 2.11 are the CO light-off curves for all three catalysts comparing the CO-only condition to the pre-stored C12 condition. The standard deviations were calculated and there was no overlap in the light-off curves confirming the shifts in temperatures are consistent and statistically significant.

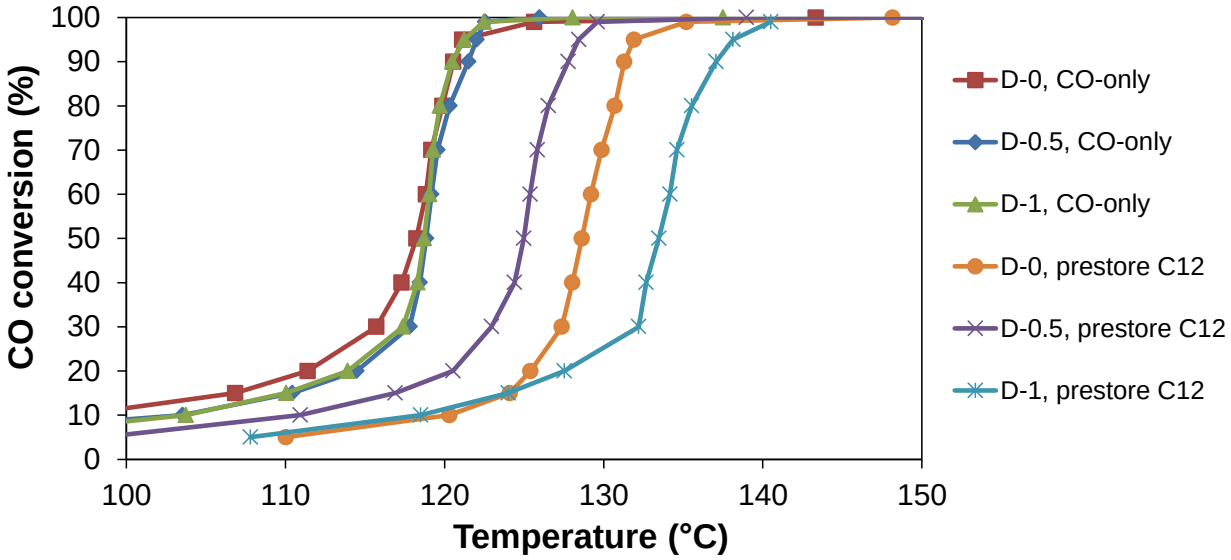

Figure 2.11 Comparing effect of pre-store 100 ppm C12 on 500 ppm CO light-off for D-0, D-0.5, and D-1 catalysts (10% O_2, GHSV=56,000 h^{-1}).

The Fig. 2.11 data show a non-monotonic effect of the zeolite loading on the extent of CO light-off inhibition by the pre-stored C12. The presence of 0.5 g/in^3 zeolite in the washcoat of the D-0.5 catalyst has the result of lowering the CO light-off temperature (x) compared to the no-zeolite base case (●). The beneficial effect on the CO light-off seen for the medium loading of zeolite is attributed to the zeolite providing alternative storage sites for the HC, thus lessening the inhibition on CO oxidation. With a further increase in zeolite, bringing the total to 1.0 g/in^3 in the D-1 catalyst, the end result

is a net inhibitory effect and the light-off temperature (*) is increased beyond that of the base case. The extent of inhibition on CO light-off by C12 is affected by several factors. These factors include competitive adsorption, transport inhibition, and species migration. These factors are now briefly described.

The first inhibition factor is competitive adsorption on the PGM sites. The C12 stored by the catalyst sample adsorbs to surfaces, some of which occupy catalytic sites. When the C12 molecules are adsorbed to active metal sites it blocks CO and O_2 from reaching the site. Excluding the reactants from a portion of the PGM sites subsequently results in inhibition of the CO reaction and light-off.

The second factor involves the blockage of pores by C12. The physical presence of C12 serves to restrict the transport of CO and O_2 through the washcoat passages. The restriction slows down the rate at which the reactants reach the available active catalyst sites and thus the CO light-off is inhibited.

The third factor is species migration. The washcoat alumina and zeolite store C12 at low temperature. After the temperature ramp commences the C12 can start desorbing or becoming more mobile on the catalyst surface. The desorbed C12 can re-adsorb or the surface mobile C12 can migrate to the PGM active sites and thus now inhibit the reaction by the first factor, competitive adsorption.

These factors can help explain the catalyst behavior as shown in Fig. 2.11. Each catalyst displayed increased CO light-off temperatures during C12 pre-store experiments, demonstrating the inhibition due to presence of C12. The degree of inhibition is apparently correlated to the amount of C12 stored. The medium loading of zeolite catalyst (D-0.5) displays a beneficial effect of the added zeolite, as it did not store so

much C12 to cause inhibition of the CO light-off beyond that of the base case D-0 catalyst. The highest loading of zeolite (D-1) with the most C12 stored results in greater inhibition, which overwhelms the beneficial benefit of added zeolite on CO light-off at the tested conditions. Species migration, in particular, can result in the additional stored C12 causing more inhibition on CO light-off during the temperature ramp.

Results for the CO light-off curves during the C12 co-feed condition compared to the CO-only feed are shown in Fig. 2.12. The medium zeolite loading is again shown to decrease the light-off temperature compared to the zeolite-free catalyst. The high zeolite loading follows the previous trend of increasing the light-off temperature, but now only to the point of matching the zeolite-free base case curve. The CO light-off results for the high zeolite loaded catalyst during the co-feed experiments had a larger amount of variability from run to run, and based on the standard deviations there was not a statistical difference between the zeolite-free and high zeolite loaded catalysts in terms of CO light-off temperatures during co-feed experiments. The medium loading zeolite, however, showed a clear improvement in CO light-off temperature during co-feed.

The previously described inhibition factors contribute to the stronger inhibitory effect during co-feed of C12 compared to when there is only pre-stored C12. When the C12 is co-fed with the CO there is a continual supply of C12 which maintains the coverage of C12 and increased extent of site blockage. During co-feed the C12 partial pressure remains higher and the pores are more likely to remain blocked. The overlap of the CO light-off curves for D-0 and D-1 catalysts during co-feed, in contrast to the increased inhibition displayed by the D-1 catalyst during pre-store experiments, may be due to relatively less inhibition due to the species migration factor. With a co-feed of

C12, the fresh supply of C12 can cause similar inhibition and may make the inhibition due to species migration either indistinguishable or irrelevant.

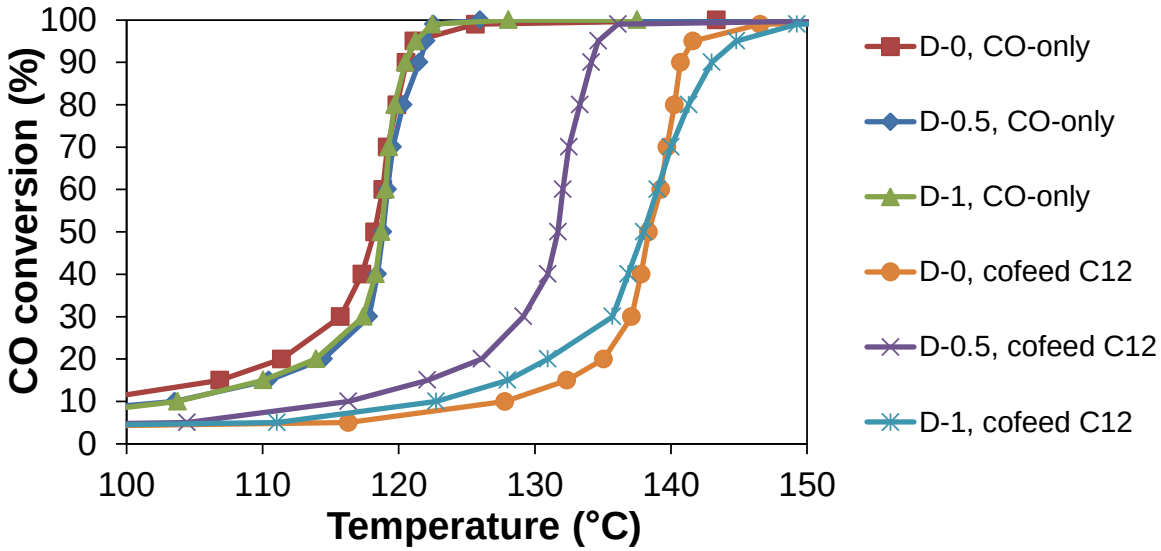

Figure 2.12 Comparing effect of co-feed 100 ppm C12 and 500 ppm CO light-off for D-0, D-0.5, and D-1 catalysts (10% O_2, GHSV=56,000 h^{-1}).

The catalyst temperature needed to achieve 50% conversion of 500 ppm CO (T_{50}) is listed in Table 2.2 for the different catalysts and experiments. These results reveal the main trends across all three types of experiments. Each catalyst follows the order co-feed C12 > pre-store C12 > CO –only. The light-off temperatures for CO-only experiments are essentially the same value (~119 °C) for all three zeolite loadings, as was shown in Fig. 2.5. The CO T_{50} for the pre-stored C12 are higher than those for CO-only runs, while the medium loading zeolite displayed the lowest T_{50} and the high loading zeolite displayed the highest T_{50}. The co-feed experiments, for which C12 was continuously fed with the CO, had the highest T_{50}, except the D-0.5 catalyst performed so well that the CO light-off temperature during co-feed (132 °C) is actually better than the D-1 catalyst CO light-off temperature during pre-stored experiments.

Table 2.2 Average temperatures to reach 50% conversion of 500 ppm CO

	CO T_{50} (°C)		
	CO-only	Pre-store C12	Co-feed C12
D-0	118	129	138
D-0.5	119	125	132
D-1	119	134	138

While the highest zeolite loading had a detrimental effect in terms of increased CO light-off temperatures during pre-store and co-feed experiments (Fig. 2.11 and 2.12), this sample also had the largest capacity for HC storage (Fig. 2.2). An analysis of the pre-storage transient data determines which catalyst converts the most HC to CO_2, a property that may have the most importance for the real world application. Listed for each catalyst sample in Table 2.3 are the amount of C12 stored, amount desorbed during the 30 min purge, amount of C12 desorbed during the temperature ramp, and finally the percentage of the initially stored HC that is converted to CO_2.

Table 2.3 C12 stored, desorbed, and converted during pre-storage experiments

	C12 (mg/g sample)				
	Stored	Desorbed (30 min purge)	Remaining after purge	Desorbed (temperature ramp)	Percent Converted
D-0	9.5	6.4	3.1	1.4	19
D-0.5	18.1	8.4	9.7	3.1	36
D-1	27.3	9.6	17.7	4.9	47

The base case D-0 catalyst stored 9.5 mg C12/g when saturated with a flow of 100 ppm C12. During the 30 min purge 6.4 mg C12/g desorbed, leaving 3.1 mg/g remaining on the sample. As the temperature increased during the CO light-off, an additional 1.4 mg/g desorbed, with the remaining C12 (1.7 mg/g) converted to CO_2. This corresponded to 19% of the initially stored C12 converted CO_2. Experiments run without CO in the

feed confirmed that the stored C12 did not partially oxidize to form CO during the temperature ramp under these lean conditions.

The catalyst samples containing zeolite had similar trends to those of the D-0 sample. The Table 2.3 data indicate that each of the metrics increased with zeolite loading. It was determined previously that increased zeolite loading increased the specific C12 storage capacity (Fig. 2.2). The current analysis indicates that the increase in stored C12 resulted in increased C12 desorption during the 30 min purge, from 6.4 mg/g for the base case to 8.4 mg/g for medium loading of zeolite to 9.6 mg/g for the high loading. The C12 desorption during the temperature ramp for CO light-off is likewise increased with higher zeolite loading.

The increased amount of C12 lost to desorption did not fully offset the increased amount of C12 initially stored. Thus, the percentage of stored C12 that converted to CO_2 increased with zeolite loading. The D-1 catalyst sample, which has the combination of highest storage capacity but also higher light-off temperatures, resulted in not only the largest amount of HC converted to CO_2 (12.8 mg/g), but also the highest percentage of originally stored HC converted to CO_2 (47%). The percentage HC converted metric is potentially more important than the CO light-off temperature in the optimization of the zeolite loading for the application.

2.5. Conclusions

An experimental study on Pt/Pd diesel oxidation catalysts containing varying amounts of zeolite beta (BEA) was carried out to investigate the effects of the zeolite on hydrocarbon storage, light-off temperatures and conversion of stored HC to CO_2. Increasing the loading of zeolite mixed into the washcoat layer of the monolith catalysts

subsequently increased the amount of dodecane storage capacity. The addition of zeolite did not have a notable effect on the light-off behavior for single component feeds of either CO or C12, as the curves essentially overlapped at the conditions used in this study. Pre-storing HC had an inhibitory effect on the CO-light-off and the co-feed of C12 and CO increased the CO light-off temperatures even further, a trend that was consistent across all three catalysts.

During co-feed and pre-storage experiments the medium loading of zeolite displayed a beneficial effect on the CO light-off, compared to the baseline zeolite-free catalyst, which is attributed to the zeolite providing alternative storage sites for the HC and therefore lessening the inhibition on CO oxidation. The catalyst with high loading of zeolite, however, resulted in no significant change in CO light-off during co-feed experiments compared to the baseline zeolite-free catalyst, and in fact showed a negative effect on CO light-off during HC pre-storage experiments. This adverse effect of high zeolite loading is ascribed to the further increase in HC storage, which has an inhibitory effect on the CO light-off, overwhelming the beneficial effect of zeolite observed for the medium loading zeolite. The catalyst with high zeolite loading did, however, demonstrate the largest percentage conversion of stored HC to CO_2 during the pre-store experiments.

These results illustrate that the zeolite loading level can be an important parameter to be mindful of during commercialization of real world applications. Demonstrated was a need to optimize the zeolite loading so that improvements in HC storage/conversion do not result in unacceptable light-off performance for other reactant species.

3. Propylene Oxidation Study with Development of Spaci-MS and Adaptation of Low-Dimensional Model

3.1. Introduction

Propene, also commonly called propylene, can be a very useful and desirable (valuable) chemical. It is the building block used in the production of polypropylene polymer, which reached a global annual production of 65 million tons in 2013 [84]. However, emissions of propylene to the environment are undesirable. Combustion engine exhaust contains a complex mixture of unburned hydrocarbons, the composition of which varies depending on the fuel type and engine technology, among other factors. Propylene typically makes up 5 - 10% of the total HC on a ppm C basis [9–11]. While low concentrations of propylene are not considered to be directly harmful to people (high concentrations are flammable and can be an asphyxiant), the propylene does react with NOx in sunlight to produce harmful ozone and smog [12, 13]. As described in Chapter 2, DOCs are utilized in the treatment of diesel exhaust and remove the unburned HCs by catalytic oxidation, emitting instead the more benign reaction products CO_2 and H_2O.

The complicated mixture of HCs in real engine exhaust is often simplified for research purposes to fewer but broader categories of HCs based on shared properties. The main groupings are typically comprised of alkanes (including methane, ethane, propane, etc), olefins (ethylene, propylene), aromatics (benzene, xylene), and aldehydes (formaldehyde, acetaldehyde). Propylene is often selected as the HC of choice when focusing on the lighter, more reactive portion of the exhaust HCs.

NOx abatement can be carried out using NOx storage and reduction (NSR) on lean NOx trap (LNT) catalysts, selective catalytic reduction (SCR), and their combination (NSR + SCR or LNT + SCR). Research at the University of Houston involving NOx

reduction has extensively studied NSR, SCR, and NSR + SCR. Some of these studies have involved propylene as a model reductant [85–90]. Additionally, oxidation of propylene on Pt/Al_2O_3 was studied by Joshi et al. [33], who utilized the recently developed low-dimensional (LD) theory [91–93] to simulate reactions in monoliths. The LD theory is the basis for an approximate yet simplified model compared to models comprising the complete set of partial differential equations. The LD model can provide results with the same qualitative behavior and an acceptable accuracy for practical applications, with particular utility for real time control.

The propylene oxidation study presented here uses conditions similar to those used in Chapter 2. A large excess of oxygen (10%) is again present in the feed stream (fuel lean). The same precious metal catalysts (Pt/Pd) are utilized, temperature is measured with type-K thermocouples, and gas hourly space velocity (GHSV) is 56,000 h^{-1}. Under these conditions it is anticipated that complete oxidation of propylene will occur and produce carbon dioxide and water according to

$$C_3H_6 + 4.5O_2 \rightarrow 3CO_2 + 3H_2O \,. \qquad (3\text{-}1)$$

Partial oxidation to carbon monoxide and hydrogen is also possible according to

$$C_3H_6 + 1.5O_2 \rightarrow 3CO + 3H_2 \,. \qquad (3\text{-}2)$$

However, partial oxidation is not expected unless the space velocity is extremely high or the O_2 concentration is very low (fuel rich).

An interesting and useful technique for acquiring spatially resolved measurements of gas species concentrations inside a monolith catalyst was developed by researchers at Oak Ridge National Lab [94, 95]. The spatially resolved capillary-inlet (Spaci) system can elucidate the progression of reactions through the length of the catalyst by measuring

the changing concentrations of reactants and products in situ, thereby reducing some of the usual speculation that is necessary in the absence of such information. The technique can eliminate the need for destructive testing whereby the catalyst sample is incrementally cut shorter in order to systematically build an understanding of the reactant profiles. For example, Clayton et al. [96] cut a Pt/BaO monolith into progressively shorter pieces to construct spatial profiles of concentration during NSR. Some contention on the magnitude of the error that is introduced by the invasiveness of the probe has arisen [97–99]. More elaboration on the Spaci technique and citations of additional studies performed by research groups employing spatially resolved techniques are contained in Chapter 5. It was decided that a single capillary should be constructed to increase the analytical capability of the experimental setup.

The first objective in this chapter is the construction of a spatially resolved capillary-inlet sampling system for in-channel concentration measurements. Next, a study on propylene oxidation is conducted and the newly built sampling technique is utilized. Finally, the low-dimensional model formulation of Joshi et al. [33] is adapted in order to simulate the propylene effluent conversions as well as model the propylene concentration profiles through the catalyst in order to compare the results to the experimentally obtained data.

3.2. Construction of Spatially Resolved Capillary-Inlet Measurement System

Design of the spatially resolved capillary-inlet (Spaci) measurement system was inspired by publications of Raimund Horn [100], Nick Degenstein [101], Allesandro Donazzi [102], and Brian Michael [103]; all former students of Dr. Lanny Schmidt at the University of Minnesota. Due to the gas flow requirements for acceptable FTIR

measurement performance, it was decided to use a mass spectrometer for the Spaci measurement system (although FTIR is possible [104, 105]). Another design consideration was to connect the capillary such that it will enter the reactor from the downstream end as depicted in Fig. 3.1. This minimized the likelihood of a leak around the capillary seal affecting the reactant mixture upstream of the catalyst.

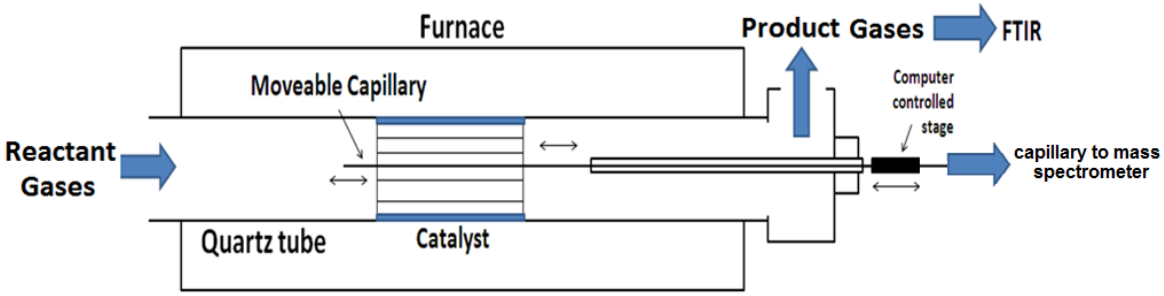

Figure 3.1 Schematic of spatially resolved capillary-inlet measurement system

A computer controlled moveable stage with 15 cm of travel (part# T-LSM150A-KT02) was ordered from Zaber Technologies Inc. (http://www.zaber.com/) of Vancouver, Canada, which is similar to the one used by Dr. Schmidt's research group. The moveable stage arrived in Houston and was installed downstream of the reactor with a custom bracket fabricated by Mr. Dave Perkins, shown in Fig. 3.2.

The Zaber stage can be moved by hand using a knob (turn left to retract, turn right to progress forward, speed depends on degrees turned) and also communicates via RS-232 connection to the Labview computer terminal. The device drivers and subVIs are available online (www.zaber.com/wiki/Software). When the stage is moved by hand the location updates in Labview in units of "counts" where 52,494 counts = 0.25 cm (the typical distance between measured points in this study).

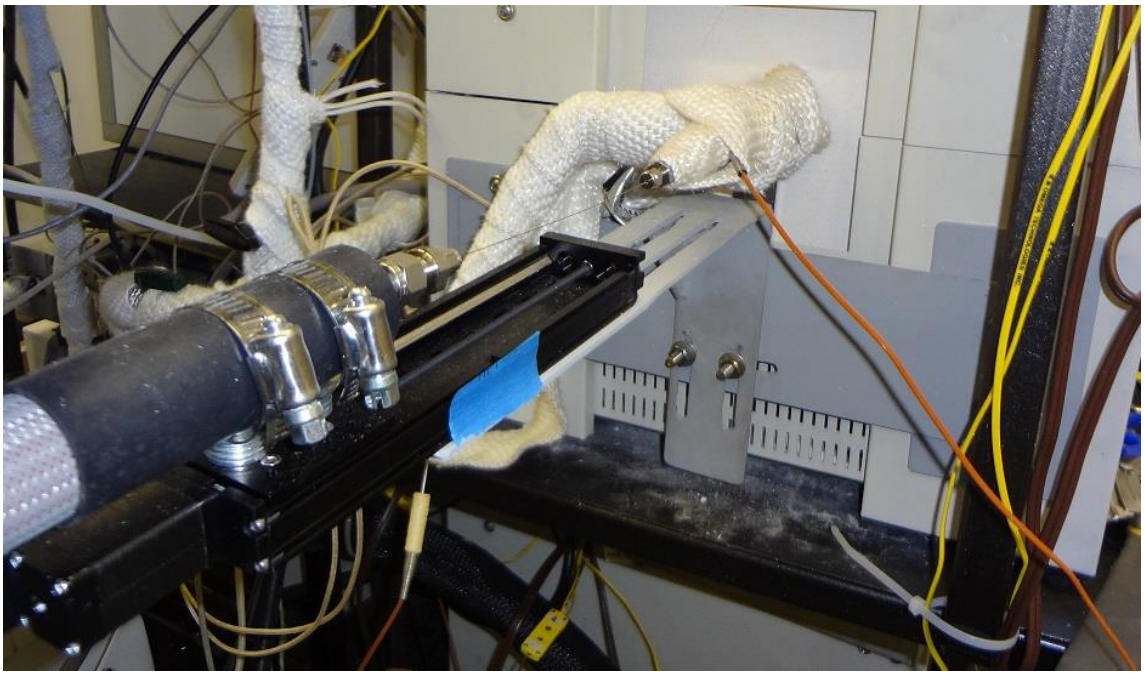

Figure 3.2 Computer controlled moveable stage mounted on custom bracket downstream of reactor

A Pfeiffer OmniStar GSD301 mass spectrometer was used for this study. Prior to the experiments the mass spec. was sent to Pfeiffer for modifications since it had been custom ordered with a special liquid sampling system. The mass spec. was converted to a ThermoStar, which includes a 1 meter long heated sample tube (up to 200°C) and a quartz capillary. The heated tube was attached to the moveable stage using band clamps as shown in Fig. 3.2. Swagelok compression fittings, vespel ferrules and a length of 1/8" stainless steel tubing were used to seal and guide the capillary's movement during reaction conditions.

The sample capillary included with the mass spec. after the refurbishment by Pfeiffer had an outside diameter (OD) of 0.22 mm and an inner diameter (ID) of 0.15mm. Initial attempts at using this capillary inside the reactor displayed that it was extremely fragile once the polyimide coating was removed (burned off) and the capillary broke so quickly that it was unusable. To increase the strength of the capillary, a larger OD

capillary but with identical ID to the prior one was ordered from SGE Inc. (fused silica deactivated tubing, 0.15 mm ID, 0.363 mm OD, 5 m length, part# 0624475). This OD matched that of the capillary used in the Hiden SpaciMS system [106] that had been recently installed in our lab. The ID for the replacement capillary remained the same as the original at 0.15 mm on recommendation from Pfeiffer engineers. If the ID were increased it would result in an increased gas flowrate to the mass spec. and possibly cause the turbo pump to overheat due to the increased pumping load.

The new larger diameter capillary was installed with the entire 5 m length coiled in the heated connection space, under the assumption that breaks would be inevitable. Uncoiling some additional length after a break is much easier than replacing an exact length of capillary and reconnecting the compression fitting with ferrules. One consequence that was not considered at the time is the possible impact of the length of the capillary on the sampling flow rate. A longer capillary might impact the response time of the analyzer by increasing the distance traveled between the sampling point and the analysis in addition to the issue of flow restriction. On the other hand, a lower gas sampling flow rate through the capillary may reduce suction effects on the results.

Testing the operation of the Spaci-MS system included calibrating the MS signal intensities for quantification of the measured species. This was done by first calibrating the MFC flowrate outputs using the Bios Drycal flow calibrators and then feeding several concentrations to the reactor. Propene is typically measured using m/e of 41 or 42, and as shown in Fig. 3.3. The MS signal intensities displayed good stair step behavior with very little drift as the propene concentration was incrementally decreased.

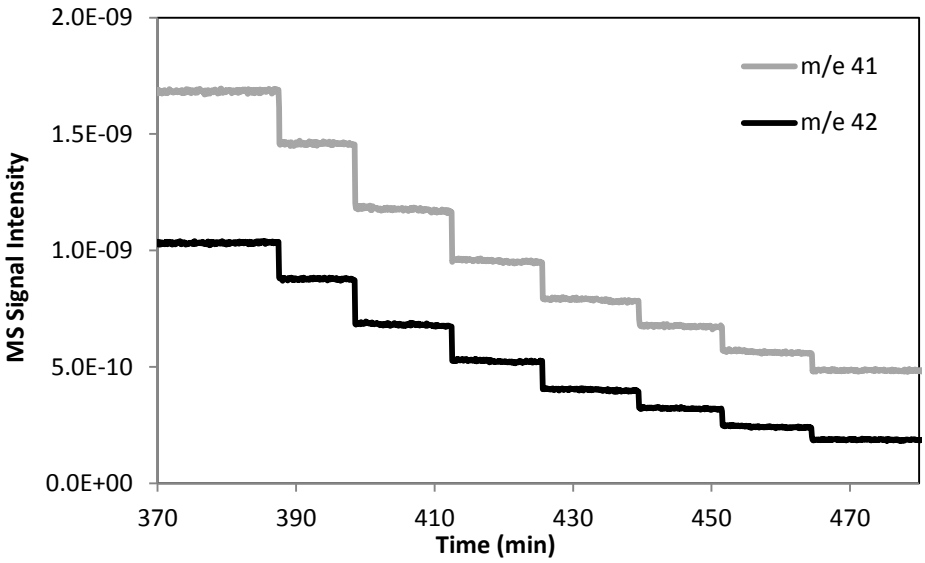

Figure 3.3 Pfeiffer MS signal intensities for m/e 41 and 42 during propene calibration

The calibrations were very linear, with the propene calibrations corresponding to Fig. 3.3 shown as Fig. 3.4. From this point only m/e 41 was used to quantify propene based on the slightly increased signal strength compared to the m/e 42 signal. That the m/e 41 signal had a non-zero intercept does not matter once it is accounted for, as it is merely an artifact of the zeroing procedure in the mass spec software. The species calibrations were performed each day prior to testing due to the potential for drift in the MS signals. Depending on the length of time required to complete the testing the calibrations were additionally done during and after testing was completed for lengthy tests.

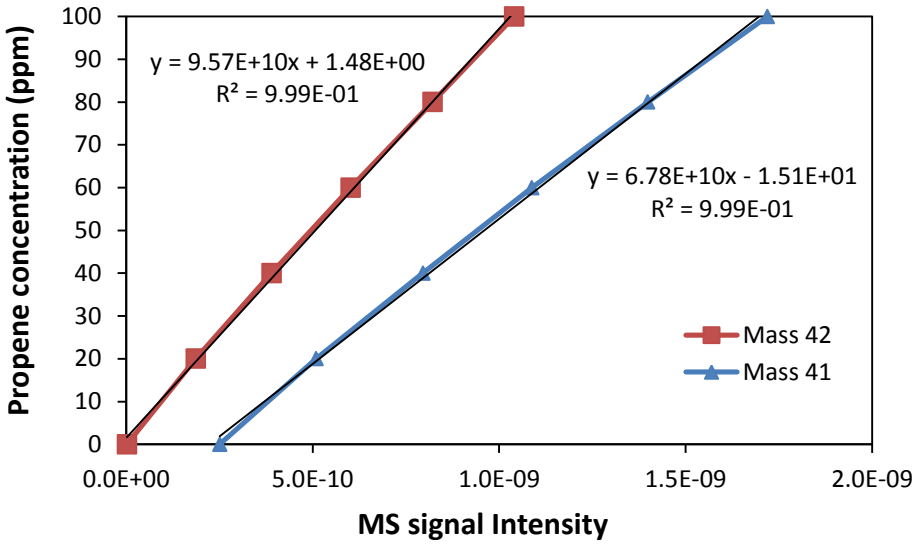

Figure 3.4 Propene quantification calibration linearity check

Initial measurements of propene concentration down the length of the catalyst while under reaction conditions were successful. Data presented in Fig. 3.5 were acquired while feeding a constant propene feed of 100 ppm at a temperature of 150 °C (with 10% O_2 and total flowrate 3000 sccm). At the 360 min mark the capillary was extended all the way through a central channel of the monolith and protruding 0.25 cm in front of the front face of the catalyst. At 370 min the capillary was pulled back to be even with the front of the monolith, and, as expected, there was no change in the signal intensity. At 387 min the capillary was moved such that it sampled from 0.25 cm inside the catalyst and a decrease in signal intensities for m/e 41 and 42 were recorded within a few seconds, which displayed good response time. In intervals of roughly 10 minutes the capillary was incrementally withdrawn through the catalyst and the signals in turn decreased.

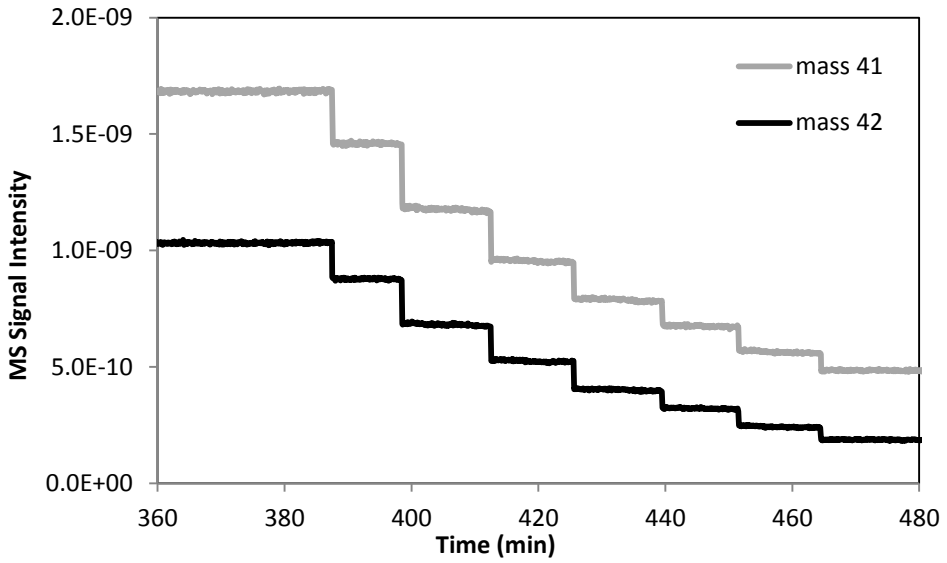

Figure 3.5 Signal intensities as capillary incrementally moved through D-0 catalyst at 150°

The average signal intensity was taken across each steady-state position and converted to the propene concentration value using the constructed calibration relation. The conversions were then determined using the measured concentrations and the 100 ppm propene feed concentration, which produced the propene conversion profile in Fig. 3.6. As shown in the figure, most of the conversion occurred in the front portion of the monolith, with 50% conversion achieved at 0.75 cm from the front face. That the conversion did not change between the 2.5 cm and 2.75 cm measurement points is important. The catalyst was only 2.54 cm in length, so the final measuring point was in fact behind the catalyst and no longer in the monolith channel. That the measurement did not change once the capillary probe was removed from the channel may indicate that the capillary was not overly intrusive. It may also indicate that the particular channel being measured did not differ significantly from the other channels, notwithstanding the possibility that the effluent stream was not fully mixed yet at that location. Another indicator that the system was working well was that the final propene conversion

measurement of 88% by the Spaci-MS compared well with the FTIR measurement of the reactor effluent at 90% propene conversion. This final measurement check behind the catalyst was not done often, however, due to the difficulty in reinserting the capillary into the correct monolith channel.

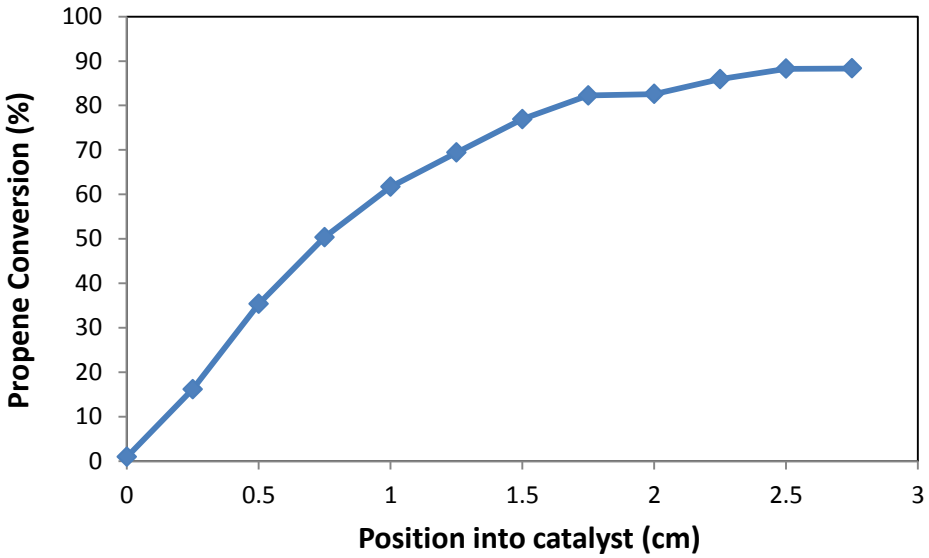

Figure 3.6 Propene conversion profile through the length of the catalyst

This initial testing of the single capillary Spaci-MS system indicated that it was working as designed. Periodic monitoring of the system for acceptable performance was done continuously to ensure accuracy of the results moving forward. The next step involved performance studies on propene oxidation utilizing temperature ramps for light-off determination as well as steady-state measurements with varying propene concentrations.

3.3. Propene Oxidation Light-off by Temperature Ramp

Temperature ramp procedures similar to those utilized in Chapter 2 were carried out to determine light-off temperatures for several feed concentrations of propene. As mentioned in Chapter 2, the use of a temperature ramp may give different results from steady-state operation due to inherent transient conditions and associated thermal and

chemical species accumulation effects. These experiments utilized a relatively slow ramp rate of 1°/min, which at the time were thought to increase the accuracy of the measurement of the temperature at which 50% conversion (T50) was reached. All reported temperatures in this chapter refer to the catalyst temperature, as measured by the thermocouple placed at the approximate midpoint of the catalyst sample.

Two catalyst samples were tested by this method, D-0 and D-0.5 (catalyst details in Chapter 2), the results of which are shown in Table 3.1. With a propene feed concentration of 50 ppm the light-off was achieved between 90 and 100 °C depending on the catalyst sample. The light-off temperatures increased from this point as propene feed concentration was increased and this indicated that the overall reaction order with respect to propene may be negative. Further analysis is needed to confirm this using steady-state data (see section 3.4 below). Notably, the D-0.5 catalyst sample with 0.5 g/in^3 zeolite mixed in the washcoat consistently displayed a lower propene oxidation light-off temperature than the D-0 zeolite-free catalyst sample.

Table 3.1 Light-off temperatures for propene oxidation by temperature-ramp method

	T50 (°C)	
Propene Feed (ppm)	**D-0**	**D-0.5**
50	97	90
100	111	105
200	136	129
400	160	147

It was initially thought that the zeolite component may inhibit the activity of the PGM and the light-off temperatures would subsequently increase. Results of these experiments, however, indicate that light-off temperatures are reduced for propene oxidation with zeolite in the washcoat. This interesting effect was also noted in Chapter 2

during dodecane oxidation. As stated in the previous chapter, the increase in zeolite loading and the accompanying increase in washcoat thickness might be presumed to increase the diffusional resistance and thus reduce the reaction rate; however under the current experimental conditions the zeolite was beneficial.

The beneficial effect of additional zeolite on HC light-off temperatures is attributed to the zeolite increasing the transport of oxygen and hydrocarbons on the surface and decreasing the extent of inhibition caused by propylene site blocking. The synergy effect between catalyst and zeolite due to increased O_2 mobility and storage was reported on by Maupin et al. as it applies to VOC catalytic combustion [107]. In the case of propene, the acidic nature of the zeolite may also be creating hydrocarbon species on the surface that are in some way "activated", which lead to oxidization reactions at a lower temperature.

3.4. Steady-State Propene Oxidation Kinetics

Steady-state propene oxidation experiments were performed using the D-0 (no zeolite) catalyst sample. The conversion dependence on temperature for several feed concentrations (50, 100, 200, and 400 ppm) are shown in Fig. 3.7. The resulting light-off temperatures (T50) during steady-state were moderately increased compared to the temperature ramp experiments. For example, 50% conversion was attained at approximately 120 °C for 50 ppm feed under steady-state conditions, but this conversion was reached at 97° during the temperature ramp. The differences in light-off temperatures between steady-state experiments and temperature ramp experiments indicates there are transient effects at play even at the slow ramp rate of 1 °C/min (other chapters in the

dissertation used a ramp rate of 3 °C/min). Further experiments to help elucidate the nature of those effects have not been performed as of yet.

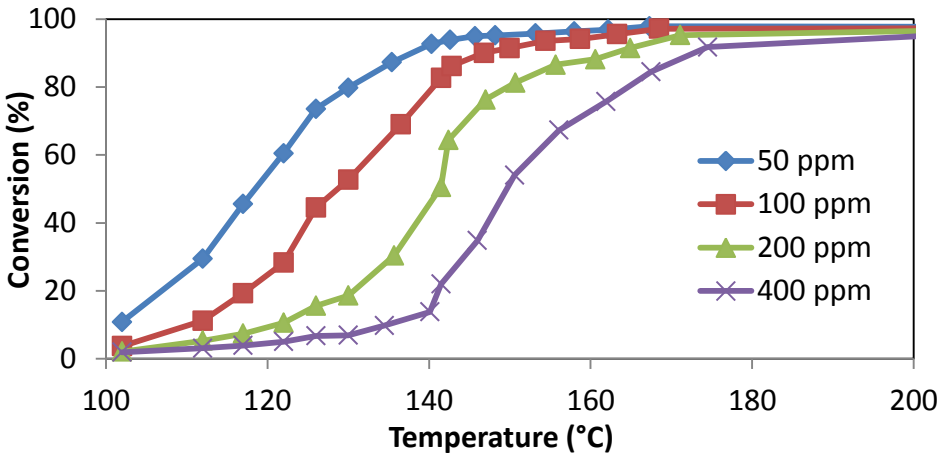

Figure 3.7 Steady-state propene oxidation with D-0 catalyst, GHSV = 56,000 hr^{-1}, 10% O_2 (balance Ar), propene feed = 50, 100, 200, 400 ppm

Data at low conversion were used to determine reaction kinetics under conditions of negligible mass transfer limitations. The kinetics will then be used as a baseline for the modeling study shown below. Figure 3.8 shows the dependence of propene feed concentration on rate (mole reacted/mole PGM/sec). As reported in the figure, the reaction is of negative order with respect to propylene ($n \approx -0.5$) at these temperatures. This compares to n = -0.88 reported by Joshi et al. [33] for propene oxidation on Pt.

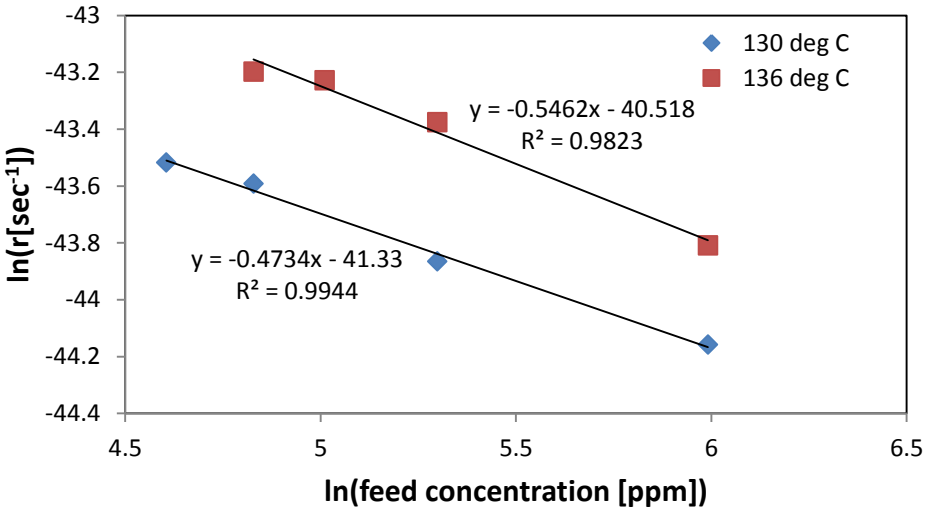

Figure 3.8 Determination of propene oxidation reaction order

Using the power law model, the apparent activation energy can be estimated by plotting the rate constant as a function of temperature according to $r = k_{app}C^n$, where C is concentration of propene in ppm and k_{app} is the apparent rate constant (an Arrhenius plot). As shown in Figure 3.9, the apparent activation energy (E_a) is found to be 109.8 kJ/mol (E_a/R = 13205 K). This compares to the Joshi et al. finding of E_a = 73.3 kJ/mol for Pt [33].

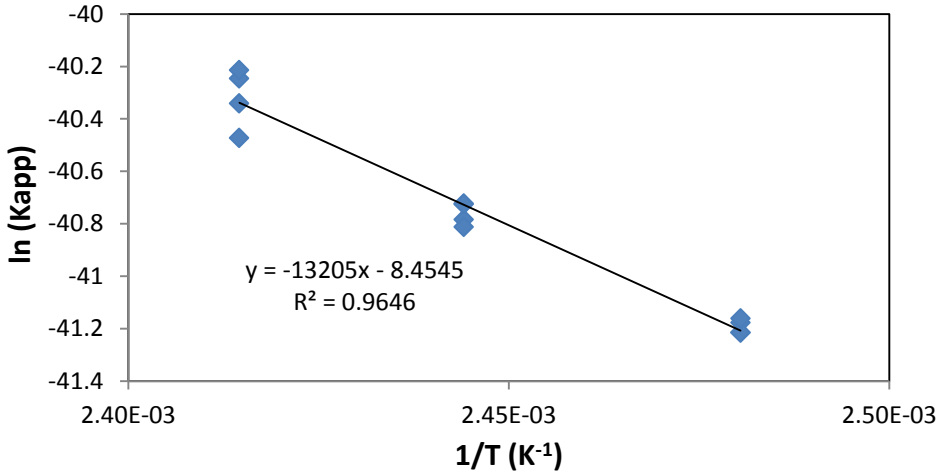

Figure 3.9 Arrhenius plot for determination of activation energy

3.5. Steady-State Propylene Oxidation Spatially Resolved Measurements

The Spaci-MS measurement capability was utilized for the same reaction conditions as during the steady-state propene oxidation experiments. The capillary was first aligned with the front face of the catalyst sample. Once the temperature had stabilized, the capillary was pulled back through the catalyst using the motorized stage at ¼ cm intervals. Measurements were taken for 10-15 min and then an average was taken over each corresponding stable period. For the first set of spatially resolved experiments, this procedure was repeated at increasing temperatures with a feed concentration of 100 ppm propene and 10% O_2. The results are displayed in Fig. 3.10.

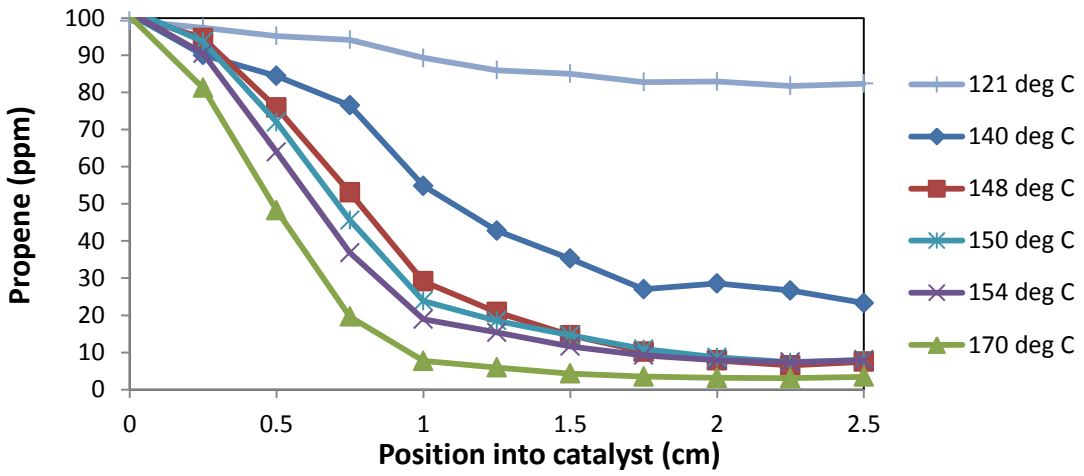

Figure 3.10 Concentration dependence on temperature for 100 ppm propene feed

At the entrance (0 cm position) the capillary probe was flush with the catalyst face and, as expected, the measured propene concentration was always 100 ppm, matching the feed concentration. At a catalyst temperature of 121 °C, the lowest temperature tested for the Spaci measurements, the propene oxidation reaction occurred at a relatively low rate. The measured concentration slowly decreased along the length of the channel, reaching 82 ppm near the exit (2.5 cm position). Increasing the temperature to 140 °C caused the

reaction rate to increase appreciably and, as shown in the figure, the propene concentration was reduced to 23 ppm by the 2.5 cm mark. The Spaci-MS measurements enabled the detection of the location through the catalyst where the light-off (>50% conversion) occurred, and at 140 °C it did so by the halfway point, reaching 43 ppm at the 1.25 cm mark.

A further increase in temperature to 148 °C increased the reaction rate further with the propene concentration decreasing more steeply, as shown in Fig. 3.10, especially in the front ~1 cm section of the catalyst. The propene concentration fell to 29 ppm by the 1 cm mark followed by a more gradual decline, reaching 8 ppm by the furthest downstream measurement at 2.5 cm. Small increases in temperature to 150 °C and 154 °C displayed detectable decreases in propene concentration, especially between 0.25 cm and 1.75 cm. That the Spaci system can make these measurements precisely enough that the correct trend is followed is a testament to its utility, as these measurements were in fact separated by a few hours of operation.

At the highest temperature considered (170 °C) the propene concentration was reduced to 48 ppm by 0.5 cm into the catalyst, and a further decrease to a mere 8 ppm by the 1 cm mark. The propene oxidation reaction is clearly strongly temperature dependent and Spaci-MS measurement follows the expected trends with few aberrations. Only 50 °C separated the lowest temperature (121 °C) when propene oxidation was just beginning and only reached 20% conversion in the effluent, from the highest temperature, where light-off (>50% conversion) had occurred by 0.5 cm into the catalyst.

The next set of spatially resolved experiments involved feeding several different concentrations of propene (50, 100, 200, 400 ppm) with measurements taken at

temperatures of 140 °C, 148 °C, and 170 °C. The results are in general predictable, but a few interesting features are notable. The propene concentration profiles at 140 °C are displayed in Fig. 3.11. The measurements taken at the catalyst entrance (0 cm into catalyst), shown on the far left hand of the figure, match the corresponding propene feed concentrations. As the capillary was moved through the length of the catalyst the measured propene concentrations decreased as the propene was being consumed by the oxidation reaction. (The 100 ppm profile is the same data as was shown in Fig. 3.10, but now appears more flattened since the Y-axis is expanded.) The four feed concentration profiles appear to have very similar shapes and slopes, although the 50 ppm feed is completely consumed by 1.25 cm and cannot decrease further.

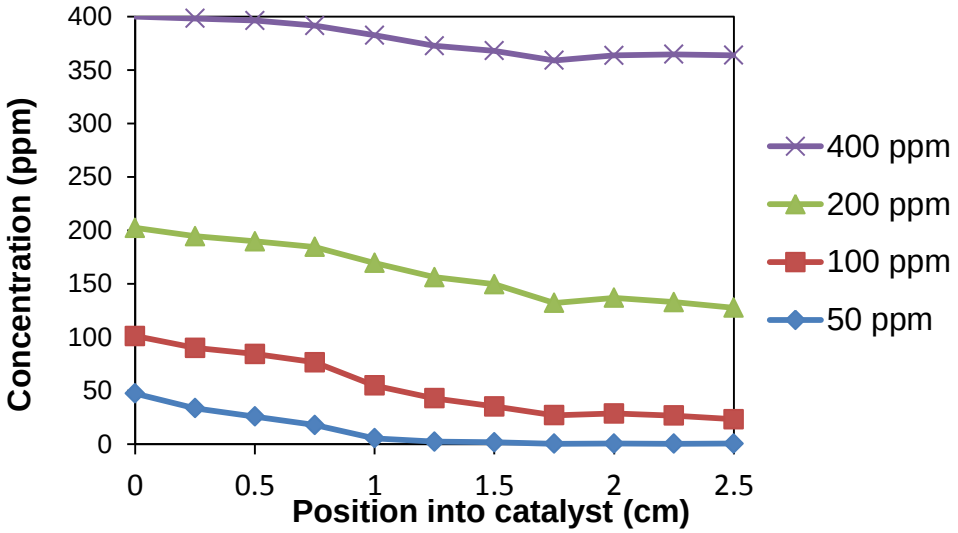

Figure 3.11 Propene concentration measurement profiles at 140 °C

The corresponding conversion profiles are shown in Fig. 3.12. At first glance they seem to paint a different picture. The behavior of the conversion profile for 50 ppm makes it appear much more active than the 400 ppm feed; however it is mostly due to the relative amount of propene that must be reacted to produce the corresponding percentage change in conversion. For instance, a reduction of 25 ppm is equivalent to 50%

conversion with a feed of 50 ppm; however the same 25 ppm reduction is only ~6% conversion for a 400 ppm feed.

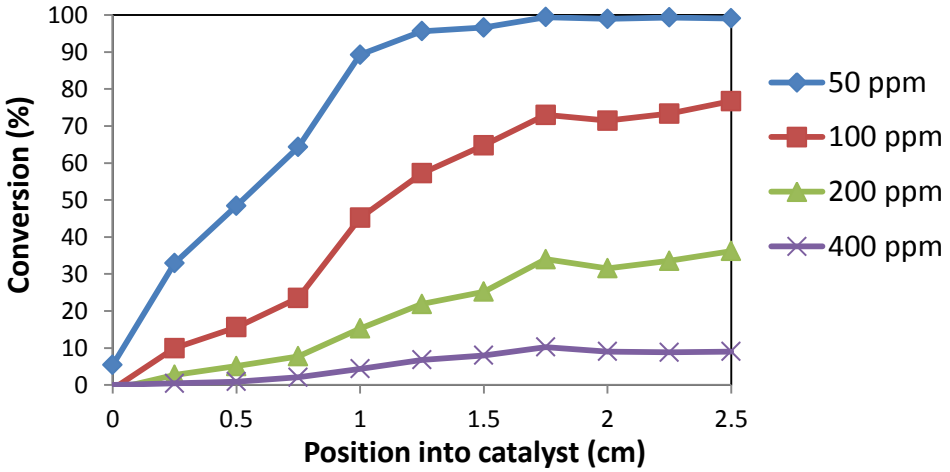

Figure 3.12 Propene conversion profiles at 140 °C

The relative ordering of the conversion profiles in Fig. 3.12 will be displayed by any nonreversible reaction with a rate that can be approximated by the power law, $r = k_{app}C^n$, and n is less than 1 (<1st order). This is due to the instantaneous rate of the reaction being based on the reactant concentration. When the reactant feed concentration is changed, for example doubled from 100 ppm to 200 ppm, the rate must also double in order to produce an equivalent conversion. That is the case for a first order reaction ($200^1/100^1 = 2$) but a lower order (e.g. 0.5) results in less of a rate increase ($200^{0.5}/100^{0.5} = 1.41$). Thus, absent mass transfer limitations and heat effects, the feed containing increased reactant concentration will not catch up to the lower concentration in terms of conversion.

Another format of plotting the data is in terms of the concentration of propene reacted as shown in Fig 3.13. As was determined by the Arrhenius plot (Fig 3.7), the order of the reaction is roughly -0.5 with respect to propene concentration. The negative

order dependence is evident within the channel in Fig 3.13. In the front 1 cm the 50 ppm feed profile clearly reacts the fastest, outpacing all other reactant feed levels. This result could not be measured at these conditions without the capillary probe, unless the catalyst were physically removed and cut shorter. The 100 ppm feed catches up to and surpasses the 50 ppm feed further down the channel, between 1.0 and 1.25 cm, since it is not possible for the 50 ppm feed to react more feed than was supplied. The 200 ppm feed catches up still further down the channel and the 400 ppm feed never reached 50 ppm reacted at this temperature.

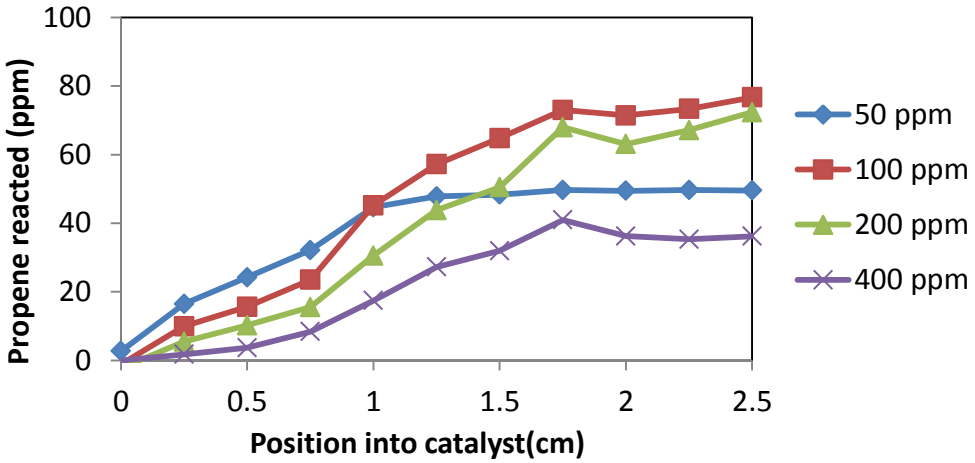

Figure 3.13 Amount reacted (ppm) for several propene feed concentrations at 140°C

When the temperature was increased to 148 °C the rate of propene oxidation likewise increased. The concentration and conversion profiles look similar to Fig. 3.11 and Fig. 3.12, except that the concentrations decline a bit more steeply and conversion rises more quickly through the length of the monolith, however the shape and ordering remain the same. More interesting are the profiles for amount of reactant consumed for each feed concentration. At this condition, the 200 ppm feed profile surpassed the 100 ppm feed in terms of total amount reacted by the 1 cm mark, as shown in Fig. 3.14. The

400 ppm feed catches up to the 100 ppm feed near the end of the monolith, reacting a total of 102 ppm by the 2.5 cm mark.

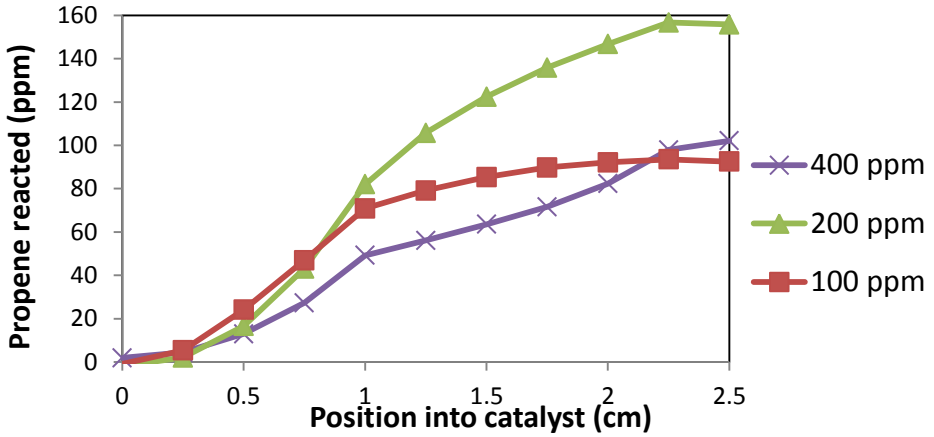

Figure 3.14 Amount reacted (ppm) for several propene feed concentrations at 148 °C

When the temperature was further increased to 170 °C, the concentration profiles become notably less linear, reacting the bulk of the feed in the first half of the catalyst, as displayed in Fig. 3.15. The corresponding conversions are displayed in Fig. 3.16. This is still a relatively low temperature compared to real world exhaust treatment conditions; however the 400 ppm propene feed still reaches 86% conversion. The profiles for amount of reactant consumed are displayed in Fig. 3.17. Under these conditions the negative order dependence on propene concentration is no longer clearly evident.

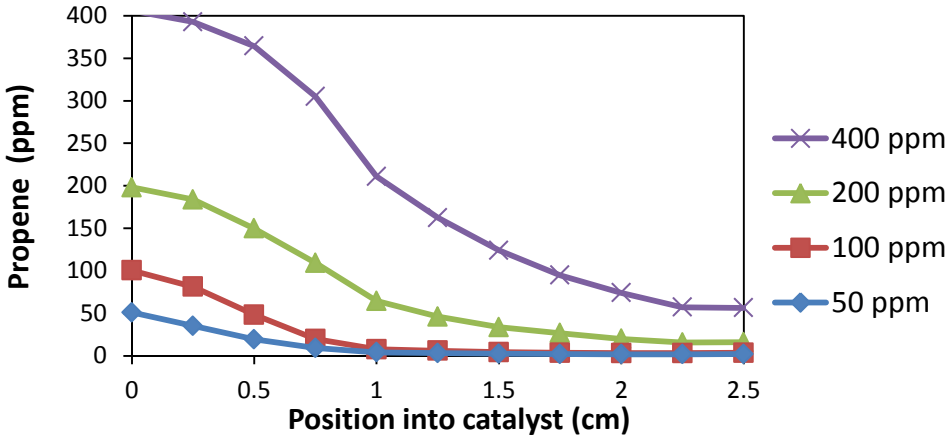

Figure 3.15 Propene concentration measurement profiles at 170 °C

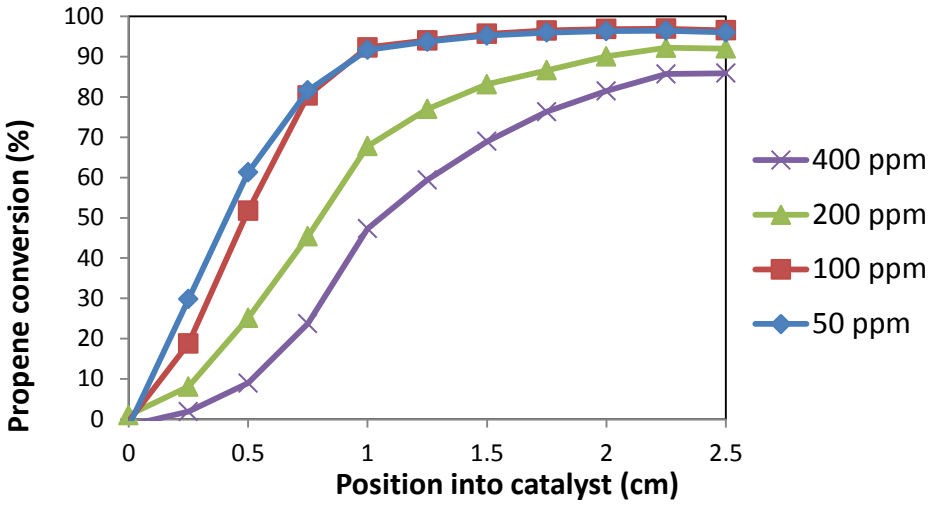

Figure 3.16 Propene conversion profiles at 170 °C

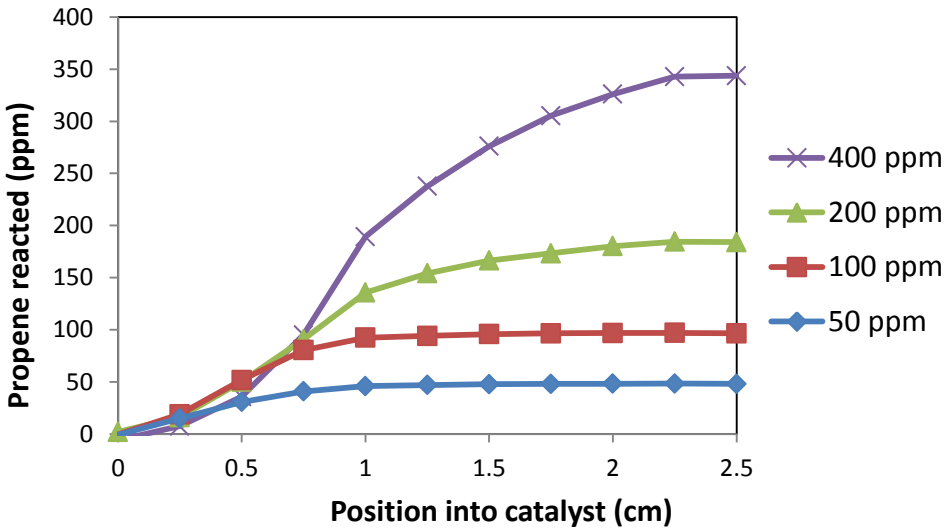

Figure 3.17 Amount reacted (ppm) for several propene concentrations at 170 °C

3.6. Application of Low-Dimensional Model

Research carried out by former graduate student Dr. Saurabh Joshi (now with Cummins) led to development of the Low-Dimensional Model formulation [91–93]. The Low-D Model approach was applied to oxidation of methane and propylene on Pt washcoated monoliths [33]. As mentioned in the chapter Introduction, the LD model is simplified compared to full partial differential equation (PDE) models, but it can provide

results with the same qualitative behavior and an acceptable accuracy for practical applications. The equations utilized by the LD model include the gas phase species balance Eq. (3-3), the local Eqs. (3-4, 3-5), and the inlet condition Eq. (3-6), and are as follows:

$$\langle u \rangle \frac{dC_{fm}}{dz} = -\frac{1}{R_{\Omega_1}} k_{me} \left(C_{fm} - C_s \right), \tag{3-3}$$

$$k_{mi} \left(C_s - \langle C_{wc} \rangle \right) = R_{\Omega_2} R\left(\langle C_{wc} \rangle \right), \tag{3-4}$$

$$k_{me} \left(C_{fm} - C_s \right) = k_{mi} \left(C_s - \langle C_{wc} \rangle \right), \text{ and} \tag{3-5}$$

$$C_{fm} = \alpha_1 C_{in} \;\; ; \quad z = 0 . \tag{3-6}$$

The mass-transfer coefficients k_{me} (external) and k_{mi} (internal) are calculated according to

$$k_{me}(z) = \frac{Sh_e(z) D_f}{4 R_{\Omega_1}} \text{ and} \tag{3-7}$$

$$k_{mi} = \frac{Sh_i D_e}{R_{\Omega_2}} . \tag{3-8}$$

The reactant diffusivity in the gas phase, D_f, was estimated by Joshi using Lennard-Jones potentials and depends on temperature:

$$D_f = 4.237 x 10^{-10} T^{1.7844}. \tag{3-9}$$

while the reactant diffusivity in the washcoat, D_e, is correlated to D_f with a diffusivity ratio:

$$D_e = D_f / B. \tag{3-10}$$

The diffusivity ratio, B, was tuned in the previous publication [33] and found to be equal to 10. This value also showed to be a good fit for the current study. The external and

internal Sherwood numbers, Sh_e and Sh_i, respectively, are from the work of Balakotaiah and West [108] (following Joshi's example):

$$Sh_i = 2.65 + \frac{0.58\Phi_g{}^2 Sh_e}{1 + 0.58\Phi_g} \text{ and} \tag{3-11}$$

$$\Phi_g{}^2 = 2R_{\Omega_2}^2 \frac{\int_0^{C_s} R(C')dC'}{D_e C_s{}^2}. \tag{3-12}$$

Table 3.2 lists the nomenclature used in the LD model equations.

Table 3.2 Nomenclature for LD model equations

$\langle u \rangle$	average gas velocity in the channel [m/s]
C_{fm}	cup-mixing concentration in fluid phase [mol/m^3]
C_s	fluid-washcoat interfacial concentration [mol/m^3]
$\langle C_{wc} \rangle$	volume averaged concentration in the washcoat [mol/m^3]
D_f	molecular diffusivity of the reactant in fluid phase [m^2/s]
D_e	effective diffusivity of the reactant in the washcoat [m^2/s]
B	diffusivity ratio (D_f/D_e)
k_{me}	external mass transfer coefficient from the bulk of fluid phase to fluid-washcoat interface [m/s]
k_{mi}	internal mass transfer coefficient between the interior of the washcoat and fluid- washcoat interface [m/s]
R_{Ω_1} (R_{Ω_2})	effective transverse diffusion length for flow (washcoat) area [m]
Sh_e	external Sherwood number
Sh_i	internal Sherwood number
R	reaction rate calculated per unit catalyst phase (washcoat) volume [mol/m^3/s]
$x_{C_3H_6}$	mole fraction of propylene
z	axial coordinate [m]
α_1	first normalized Fourier weight
Φ_g	generalized Thiele modulus

The computer source code was acquired from Dr. Joshi and implemented using Matlab. The code was confirmed to be working correctly by recreating a previously published result (Fig. 1 from Joshi et al. [33]). To extend this model to the current Pt-Pd catalysts modifications needed to be made to the Matlab code. (Previous experience with C++ programming was greatly beneficial in this endeavor, as very limited commenting was included with the code.)

The first step in adapting the low dimensional model to the current application was changing several parameters to match the current experimental setup. This included the catalyst length, z (from 4 cm to 2.54 cm), the average gas velocity in the monolith channel, $< u >$ (depends on space velocity and temperature), and the propene feed concentrations. The present experimental setup used a larger diameter quartz tube reactor, and therefore used a monolith catalyst with a larger number of channels when testing a catalyst with the same substrate cell density. Despite the different experimental setup, the average gas velocity changed little, from 0.49 m/s to 0.53 m/s at 273 K.

Since this was a different catalyst sample than was used by Joshi, the kinetic parameters needed to be tuned to account for the different catalytic activity. The fitting was done by trial and error. A change was made to the value of a constant variable, the model was run, the new output was observed and the next change was made. It was first considered that it might be necessary to incorporate two rate equations to model the experimental data since the current catalyst has two active metals, Pt and Pd, rather than monometallic Pt. This increased the complexity and the attempts at fitting proved nontrivial. The single rate equation was reverted to and manipulation of the rate constants

and adjustments to the diffusivity ratio (B) and the apparent Sherwood number led to satisfactory results being obtained. The final rate expression is

$$R = \frac{2x10^{14} \exp\left(-\frac{10500}{T}\right) x_{C_3H_6}}{[1+150\exp\left(\frac{500}{T}\right) x_{C_3H_6}]^2},$$

with a table of the parameter values shown in Table 3.3.

Table 3.3 Model parameter values

Q	3000 sccm
$x_{C_3H_6}$	50, 100, 200, 400 ppm
L	0.0254 m
cpsi	400
$\langle u \rangle$	0.5298*T/298
R_{Ω_1}	0.275 mm
R_{Ω_2}	25 μm
Sh_e	1.8
B	10

The model results are shown in Fig. 3.18. The data points marked by symbols are from the FTIR measurement data, while the lines are the LD model predictions. It is considered to be a fairly good fit, capturing the S-shaped light-off features and alignment with the different feed concentrations.

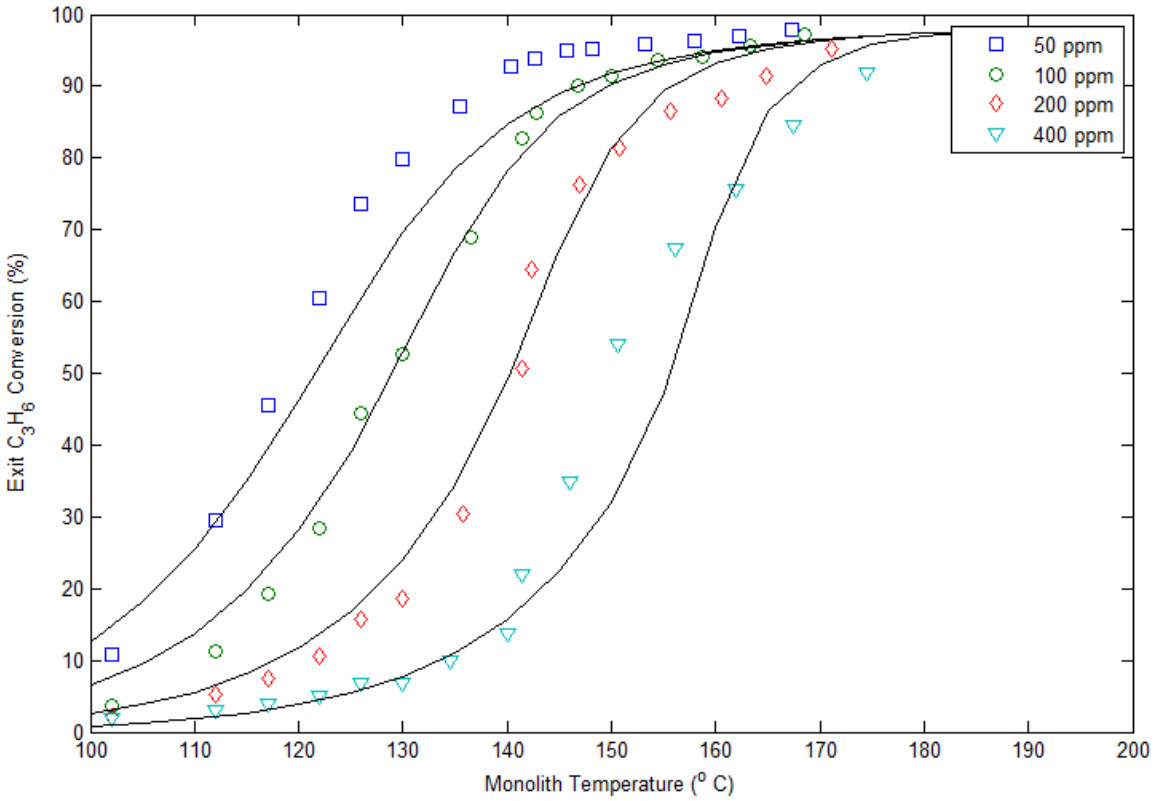

Figure 3.18 Propylene exit conversions with markers for experimental data and curves from model

The Matlab code was then used to predict the propene concentrations along the length of the catalyst at several temperatures. No additional parameter fitting was done. Shown in Fig. 3.19 are the model predications compared to the Spaci-MS results at 140 °C. The almost linear, nearly parallel profiles as the concentration decreases through the length of the catalyst channel match well.

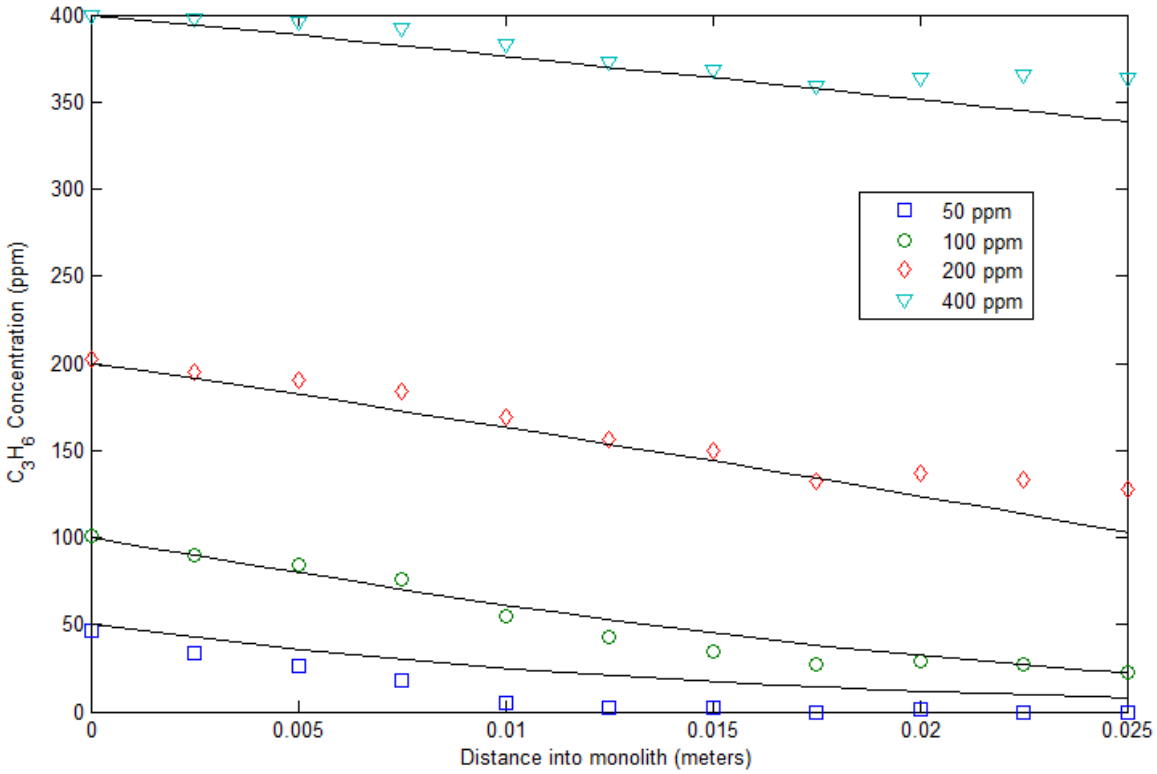

Figure 3.19 Propylene concentrations with markers for experimental data and curves from model at 140 °C

The results for the increased temperature of 148 °C are displayed in Fig. 3.20. Again, the experimentally obtained data matches fairly well with the model results. Matching especially well is the 400 ppm feed concentration profile. The modeled data for 200 ppm and 100 ppm show a more linear decrease through the length of the channel compared to a more complex experimental data behavior. The experimental measurements display a slight lag in the propene concentration decrease compared to the model near the entrance, then an increase in reation rate causing the concentrations to fall below the model by the 1 cm mark. This is followed by a slowing of the rates in the back portion of the monolith, resulting in final propene concentrations that match.

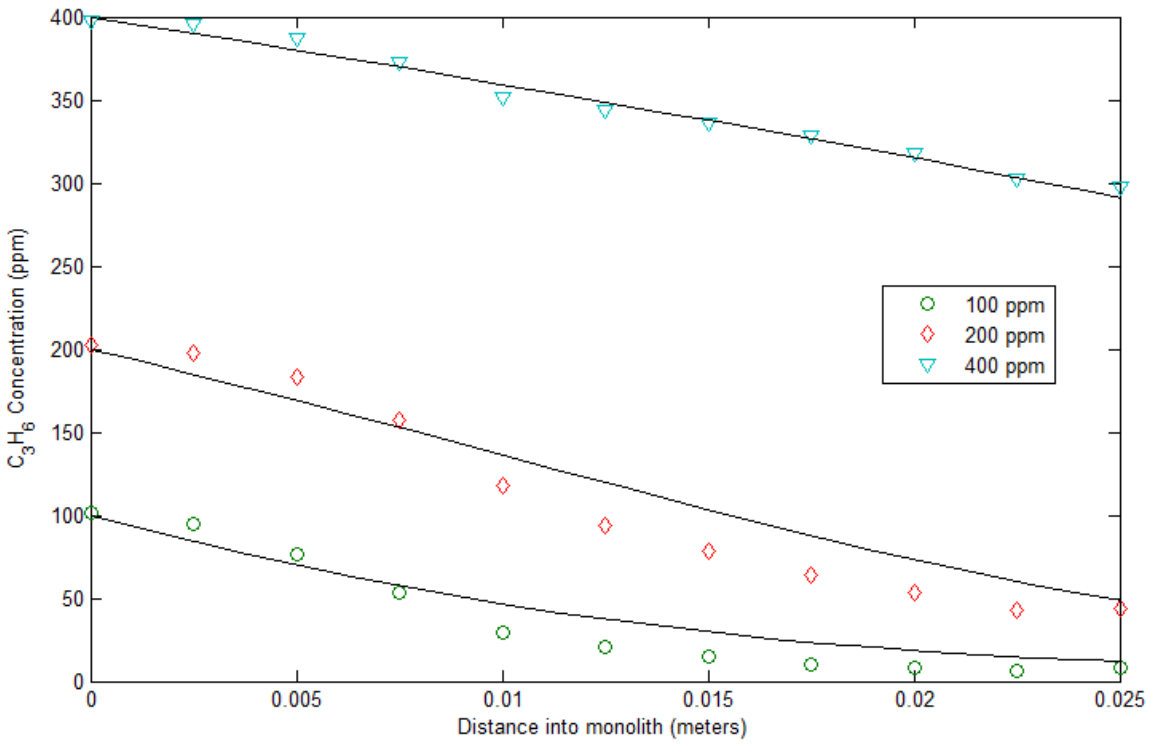

Figure 3.20 Propylene concentrations with markers for experimental data and curves from model at 148 °C

Finally, the modeled concentration profiles through the length of the catalyst at 170 °C are shown in Fig. 3.21. At this increased temperature the modeled results take on a more nonlinear shape for higher propene feed concentrations and overall make a fairly good fit to the experimental data.

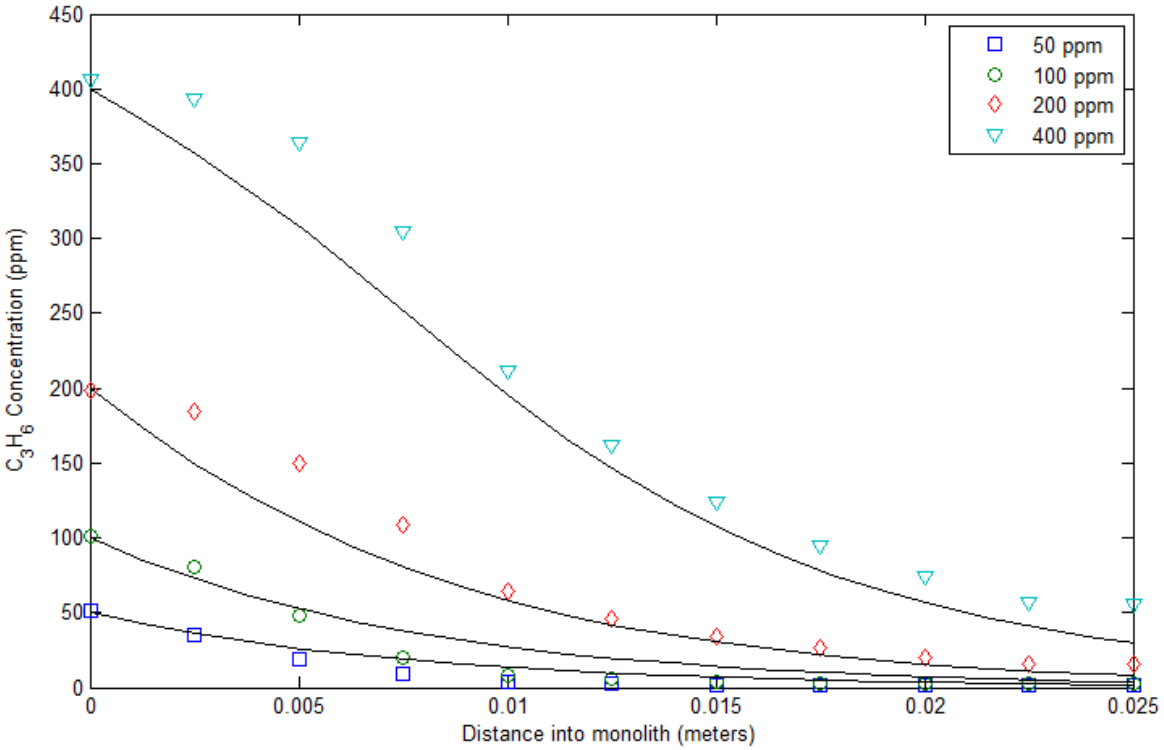

Figure 3.21 Propylene concentrations with markers for experimental data and curves from model at 170 °C

To provide insight into the extent of mass transfer limitations the modeled surface concentrations (Cs) and washcoat concentrations (Cwc) are plotted in addition to the cup-mixing concentration (Cfm). This is done for inlet concentrations of 400 ppm and 100 ppm at 148 °C in Fig. 3.22 and at 170 °C in Fig. 3.23. According to the criteria of Joshi to determine which controlling regime is present, Cfm/Cs ≤ 1.1 and Cs/Cwc ≤ 1.1 in the kinetic regime, while Cfm/Cs ≤ 1.1 and Cs/Cwc ≥ 10 for the washcoat diffusion regime, and Cfm/Cs ≥ 10 and Cs/Cwc ≥ 10 in the mass transfer controlled regime. At 148 °C the model indicates it is in the kinetic regime, but approaching the washcoat diffusion regime, as Cfm/Cs ranges from 1.1 to 2.5 and Cs/Cwc ranges from 1.0 to 1.4. At 170 °C Cfm/Cs ranges from 1.4 to 4.7 and Cs/Cwc ranges from 1.1 to 2.0, so it is still transitioning from the kinetic regime to the washcoat diffusion or mass transfer regime.

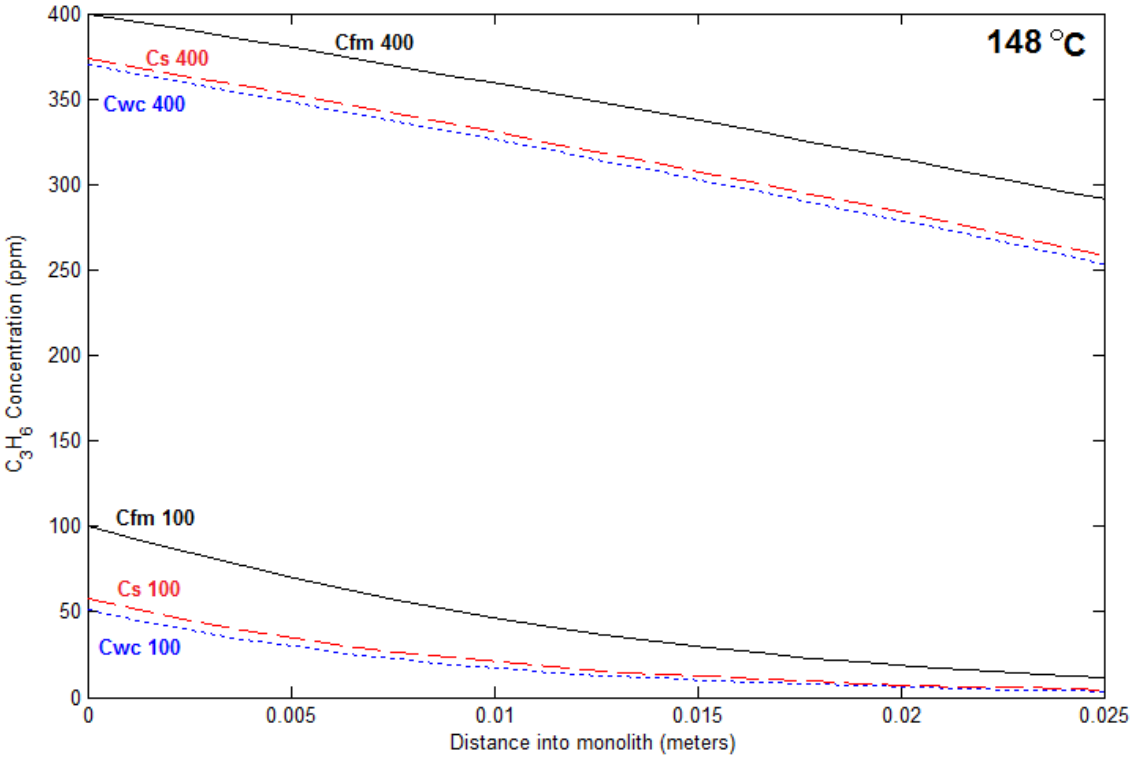

Figure 3.22 Model values for Cfm, Cs, and Cwc at 148 °C

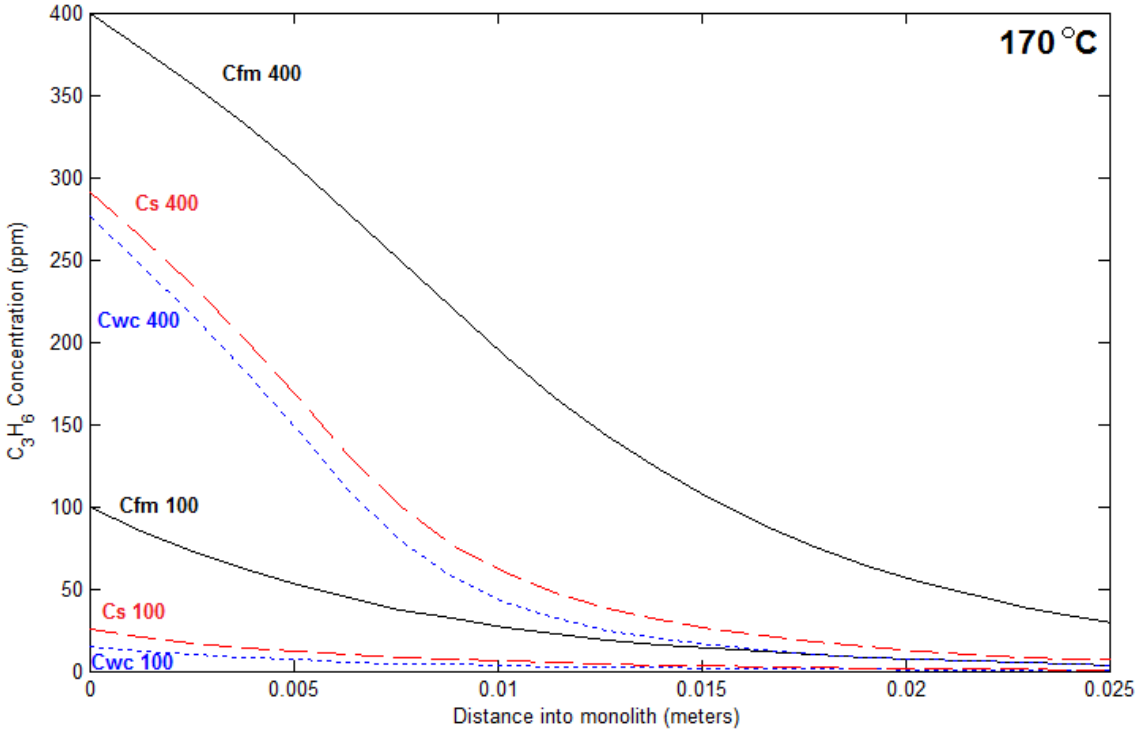

Figure 3.23 Model values for Cfm, Cs, and Cwc at 170 °C

3.7. Conclusions

The construction of a spatially resolved capillary-inlet sampling system for in-channel concentration measurements was successfully completed. A study of propylene oxidation was conducted, which included both light-off measurements by temperature ramp as well as steady-state measurements to acquire kinetic parameters. Using the current Pt/Pd catalyst, the reaction was found to be self-inhibited with respect to propene concentration with a negative reaction order (~ -0.5). The newly built sampling technique was then utilized to measure the propene concentration through the length of the catalyst at various temperatures and propene feed concentrations. Interestingly, the negative-order reaction behavior was observed within the monolith channel. Finally, the low-dimensional model was adapted in order to simulate the propylene effluent conversions and then modified without any further parameter fitting to produce the propene concentration profiles through the catalyst. The comparison between the model results and the experimentally obtained data fits relatively well and provides further evidence of the merits of the LD model.

4. Oxidation of Complex Feed Mixtures over Proprietary and Model Catalysts

4.1 Introduction to Testing Project

A major goal (if not the primary goal) of conducting tightly controlled laboratory experiments is to lead toward real world improvements in the catalytic treatment of exhaust emissions. Many studies (including the other chapters of this dissertation) focus on one or two key reactive components. Those experiments provide crucial data and yield many insights, but it cannot be denied that the real world applications are generally more complex in terms of the feed composition. When additional species are present in the feed stream mixture they often lead to complex behaviors and ambiguous or unexpected results. The additional complexity can be caused by reactants competing for active catalyst sites, competition for limiting reactants, by additional reaction pathways with different intermediate species, as well as by thermal effects from exotherms or endothermic reactions. As a result there exists a need to utilize more complex reactant mixtures during the development process for commercial catalysts so that the real world application can be more closely imitated.

The Texas Diesel Testing & Research Center (now TxCEF) was contracted by a third party to perform bench-scale catalyst testing. The third party participant is an engineering firm that provides its customers with single source solutions for emissions control, including OEM engineering, fabrication, implementation, testing, and training. The company has strong ties to the natural gas industry and has years of hands-on field experience addressing compliance with air quality regulations. Their products include engine controls (air/fuel ratio) and exhaust aftertreatment (catalyst housings and elements), as well as the associated accessories.

The third party provided washcoated monolithic catalyst samples with proprietary catalyst formulations on metallic substrates to TxCEF for testing. The initial round of testing utilized a non-selective catalytic reduction (NSCR) catalyst, which is typically used in emissions treatment of exhaust near the stoichiometric point. Successful completion of the third party NSCR catalyst testing led to the commissioning of additional testing of a new proprietary oxidation catalyst, which was intended for treatment of exhaust with an excess of oxygen. In addition to the testing of proprietary third party participant catalysts, similar experiments were conducted using model catalysts of known composition. This enabled more fundamental aspects to be investigated and related mechanistic and catalytic kinetics to be explored.

The reactant feed streams for the study were relatively complex, containing N_2, O_2, CO_2, H_2O, NO, NO_2 and a mixture of hydrocarbons, comprised of methane, ethane, ethylene, propane, propylene, and formaldehyde. A unique feature of the study, beyond the complexity of the reactant feed streams, is the use of a metal substrate for the third party catalysts, as opposed to the ceramic substrate used for the model catalyst (ceramic substrate was used exclusively in the other chapters of this dissertation). Metal substrates have several advantages, including increased thermal conductivity, thinner walls (for higher cell density, smaller volume, or less pressure drop) and greater mechanical resistance (will not crack like ceramic) [109–111]. Figure 4.1 displays one of the catalyst samples provided by the third party participant, with the thin metallic foil channel walls clearly displaying a more open, corrugated structure compared to ceramic monolith samples.

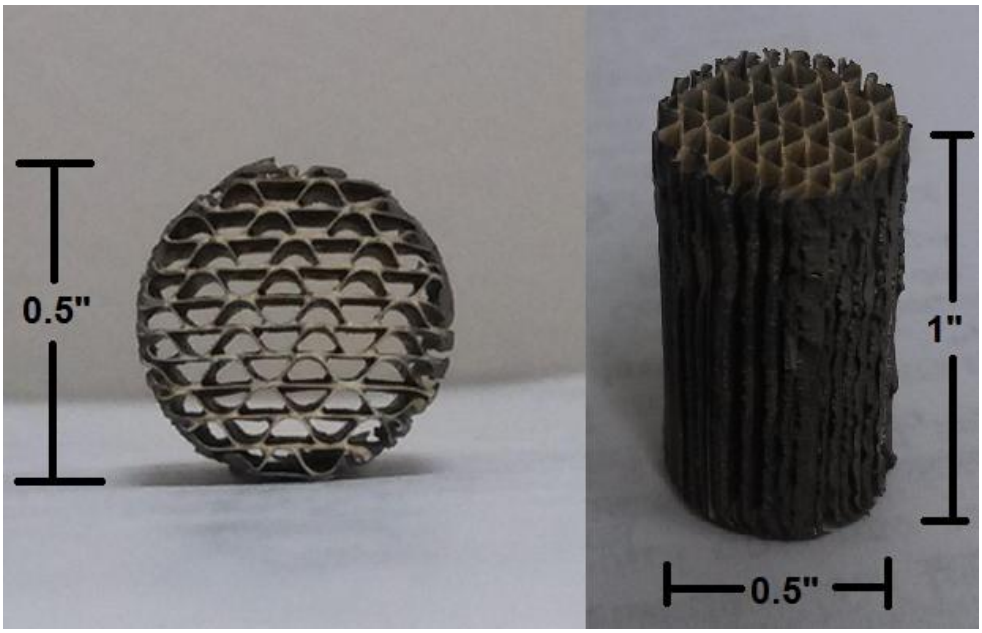

Figure 4.1 Profiles of third party participant metal substrate catalyst

The primary disadvantage of metallic substrates has traditionally been reduced adhesion of the washcoated catalyst, which can lead to higher attrition and premature failure of the catalyst, shortening its useful lifetime. Work continues on increasing the adhesion, including research on pretreatments of the metal foil surface prior to catalyst washcoating [112]. Interest in recycling catalytic converters for the precious metals at the end of their lifecycle also makes metallic substrates more attractive due to the easier separation of the metallic substrate from the more valuable washcoat, as compared to ceramic substrates [113].

The primary objective of the study was to supply the client with catalyst performance data (reactant conversions and product distribution) under the conditions representative of the application. As stated above, additional experiments were then carried out with model catalysts in order to develop a more fundamental understanding of the results. This extension of the work was initiated by applying the third party feed

conditions to a catalyst of known composition and then those additional results were evaluated in order to develop further scientific investigation.

4.2 Third Party Experimental Conditions

The feed gas compositions were specified by the third party and were based on the company's measurements taken in the field for their field applications. To this end the balance gas was to be N_2, rather than argon, due to the client's concerns that NOx might be formed from N_2 across their catalyst. [Comment: The client felt strongly that it was a real phenomenon and needed to be examined, stating that they had seen some evidence of the chemistry.] Using the existing Ar cylinder blends and MFC calibrations would have eliminated the possibility of observing NOx generation from the balance gas.

The third party feed gas compositions are shown in Table 4.1 for both NSCR testing (first column) and oxidation testing (second column). The NSCR testing plan called for first optimizing the concentration of oxygen fed to the catalyst to achieve, according to the testing request, "nearly equal NOx and CO reduction, and maximum VOC (non-methane, non-ethane hydrocarbon) and formaldehyde reduction." (Note: "reduction" is synonymous with conversion.) The steady-state conversions of the reactants were to be determined for several gas hourly space velocity (GHSV) levels in the range of 30,000 h^{-1} to 120,000 h^{-1} and temperatures spanning 400°F to 1200°F (204 to 649 °C). For this study, steady-state was defined in the testing plan as "no measureable directional change in reaction products for a period of 10 minutes." The same bench flow reactor system described in Chapter 1 was utilized for this study.

Table 4.1 Third party feed gas compositions for NSCR and Oxidation tests

	NSCR	Oxidation
Feed Gas	**Concentration**	**Concentration**
Nitrogen	balance (~71%)	balance (~75%)
Oxygen	3000-6000 ppm	10%
Carbon Dioxide	9.4%	5%
Water	18.3%	9.8%
Carbon Monoxide	3000 ppm	600 ppm
Nitrogen Oxide	3000 ppm	40 ppm
Nitrogen Dioxide	0	30 ppm
Methane	800 ppm	800 ppm
Ethane	90 ppm	90 ppm
Propane	70 ppm	70 ppm
Ethylene	90 ppm	90 ppm
Propylene	20 ppm	20 ppm
Formaldehyde	40 ppm	40 ppm

The NSCR inlet gas concentrations, which approximated that of a stoichiometric engine exhaust, contained a rather low concentration of O_2. This concentration was to be estimated experimentally (see NSCR Results section). In practice, the company's NSCR emissions treatment devices were tuned in the field for best performance when installed without direct measurement of the actual O_2 exhaust concentration. The request for a relatively high feed gas concentration of 18.3% H_2O is notable. In addition, CH_4 comprised the main HC species with a concentration of 800 ppm (56% of the hydrocarbon on a C1 basis).

The high H_2O and CH_4 values are consistent with the potential application being treatment of emissions from a natural gas powered engine or even a natural gas flare. More specifically, natural gas (NG) is primarily composed of CH_4 [114] and for this reason the combustion of NG produces more H_2O and less CO_2 per unit of energy than other fuels; this explains the high water content. It also explains the high fraction of CH_4 in the designated feed stream, since an engine or flare fed with primarily CH_4 is likely to

enable a larger portion of CH_4 to survive the combustion and slip into the exhaust than a diesel or gasoline engine would.

The relatively high methane slip in the exhaust of a NG powered vehicle is a result of the increased auto-ignition temperature of CH_4 compared to gasoline and diesel as well as less stringent emissions regulations for CH_4. Additionally, small variations in natural gas composition have influence on NG engine efficiency and emissions [114–118]. Strict rules for methane slip are anticipated [119], motivating research and development toward continued improvement in the efficient combustion of natural gas and the catalytic aftertreatment of methane slip emissions.

The second phase of the third party catalyst testing utilized a proprietary oxidation catalyst, slightly expanded the temperature window down to 300°F (149 °C), and increased the GHSV range to between 60,000 h^{-1} and 180,000 h^{-1}. The feed gas composition for oxidation testing was similar to the NSCR testing, but contained a much higher O_2 feed concentration (10%), which approximates that of a lean-burn engine exhaust. When excess air is used for combustion it also lowers the amount of CO_2 and H_2O in the exhaust by dilution. For oxidation catalyst testing the CO_2 feed was 5% and H_2O was at 9.8%. The CO concentration was also lower (from 3000 ppm to 600 ppm), which is typical of lean-burn combustion exhaust. An additional species, NO_2, was added to the reactant feed stream, but at a rather low level of 30 ppm. The NO feed would also be low at a concentration of 40 ppm for the oxidation catalyst testing (rather than 3000 ppm) and total NOx feed was therefore lowered from 3000 ppm for NSCR testing to 70 ppm for the oxidation testing.

The company agreed to our recommendation of a feed mixture comprising five hydrocarbons (methane, ethane, ethylene, propane, propylene) from a single cylinder blend. This strategy eliminated some flexibility by not allowing the ratio of the hydrocarbons to be altered without ordering new gas cylinder blends, but reduced the system complexity and decreased the total number of mass flow controllers required. The original oxidation catalyst testing request sought a slightly different HC ratio (1400 ppm methane, 100 ppm ethane, 40 ppm ethylene, 70 ppm propane, 10 ppm propylene) but it was decided that the HC blend used for the NSCR testing would be suitable for the oxidation testing.

Determining a reliable method of introducing formaldehyde into the feed stream posed a challenge. Several options were investigated, including gas cylinder blends and even vaporization of solid paraformaldehyde. However, due to the low vapor pressure of formaldehyde, it is only available in gaseous cylinder form in concentrations of 100 ppm or less and at total pressure of less than 1000 psi (with a price over $1000/cylinder). Vaporizing solid paraformaldehyde would have introduced several complicating issues. It was decided that the best approach would be to introduce the formaldehyde with the feed water through the vaporizer. Since formaldehyde is available as a 37 wt. % solution in water, it proved relatively straightforward to mix the appropriate concentration into the vaporizer feed water.

The testing plan did not outline a catalyst pretreatment procedure. A straightforward temperature ramp in excess O_2 (i.e., 10%) to 500 °C over the course of 1 hour and then holding for 1 hour was proposed and agreed upon. At a minimum, this

ensured the catalyst and ceramic paper used in placement of the catalyst in the reactor would have carbon containing contaminants and binders removed by oxidation.

4.3 NSCR Results

The NSCR catalyst testing experiments followed our standard procedure for generating steady-state data. The testing results included variation of the feed gas temperature, GHSV, and O_2 feed concentration. The inlet and outlet concentrations (and percent reduction) of the following components were reported: CO, NO, NO_2, CH_4, ethane, ethylene, propane, propylene, and formaldehyde. The key results are presented here generally in graphical format for ease of interpretation and identification of the main findings and overall trends.

The objective of the NSCR study from an application standpoint was to determine the "optimum" air/fuel ratio (i.e. O_2 feed concentration), and then to measure the product stream concentrations for the provided catalyst at specific GHSV and temperature conditions. The testing plan defined the "optimum" as the O_2 feed concentration used to achieve "nearly equal NOx and CO reduction, and maximum VOC (non-methane, non-ethane hydrocarbon) and formaldehyde reduction." Additional, more fundamental objectives included explaining the observed catalyst behaviors as well as further investigating any unexpected results.

Preliminary NSCR experiments aimed to determine the "optimum" O_2 feed concentration. The resulting "optimum" O_2 feed concentration was intended to be used for all subsequent NSCR tests covering a wide range of GHSVs and temperatures. The conditions for determining the "optimum" value were (with input from the client) GHSV = 100,000 h^{-1}, feed gas temperature of 1000°F (538 °C), with O_2 feed concentration

between 3000 ppm and 6000 ppm in 500 ppm intervals. The initial steady-state conversion results are displayed in Fig. 4.2. High conversions of CO, ethylene, propylene and formaldehyde were attained for all O_2 feed concentrations, but near zero conversion of NO or total NOx was measured.

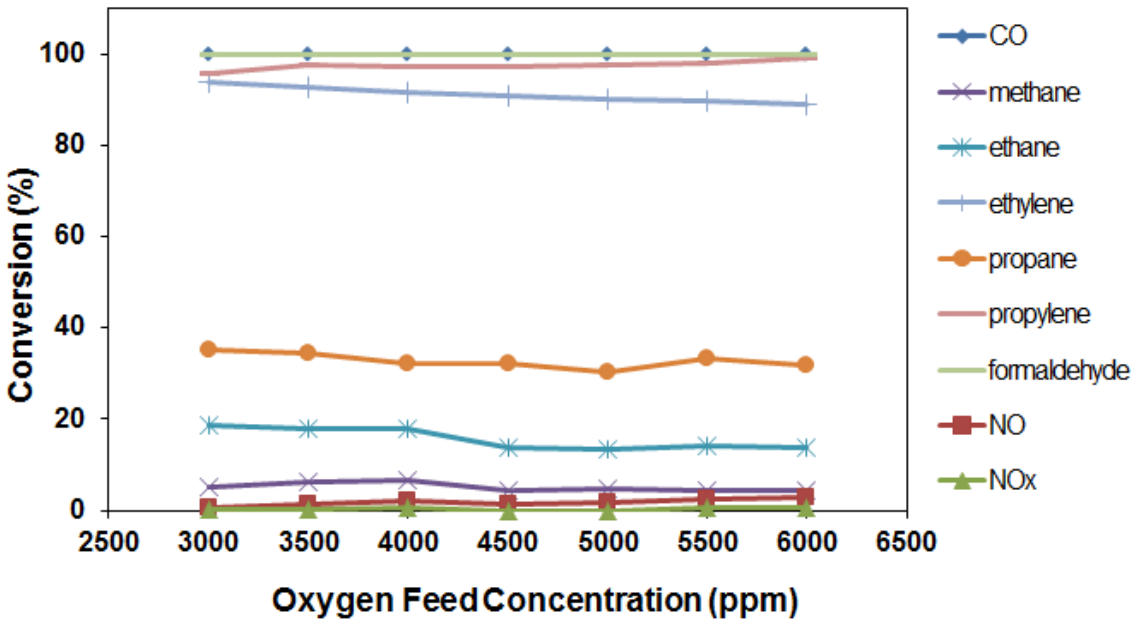

Figure 4.2 Initial results for determining "optimum" O_2 feed quantity (T_f = 538 °C, GHSV = 100,000 h^{-1})

The lack of NOx reduction indicated the exhaust composition was too lean. This led to excessive consumption of the HC species which would otherwise serve as the reducing agent of NOx. When an excess of O_2 is present in the feed, this typically requires a selective catalytic reduction (SCR) catalyst to achieve a NOx conversion. Given that the catalyst being tested is a NSCR catalyst, it is expected that the CO and HC species will react with O_2, and that NOx will not be reduced to N_2 by the CO and HC until after the excess O_2 is consumed.

In an attempt to increase the overall conversion of reacting species, a lower concentration of 1000 ppm O_2 was fed, with conversion results shown in Fig. 4.3.

Increases in methane, ethane and propane conversion were achieved and complete conversion of NOx was attained. Additionally, there was no decrease in CO, propylene, ethylene or formaldehyde conversion at the lower O_2 feed. Clearly, reducing the O_2 feed concentration to 1000 ppm resulted in improvements in the overall conversions of the reactants.

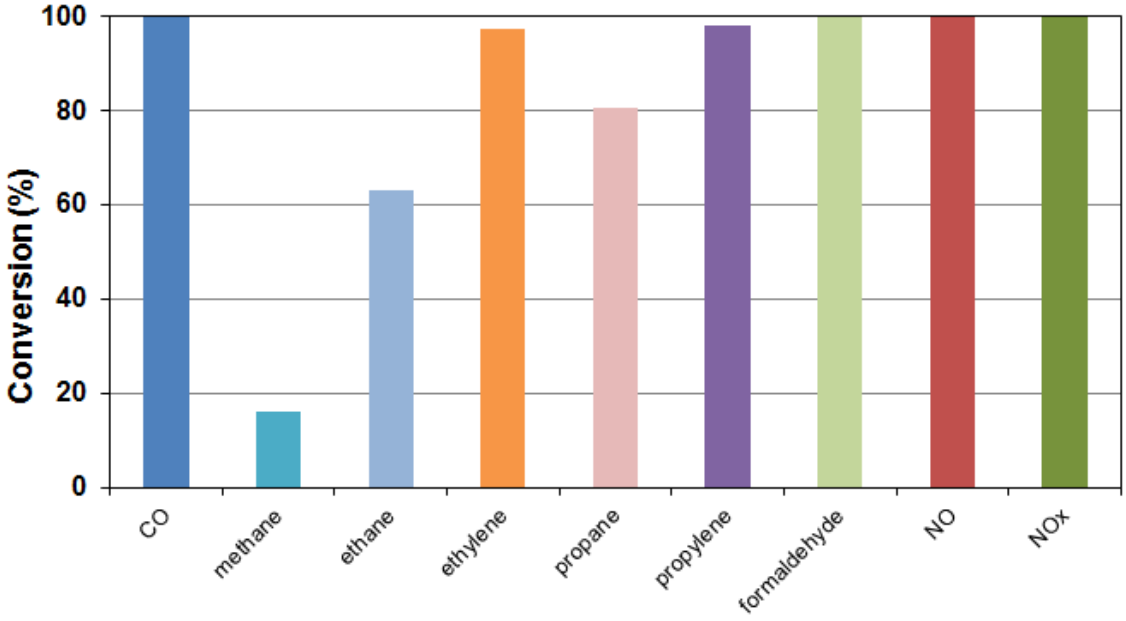

Figure 4.3 Reactant conversions at 1000 ppm O_2 feed (T_f = 538 °C, GHSV=100,000h^{-1})

Additional testing at the 538 °C, GHSV = 100,000 h^{-1} condition was then performed to explore the reactant conversions with O_2 feed concentration varied between 0 and 3000 ppm (Fig. 4.4). A peak in conversions was achieved at 1500 ppm O_2. NOx conversion remained high for O_2 concentrations lower than 1500 ppm. The NOx reacts with the CO and HCs to form N_2, H_2O and CO_2 by the following reactions:

$$CO + NO_2 \rightarrow NO + CO_2,$$

$$CO + NO \rightarrow \tfrac{1}{2} N_2 + CO_2,$$

$$C_mH_n + (2m + \tfrac{1}{2} n)NO_2 \rightarrow (2m + \tfrac{1}{2} n)NO + mCO_2 + \tfrac{1}{2} nH_2O, \text{ and}$$

$$C_mH_n + (2m + \tfrac{1}{2} n)NO \rightarrow (m + 1/4\ n)N_2 + mCO_2 + \tfrac{1}{2} nH_2O.$$

Conversion of the HCs drops at O_2 feed levels below 1500 ppm, when not enough oxidant (O_2+NOx) is present and the overall system is oxidant limited. The steep drop in conversion of several HC species as the O_2 feed level was increased above 2000 ppm was not expected, and will be further explored in Section 4.8.

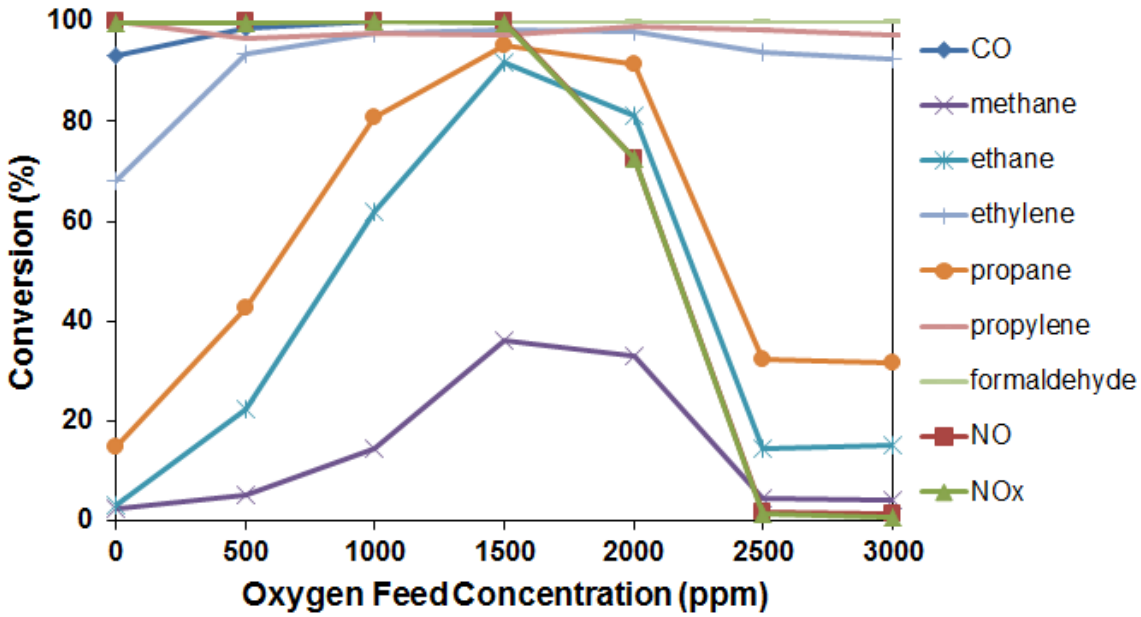

Figure 4.4 Peak in conversions at lower O_2 Feeds (T_f = 538 °C, GHSV = 100,000 h^{-1})

Temperature and space velocity sweeps were then conducted, starting from the lowest feed gas flow rate, GHSV = 30,000 h^{-1}, with steady-state conversion measurements recorded starting from 204 °C and increasing in increments of 56 °C (100°F) to 649 °C. The testing plan called for using only the 1500 ppm O_2 feed level that produced the best results at the previously performed 538 °C, GHSV = 100,000 h^{-1} condition. The O_2 feed concentration was, however, varied to investigate if the peak would remain at 1500 ppm O_2 at the lower space velocity.

Reactant conversions as a function of O_2 feed concentration are displayed in Fig. 4.5 for temperatures of 371 °C, 427 °C, and 538 °C. As shown in Fig. 4.5, the location of the peak conversion is dependent on temperature, based on the shift from left to right (lower O_2 feed to higher O_2 feed) as the feed temperature increased. At 371 °C, the highest conversion was observed for an anaerobic feed. At this lower temperature, reaction rates for the oxidation reactions are slower, resulting in a lower consumption of the feed O_2. The net reducing conditions that are favorable for NOx reduction are only achieved at very low O_2 feed at this lower temperature.

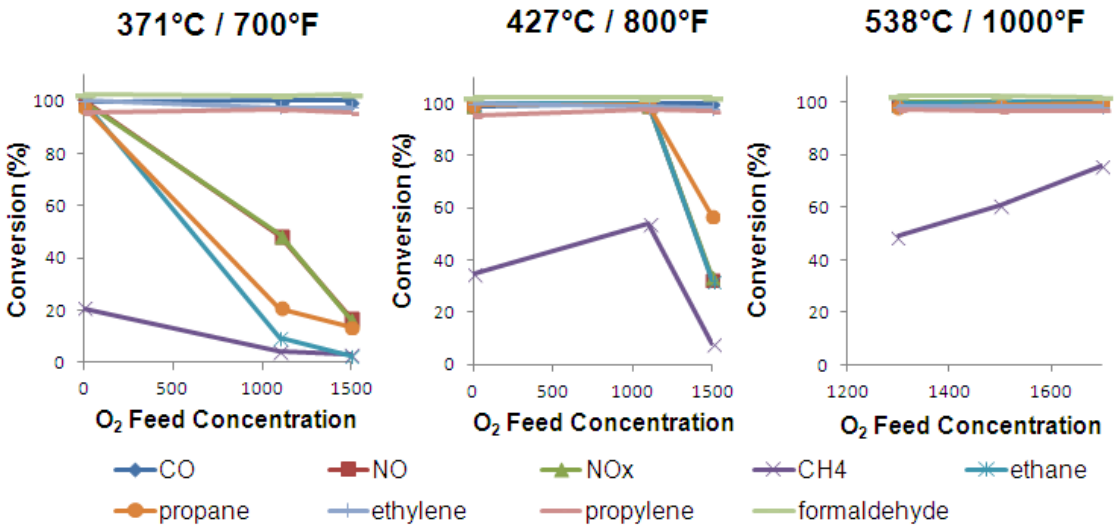

Figure 4.5 Shift in optimum O_2 feed as temperature varies at GHSV = 30,000 h^{-1}

As the temperature increases, the rate of hydrocarbon oxidation increases. This increases the consumption of additional O_2 and results in conditions that promote the conversion of NOx. At 427 °C, there is an apparent overall conversion peak at 1100 ppm O_2 feed, since NOx conversion drops off at higher O_2 feed (1500 ppm) and CH_4 conversion drops off at lower O_2 feed (0 ppm). It should be mentioned that if smaller increments of O_2 feed concentration had been tested at 427 °C, then an increased

conversion of CH_4 may have been possible in the 1000-1500 ppm O_2 range while maintaining the near complete conversion of CO, NOx and the other HCs.

A further increase in temperature to 538 °C results in increased conversion of all the reacting species. The CO, NOx and non-methane HCs conversions are near 100% and CH_4 reaches 76% conversion. Again, the increase in temperature increases the reaction rates, which increases the rate of feed O_2 consumption, and the NOx conversion is sustained at a high level at higher O_2 feed concentrations. The peak overall conversion was not identified at 538 °C, however, as O_2 levels above 1700 ppm were not tested. Based on the trends at 371 °C and 427 °C, it is difficult to predict the results of an increase in O_2 feed above 1700 ppm at 538 °C and GHSV = 30,000 h^{-1}. The additional O_2 might enable a further increase in the CH_4 conversion while maintaining near complete conversion of the other species. Another possibility is the additional O_2 might result in a drop in conversions, similar to the drop measured at lower temperatures, and thus identify the peak in overall conversion.

Testing proceeded from this point by attempting to efficiently identify the approximate "optimum" O_2 feed concentration at each temperature. This still led to long testing periods, with experiment time reaching up to 15 hours per day. If more time had been devoted to locating the exact "optimum" O_2 feed concentration that yielded the highest overall conversion, perhaps additional system behaviors could have been identified (or ruled out), such as the clockwise conversion hysteresis that will be examined in Chapter 5.

Several results for GHSV= 60,000 h^{-1} are displayed in Fig. 4.6, which is twice the space velocity examined in Fig. 4.5. Space velocity was increased by increasing the total

gas feed flow rate, resulting in reduced contact time. If the reaction is kinetically limited at these conditions, conversion will decrease with increasing GHSV. Comparing Fig. 4.5 to Fig. 4.6, this trend is easily seen in the peak CH_4 conversion at 427 °C, falling from 54% at GHSV= 30,000 h^{-1} to 34% at GHSV=60,000 h^{-1}. To further emphasize this point, the peak CH_4 conversion was only 13% at 427 °C for the highest space velocity tested (GHSV= 120,000 h^{-1} for the NSCR catalyst, data not shown), again at a feed concentration of 1000 ppm O_2.

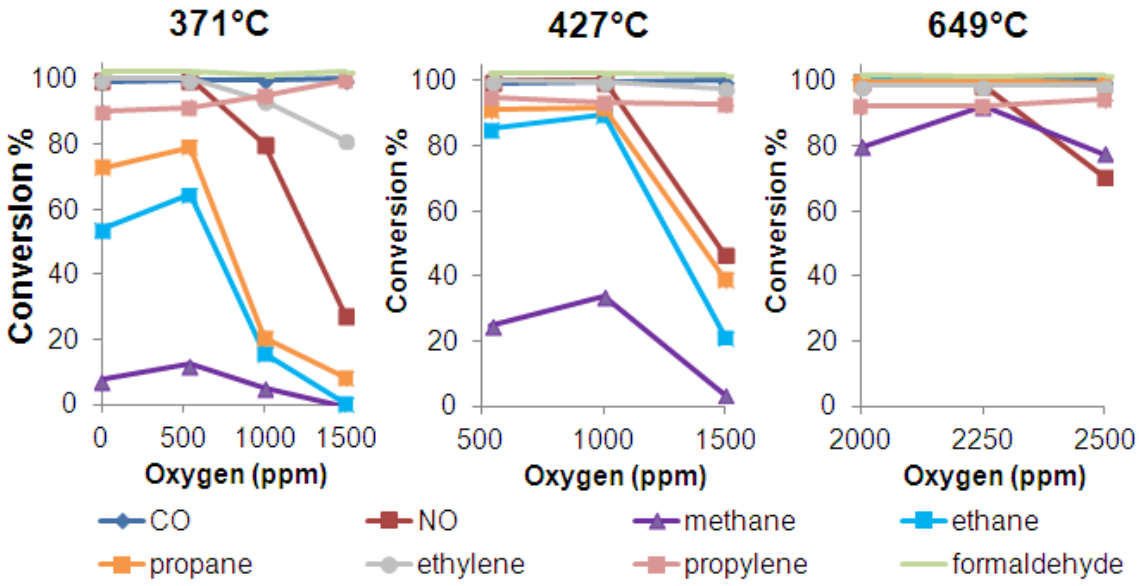

Figure 4.6 NSCR results for several temperatures at GHSV = 60,000 h^{-1}

4.4 Discussion of third party NSCR Catalyst Results

The NSCR catalyst testing results were reported to the third party participant on a daily basis to receive feedback and continually refine the path forward. At the completion of the testing several anticipated main conclusions were confirmed. These included the increase in overall conversions as temperature increased, the decrease in overall conversions as GHSV increased, as well as there being no evidence for NOx formation across the catalyst. A few of the study findings were not anticipated. These include the

lower "optimum" O_2 feed concentration during the preliminary experiments, the shift to higher O_2 feed concentrations required to achieve the highest overall conversions as temperatures increased, and the steep decline in conversion of some HC species at higher O_2 feed concentrations.

The preliminary NSCR experiments, which sought the "optimum" O_2 feed concentration at conditions of T_f = 538 °C and GHSV = 100,000 h^{-1}, determined that the O_2 feed concentration should be decreased below the lower bound of the testing plan estimate (originally 3000 to 6000 ppm O_2). The reduced O_2 feed concentrations (0 to 2500 ppm O_2) resulted in multiple operating points with significant increases in the conversions of NO, CO and HCs (Fig. 4.4), with a peak in conversions identified at 1500 ppm O_2. To further analyze the results, an "overall" conversion can be calculated by using the sum of the effluent concentrations of the reactive species (CO, NOx, HCs) and the sum of their inlet reactants concentrations (7110 ppm):

$$overall\,conversion = \frac{(7110 - \sum C_{\text{reactants}})}{(7110)}. \tag{4-1}$$

A stoichiometric number S_N can be used to characterize the oxidant/reductant ratio:

$$S_N = \frac{(2C_{O_2} + C_{NO} + 2C_{NO_2})}{\left(C_{CO} + 4C_{CH_4} + 7C_{C_2H_6} + 6C_{C_2H_4} + 10C_{C_3H_8} + 9C_{C_3H_6} + 2C_{CH_2O}\right)}, \tag{4-2}$$

where C_i is the gas feed concentration of species i. Thus the gas mixture is lean if $S_N > 1$, stoichiometric if $S_N = 1$, and rich if $S_N < 1$. Further, a modified stoichiometric number, $S_{N\text{-mod}}$ is defined, which excludes NOx as an oxidant:

$$S_{N-\text{mod}} = \frac{2C_{O_2}}{\left(C_{CO} + 4C_{CH_4} + 7C_{C_2H_6} + 6C_{C_2H_4} + 10C_{C_3H_8} + 9C_{C_3H_6} + 2C_{CH_2O}\right)}. \tag{4-3}$$

This expression (eqn. 4-3) indicates that the gas mixture must utilize NOx as an oxidant in order to oxidize all CO and HC reactants when $S_{N\text{-}mod}<1$. These metrics are plotted in Fig. 4.7.

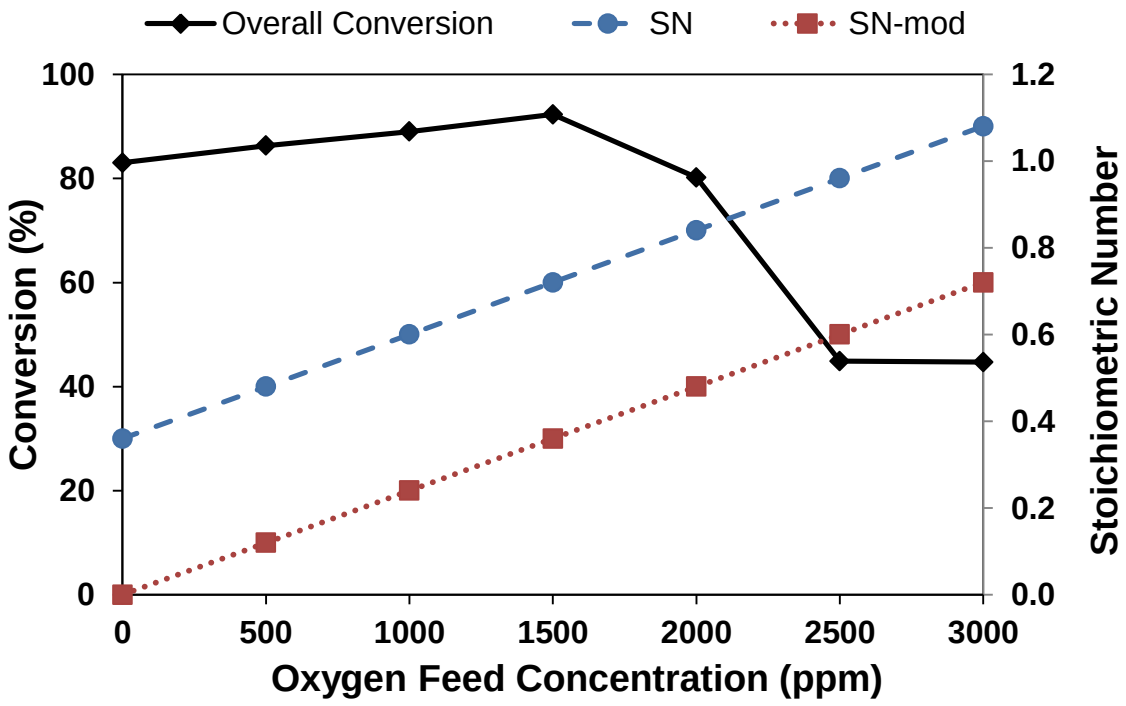

Figure 4.7 Overall conversion and stoichiometric number at lower O_2 Feeds (T_f = 538 °C, GHSV = 100,000 h^{-1})

The overall conversion (diamonds in Fig. 4.7) peaks at 92% conversion with a 1500 ppm O_2 feed concentration, which is in agreement with the determination that was made through observation of the individual reactant conversions in Fig. 4.4. As mentioned earlier, the lack of NOx conversion for O_2 feed concentrations in the range of 3000 to 6000 ppm (Fig. 4.2) indicates the exhaust environment is too lean. As now shown in Fig. 4.7 the overall conversion was only 45% for an O_2 feed of 3000 ppm. Interestingly, at an O_2 feed of 2500 ppm the overall conversion does not increase despite a stoichiometric number of 0.96 (S_N < 1), indicating an overall rich feed mixture. In fact, the modified stoichiometric number ($S_{N\text{-}mod}$) is already less than 1 at a 3000 ppm O_2 feed,

indicating NOx must be utilized as an oxidant to convert all of the CO and HCs. The data show the CO conversion was 100% at this condition (Fig. 4.2) and, in addition, the conversions were very high for formaldehyde, propylene and ethylene. On the other hand, the propane, ethane, and methane conversions were less than 50%. The lower reactivity of those HC species resulted in lower extents of reaction at these conditions and lower O_2 consumption. With less O_2 consumed a net-reducing environment is not achieved and no HC selectively reacts with NOx rather than O_2. In short, the catalyst has the capability to perform NOx reduction, however it does not selectively react NOx with CO or HC when O_2 is present, thus the designation as a NSCR catalyst is accurate.

Another study finding that was not anticipated is the increase in the O_2 feed concentration needed to achieve the highest overall conversions as temperature was increased. This shift in the peak conversion is attributed to the faster HC oxidation kinetics, which increase the HC conversions and lead to increased O_2 consumption, thus creating the reducing environment for NOx conversion. At higher temperature the O_2 feed that resulted in a peak overall conversion at lower temperature now resulted in O_2 being the limiting reactant. Thus, higher O_2 feed concentration leads to higher overall conversions, as long as the increased O_2 feed does not lead to an oxidative condition in which NOx reduction is not achieved.

The final unanticipated result was the steep decline in conversion for some HC species as O_2 feed was increased, specifically the alkanes. This decline in methane, ethane, and propane conversions had the impact of more sharply defining the “optimum” O_2 feed concentration and peak overall conversion. The conventional expected behavior is for the HC conversion to increase as O_2 feed concentration is increased, meaning

positive order reaction kinetics with respect to O_2. This interesting phenomenon is investigated in Section 4.8 as well as in Chapter 5.

4.5 Oxidation Catalyst Results

The testing procedure for the third party oxidation catalyst used a feed concentration of 10% O_2 rather than a varying O_2 feed concentration as was done for the NSCR testing. The feed gas additionally contained 5% CO_2, 9.8% H_2O, 600 ppm CO, 40 ppm NO, 30 ppm NO_2, 800 ppm CH_4, 90 ppm ethane, 90 ppm ethylene, 70 ppm propane, 20 ppm propylene, and 40 ppm formaldehyde, with balance N_2, as shown in Table 4.1. The space velocities tested ranged from 60,000 h^{-1} to 180,000 h^{-1} in increments of 10,000 h^{-1}. At each GHSV the steady-state conversions were determined for the temperature range 300°F to 1100°F for increments of 100°F. (This corresponded to 149 °C, 204 °C, 260 °C, 316 °C, 371 °C, 427 °C, 482 °C, 538 °C, and 593 °C.) Again, the composition of the catalyst was not made available by the third party.

Reactor effluent concentrations at a GHSV of 60,000 h^{-1} for CO and the HCs (excluding CH_4) are shown in Fig. 4.8a and conversions (including CH_4) are shown in Fig. 4.8b. There was no measureable NOx conversion. At the lowest temperature tested, 149 °C, conversions of 50% for CO and 28% for formaldehyde were obtained, while all other reactants had negligible conversion. At the next higher temperature tested, 204 °C, the CO achieved full conversion and light-off was also attained (>50% conversion) for ethylene, propylene, and formaldehyde. Further increases in temperature were required to initiate the oxidation of propane, ethane and methane. Propane surpassed 50% conversion at 427 °C and ethane achieved light-off at 482 °C, while methane did not achieve light-

off until 538 °C. The relative order of HC reactivities, as shown in Fig. 4.8, are well documented in the literature (e.g.,Yu Yao et al.[120]).

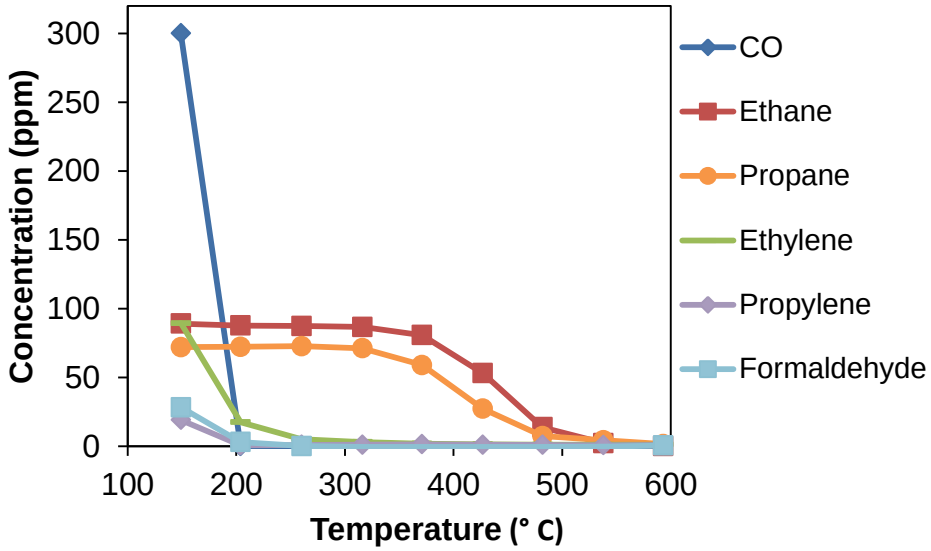

Figure 4.8a Outlet CO and HC concentrations at GHSV = 60,000 h^{-1}

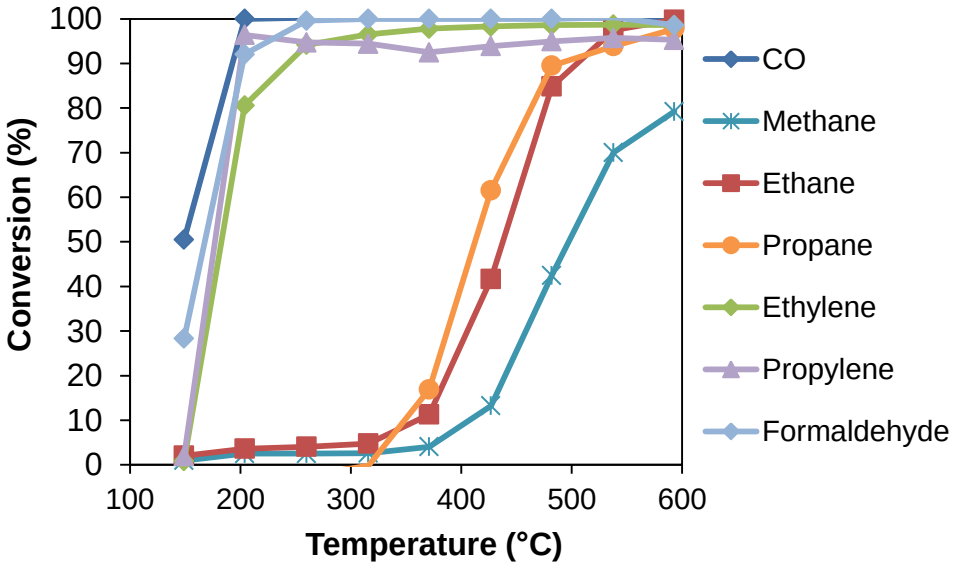

Figure 4.8b Outlet Conversions for CO and HCs at GHSV = 60,000 h^{-1}

As the space velocity was increased in increments of 10,000 h^{-1}, reactant conversions subsequently decreased incrementally. There was no measureable NOx conversion at any space velocity. Reactor effluent concentrations for CO and the HCs (excluding CH_4) at GHSV = 180,000 $h^{-1}$are shown in Fig. 4.9a, while the conversions

(including CH_4) are shown in Fig. 4.9b. This was the highest space velocity tested with a total gas flow rate of 9.7 SLPM. The propane, ethane and methane did not achieve light-off even at the highest temperature tested (593 °C). The more reactive components (CO, formaldehyde, ethylene, propylene) also have their light-offs shifted to higher temperatures, exceeding 50% conversion only at temperatures of 260 °C and above. The shift to higher temperatures required to achieve light-off (>50% conversion) at higher space velocity is attributed to the decreased contact time for reactant species to oxidize on the catalyst surfaces.

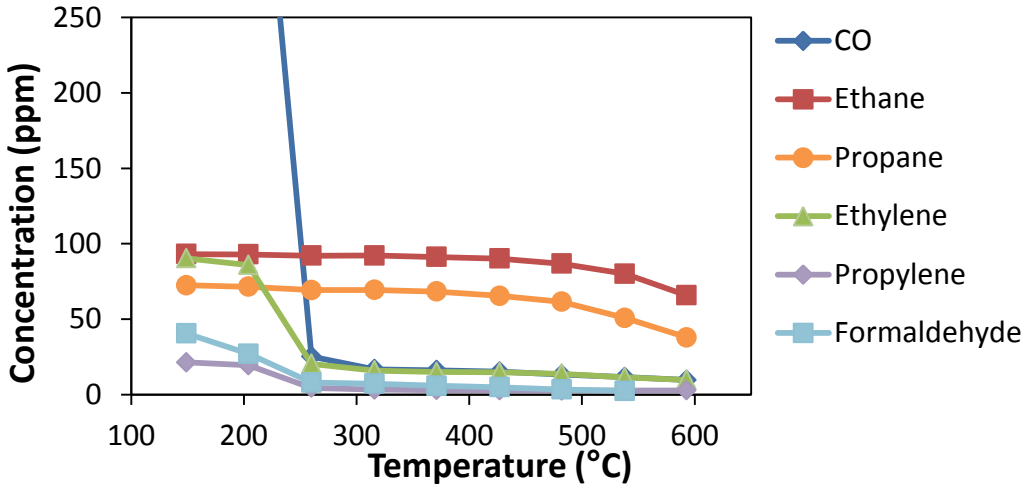

Figure 4.9a Outlet CO and HC concentrations at GHSV = 180,000 h^{-1}

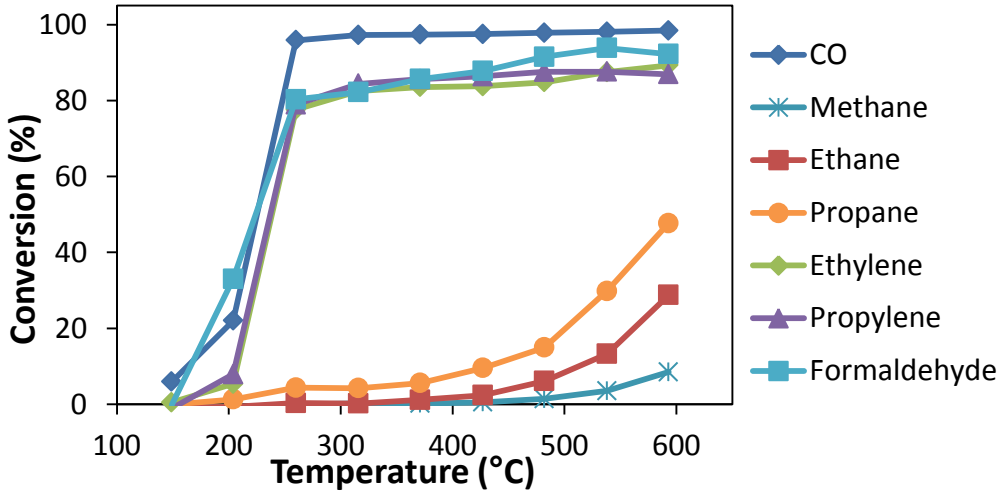

Figure 4.9b Outlet Conversions for CO and HCs at GHSV = 180,000 h^{-1}

To further illustrate the effect of space velocity on conversion, the light-off curves for methane at each space velocity tested are displayed in Fig. 4.10. The figure axis starts from a relatively high temperature of 350 °C and the conversion only goes up to 80% to improve readability of the data since CH_4 is the least reactive HC present. It is clear that a significant drop in CH_4 conversion occurs as space velocity increases from a maximum 79% conversion at 593 °C and GHSV= 60,000 h^{-1} then decreasing to below 10% conversion at GHSV = 180,000 h^{-1}.

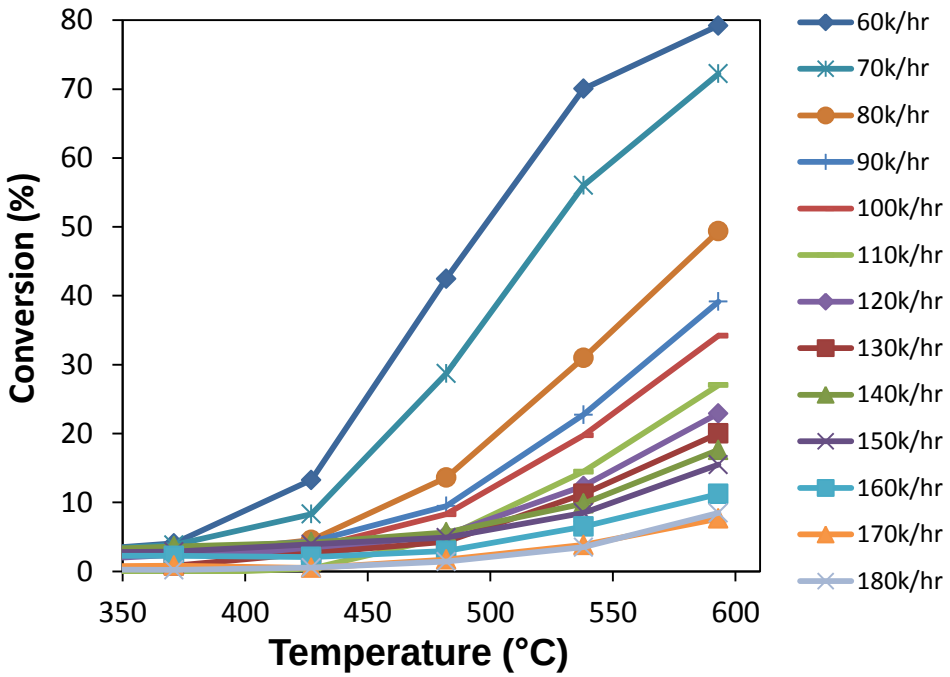

Figure 4.10 Conversion of CH_4 at varying GHSV

4.6 Discussion of Third Party Oxidation Catalyst Results

The 10% O_2 feed used for third party oxidation catalyst testing resulted in lean conditions with no measureable NOx conversion and no associated peak in overall conversion. The result of decreasing conversions as space velocity was increased is a predictable one. Decreasing the contact time leads to reduced extents of reaction for the reactant species. One possibly interesting result is the difficulty of carrying out methane

oxidation compared to the other HCs, which can be highlighted by grouping the total hydrocarbons (THC) together and comparing those with the methane concentration alone, displayed in Fig. 4.11.

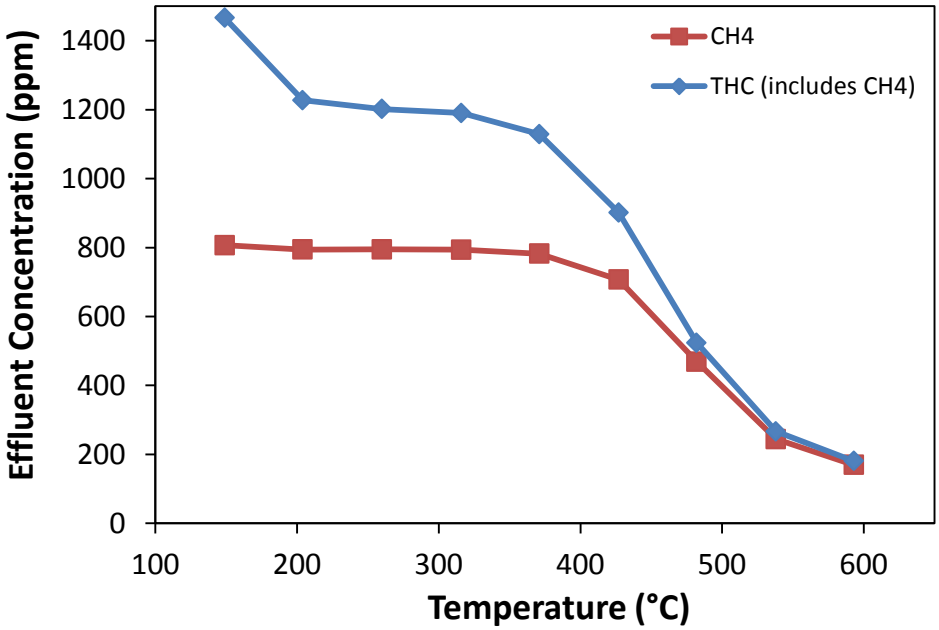

Figure 4.11 Effluent concentrations for THC and CH_4 at GHSV = 60,000 h^{-1}

At 149 °C, the portion of effluent THC concentration made up of CH_4 is already over half, as shown in Fig. 11. The first drop in THC concentration (from 149 °C to 204 °C) results from the oxidation of the most reactive components, the aldehyde and alkenes (confirmed by Fig. 4.8). This is followed by the less reactive alkanes, which start reacting at 316 °C. Propane and ethane are more reactive than methane, and by 538 °C the outlet concentration of THC is almost totally comprised of methane, so the graphed lines essentially overlap. It is interesting to note that the observed order of reactivities for the HCs roughly aligns with the photochemical ozone formation reactivities developed for California emissions regulations [121], which gave the ranking of propylene (9.4 grams

ozone formed per gram VOC emitted) > ethylene (7.4) > formaldehyde (7.2) > propane (0.48) > ethane (0.25) > methane (0.015).

4.7 Third Party Oxidation Reactions on Model Catalyst

After furnishing the acquired data to the company, which utilized their proprietary catalyst formulations, experiments were carried out applying the third party oxidation feed conditions to a catalyst of known composition. For purposes of comparison and to evaluate the potential for more fundamental studies, a catalyst utilized in Chapters 2, 3 and 5 of this dissertation was selected. The BASF catalyst DOC4, also referred to as D-0, was chosen. It is a ceramic substrate monolith containing 60 g/ft^3 PGM (Pt:Pd ratio 2:1 by mass) with no additional zeolite component. Further catalyst details are described in Chapter 2. The total flow rate was set to GHSV= 60,000 h^{-1} with results displayed in Fig. 4.12.

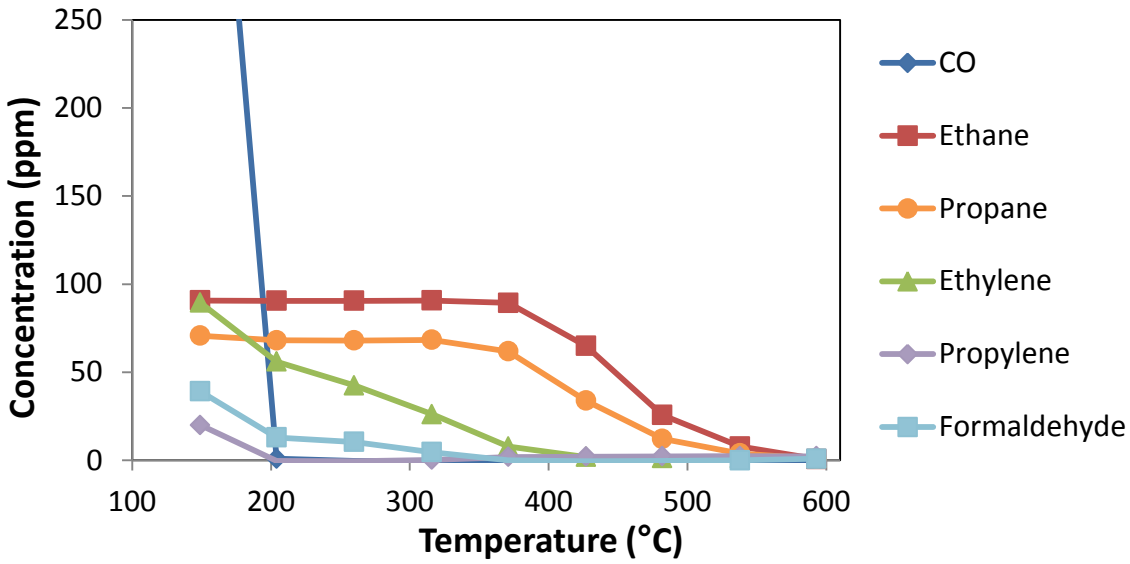

Figure 4.12 Outlet Concentrations for DOC4 Catalyst at GHSV= 60,000 h^{-1}

Upon initial inspection of the results (Fig. 4.12), the DOC4 catalyst displays little differentiation from the third party oxidation catalyst (Fig.4.8a). Comparing the data numerically reveals a slight edge in conversions to the third party catalyst over the DOC4

catalyst. At the 149 °C testing point, the DOC4 catalyst allows 506 ppm CO to break through (16% conversion), while the third party catalyst only allowed 300 ppm through (50% conversion). There are also small increases in HC conversion with the third party catalyst compared to the DOC4 catalyst. Figure 4.13 displays the comparison between the two catalysts for THC and CH_4.

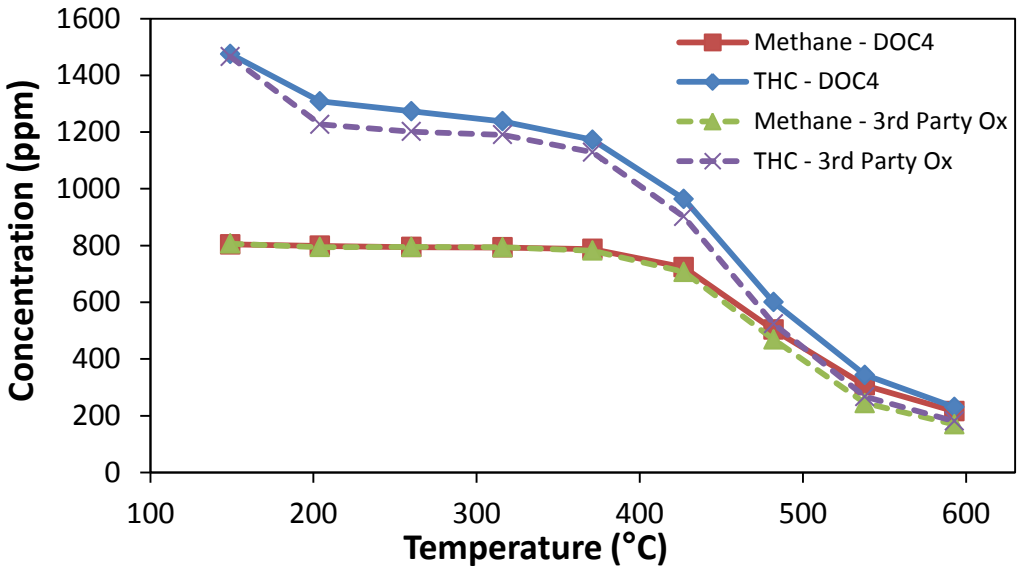

Figure 4.13 Outlet concentrations for THC and CH_4 at GHSV= 60,000 h^{-1}

The third party oxidation catalyst appears to perform slightly better than the BASF DOC4 catalyst under these particular testing parameters. Unfortunately, further speculation on which catalyst parameters contributed to this outcome is not especially meaningful without further details on the third party catalyst formulation, such as PGM loading, dispersion, or use of promoters. Our attention was then turned toward utilizing the DOC4 catalyst for experiments with the third party NSCR conditions.

4.8 Third Party NSCR Conditions on BASF Catalyst

It was presumed that the third party NSCR catalyst formulation might contain materials to enhance performance around the stoichiometric point, such as oxygen storage components, or perhaps rhodium to improve NOx reduction. The BASF DOC4

catalyst was formulated as a model diesel oxidation catalyst (DOC), so its ability to adequately perform 3-way catalyst duties might be questionable. It was considered that an optimum O_2 feed concentration in which both NOx and HC/CO conversions take place might not exist for the DOC4 catalyst. With that in mind, the third party NSCR conditions were nevertheless carried out on the DOC catalyst, with an additional measurement at 10% O_2 for comparison purposes. As it turned out, the actual performance of the DOC4 catalyst was quite good at these specific conditions, displaying high conversions for both oxidation and reduction reactions.

As shown in Fig. 4.14, at the lowest temperature tested (204 °C) there is essentially no reaction activity at low O_2 feed concentrations. However, at the added testing point of 10% O_2, the CO, formaldehyde, and propylene all achieve light-off. It therefore appears that at these feed conditions the oxidation reactions are overall positive order with respect to O_2.

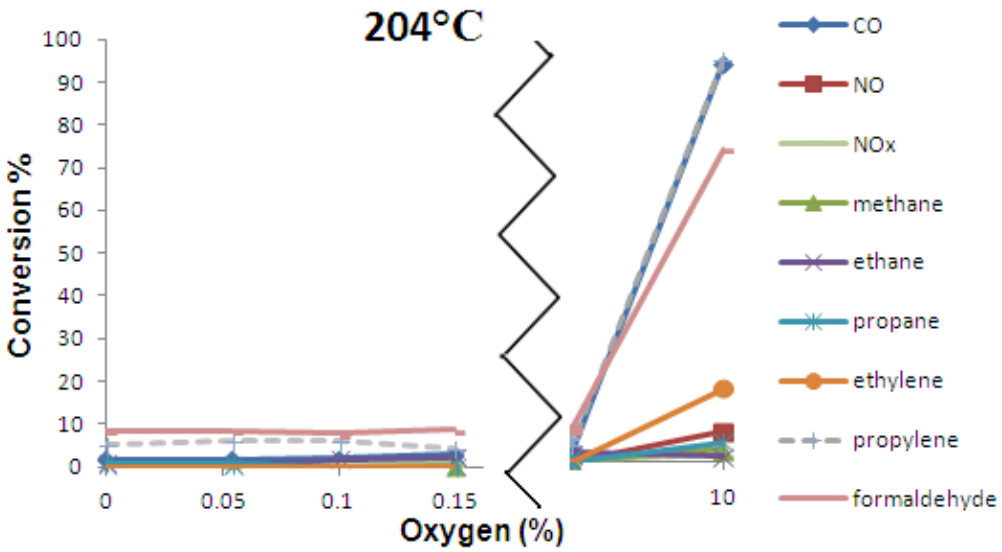

Figure 4.14 NSCR conditions on DOC4 catalyst (204 °C, GHSV=60,000 h^{-1})

The trend of low reaction rates at low O_2 feed concentrations and higher conversions at 10% O_2 also occurs at temperatures of 260 °C (Fig. 4.15) and 316 °C (Fig.

4.16). As noted previously in the oxidation conditions testing (Section 4.5), there is a progression of conversions starting with formaldehyde, then propylene, followed by CO and finally ethylene. Also shown is measureable conversion of NO for the 10% O_2 feed. The NO conversion occurs from the oxidation of NO into NO_2, and the total NOx (NO + NO_2) conversion remains essentially zero.

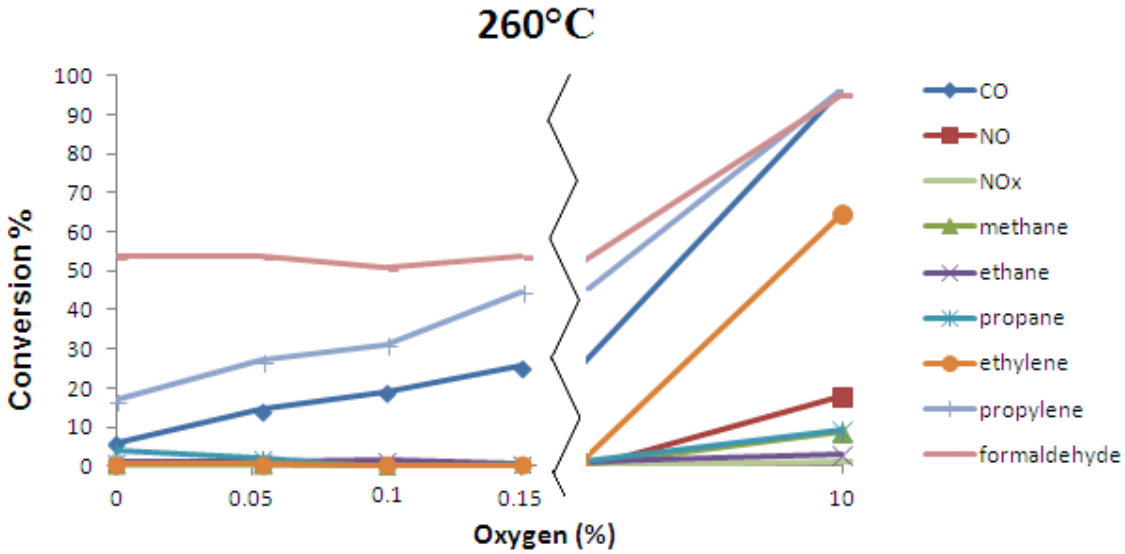

Figure 4.15 NSCR Conditions on DOC4 catalyst (260 °C, GHSV=60,000 h^{-1})

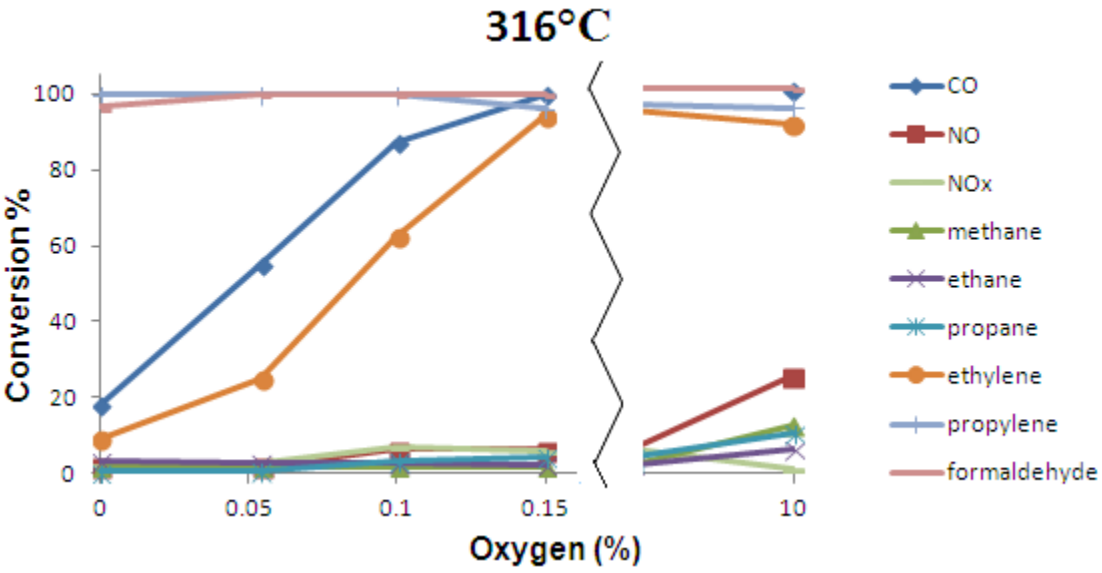

Figure 4.16 NSCR Conditions on DOC4 catalyst (316 °C, GHSV=60,000 h^{-1})

At temperatures of 371 °C and up to as high as 593 °C (Fig. 4.17 – 4.21), peaks in conversions do in fact appear at low O_2 feed concentrations, replicating the trend seen with the third party NSCR catalyst (Fig. 4.6). As temperatures increase, the peaks subsequently shift to higher concentrations of O_2 feed. At 371 °C (Fig. 4.17), the CH_4, C_2H_6 and NOx have conversion peaks at 0.05% O_2, while C_3H_8 peak conversion is at 0.1% O_2. At 427 °C (Fig. 4.18), the CH_4 and NOx peaks are at 0.1% O_2, with the ethane and propane having peaks at 0.15% O_2. (Remark: The true peaks are probably somewhere in-between the testing points and would likely align for a given temperature if the O_2 feed testing points had been more closely spaced.) The "optimum" O_2 feed at 371 °C is therefore within the 0.05%-0.1% O_2 range, while at 427 °C the optimum is within the 0.1%-0.15% O_2 range.

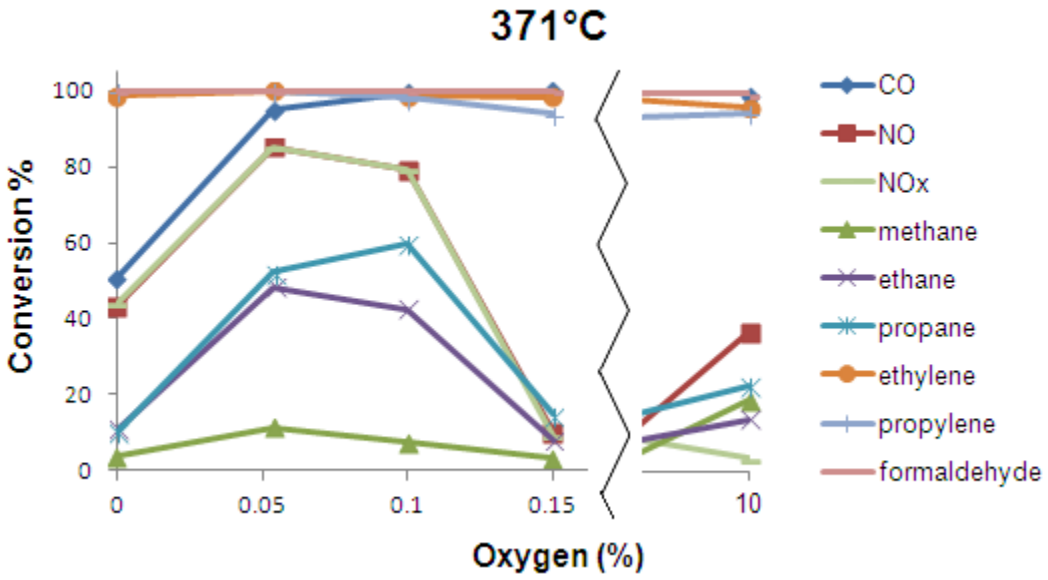

Figure 4.17 NSCR Conditions on DOC4 catalyst (371 °C, GHSV=60,000 h^{-1})

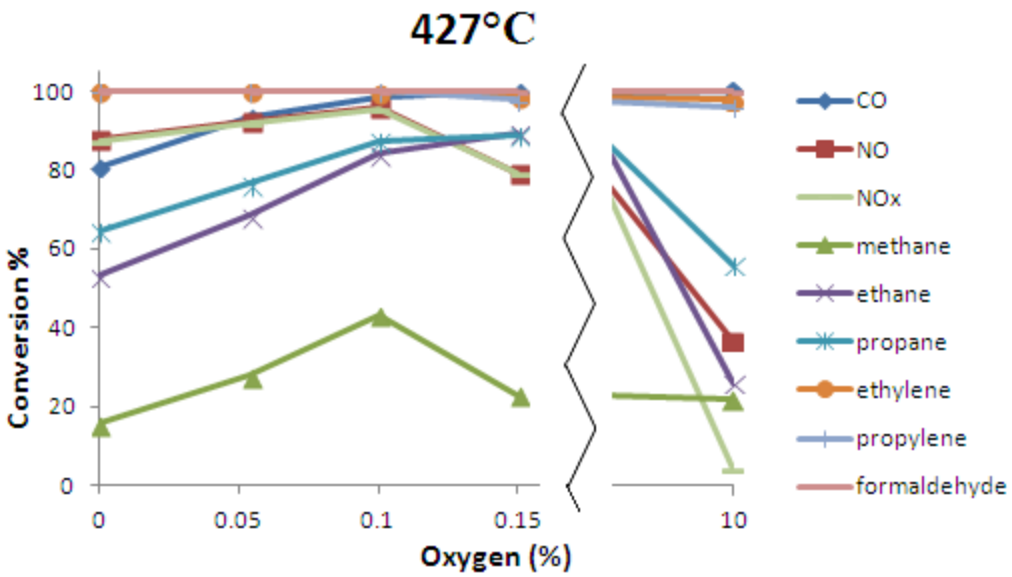

Figure 4.18 NSCR Conditions on DOC4 catalyst (427 °C, GHSV=60,000 h^{-1})

To illustrate, results for the feed temperature of 482 °C are shown in Fig. 4.19. The optimum O_2 feed concentration can be visibly identified by the peak in overall conversion at 0.17% O_2. If the O_2 feed had been increased from 0.15% directly to 0.2% (as had been done at 371 °C and 427 °C) then the peak would have appeared to be at 0.15% O_2, since the conversion of CH_4, ethane, propane, and NOx all drop at 0.2% O_2. By carrying out the intermediate feeds of 0.17% and 0.175% O_2, a better overall conversion was achieved. At both of those intermediate points, improved conversions were realized, with all reactants achieving complete conversion, with the exception of CH_4, which also achieved a relatively high 75% conversion.

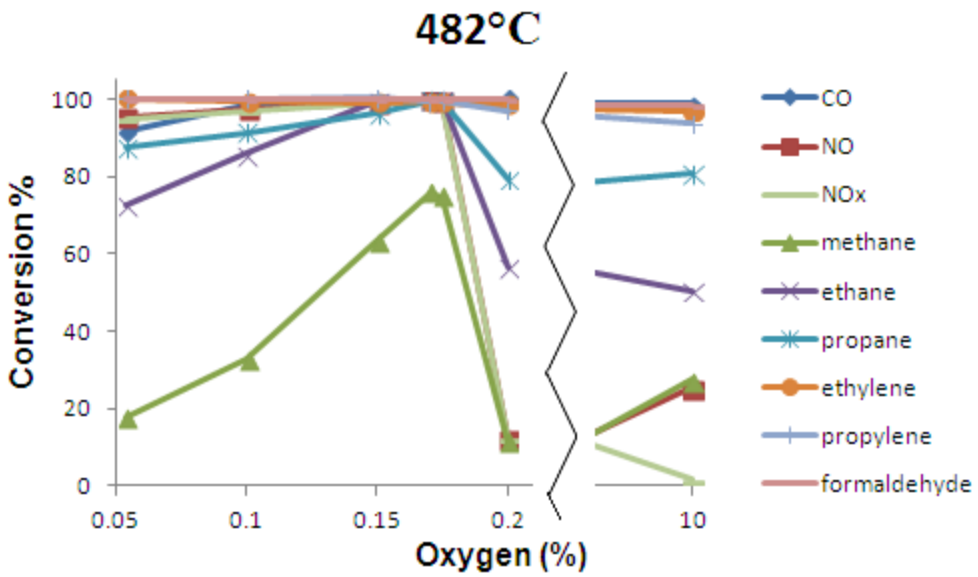

Figure 4.19 NSCR Conditions on DOC4 catalyst (482 °C, GHSV=60,000 h^{-1})

Results for feed temperatures of 538 °C and 593 °C are shown in Figs. 4.20 - 4.21, respectively. At these higher temperatures, the peak overall conversion is easily identified based on the CH_4 and NOx conversions, as the other reactants maintain very high conversion across the entire O_2 feed spectrum. At 538 °C the CH_4 peak occurs at 0.2% O_2, while at 593 °C the CH_4 peak occurs at 0.25% O_2, continuing the trend of the peak shifting to increasing O_2 feed concentrations as temperature increases. The NOx conversion decreases precipitously when O_2 feed concentrations are increased above the value that resulted in decreased CH_4 conversion. At 593 °C the NOx conversion has already decreased somewhat at the 0.25% O_2 feed, so there is likely an intermediate "optimum" O_2 feed concentration between 0.2% and 0.25% that would produce near complete CH_4 and NOx conversion.

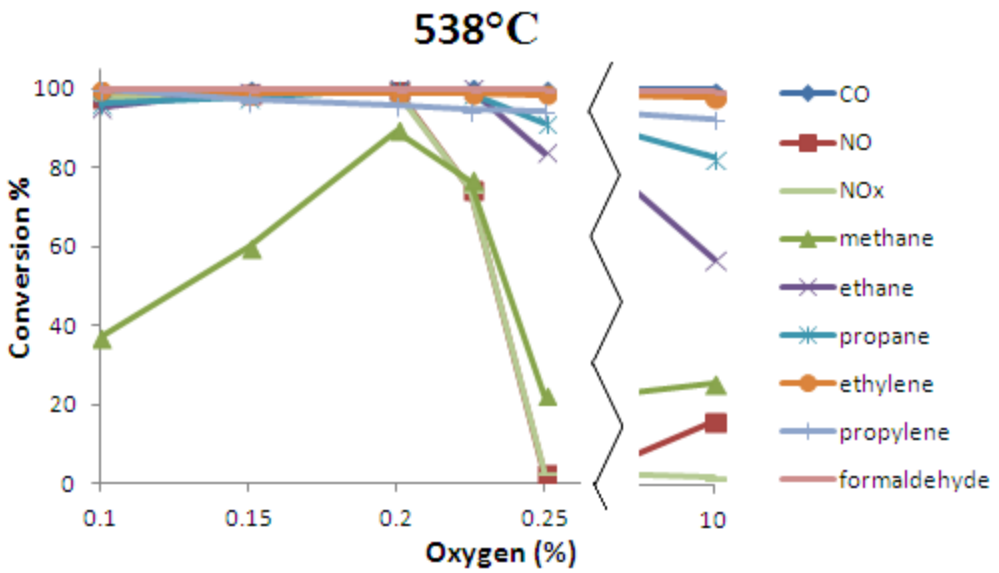

Figure 4.20 NSCR Conditions on DOC4 catalyst (538 °C, GHSV=60,000 h^{-1})

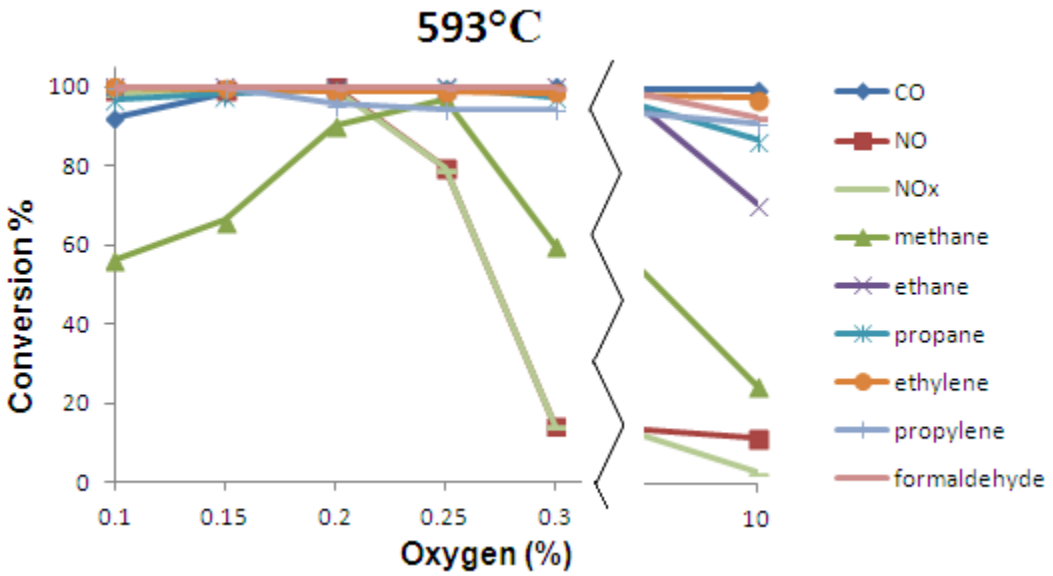

Figure 4.21 NSCR Conditions on DOC4 catalyst (593 °C, GHSV=60,000 h^{-1})

Interestingly, for some HC species their peak conversion at low O_2 feed concentrations significantly exceeds their conversion at 10% O_2. This particularly applies to the more difficult-to-oxidize alkanes. This feature is especially notable for CH_4, which at 538 °C only achieved 26% conversion with 10% O_2 in the feed, but reached a peak of

89% conversion with 0.2% O_2 feed. This is a feature that could possibly be advantageous when designing an emission control system.

Also notable in the DOC4 results is a steep decline in NOx conversion below 0.05% O_2 at 371 °C (Fig. 4.17), and a small decline below 0.1% O_2 at 427 °C (Fig. 4.18). This behavior was not observed with the third party NSCR catalyst (Figs. 4.4 – 4.6); rather the NOx conversion remained high as the feed became progressively richer. The CO conversion also decreased as the O_2 feed concentration was decreased below the peak. This did not occur for the third party NSCR catalyst at GHSV = 60,000 h^{-1}. This indicates that while the DOC4 catalyst is capable of high conversions of both oxidation and reduction reactions, the window of operation is narrower than for the third party catalyst. The third party catalyst continued to reduce NOx to N_2 by oxidizing CO to CO_2 at lower levels of O_2 feed. One possible explanation for this is that the third party catalyst formulation contains materials or promoters that improve the NOx conversion reaction rates at those low O_2 feed concentrations.

Following the completion of testing the third party NSCR catalyst conditions on the DOC4 catalyst, some questions still remain. Why does the peak in conversion of HCs, CO, and NOx exist at low O_2 feed concentrations? How can the conversion of HCs be higher at low O_2 feed than at 10% O_2? These and other questions led us to conduct additional experiments designed to identify the causative factors. For example, perhaps the reaction of NOx with HCs that occurs around the stoichiometric point is somehow better than the catalytic oxidation at high excess O_2. It is known that NO_2 is a good oxidizer (the conversion of NO into NO_2 to aid in DPF regeneration is one function of the

DOC [14–16]) , so tests were then conducted in the absence of NOx, with results shown in Fig. 4.22.

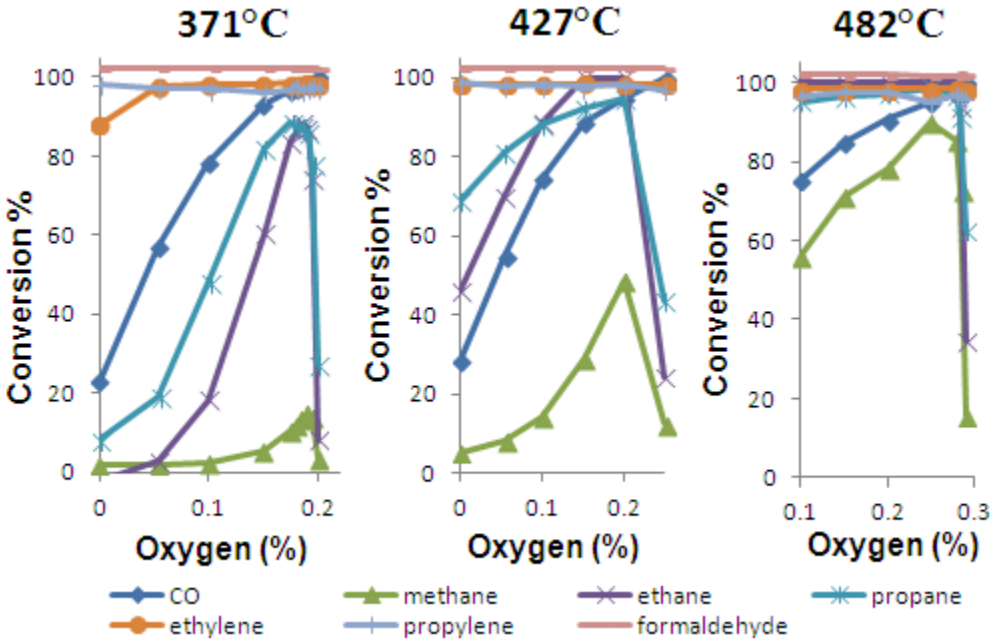

Figure 4.22 NSCR conditions (minus NO) on DOC4 catalyst (GHSV=60,000 h^{-1})

As shown in Fig. 4.22, the peak in HC conversion persists at low O_2 feed concentrations even in the absence of NO. The CH_4 peak conversion actually slightly increases at 482 °C from 76% in the presence of 3000 ppm NO feed to 90% in the absence of NO. This suggests that NO may actually inhibit the HC conversion, perhaps by competing for and occupying some of the active catalyst sites.

It was then considered that H_2O could be contributing to the conditions necessary for the peak in conversions to appear. Perhaps steam reforming reactions produced conditions that contributed to improved overall HC conversion at the peak. Experiments were then carried out in the absence of both NO and H_2O. Results are displayed in Fig. 4.23, showing that the CH_4 peak exists at 0.25% O_2 feed, and is roughly aligned with the decline in CO conversion. Also notable is that the CH_4 conversion is 29% at 10% O_2

feed, whereas when H_2O was present the conversion was only 14%. The H_2O is therefore inhibiting the oxidation of CH_4 under lean conditions.

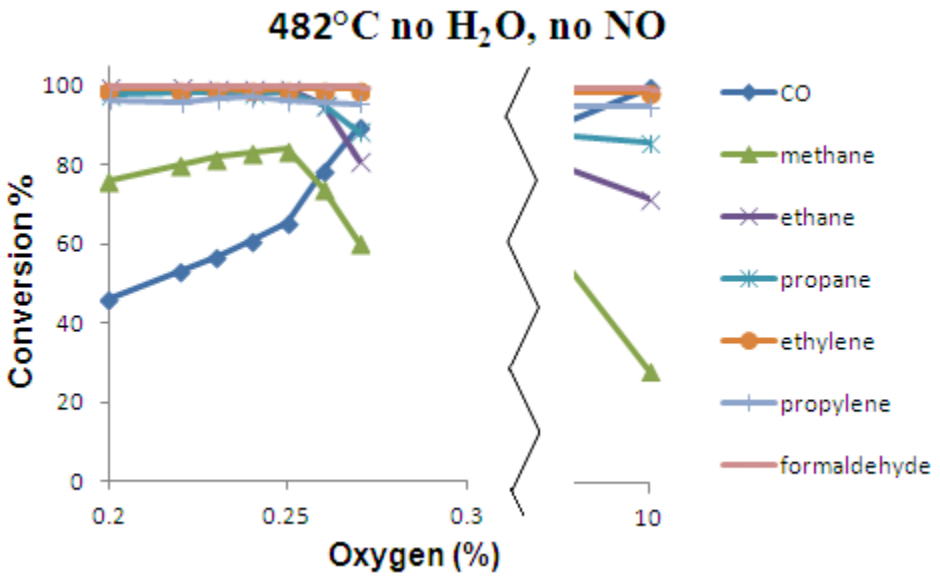

Figure 4.23 NSCR conditions (no NO, no H_2O) on DOC4 catalyst results (482°C, GHSV=60,000 h^{-1})

The next feed component to be eliminated from the reaction mixture was CO. Clearly visible in the results shown in Fig. 4.24 is the disappearance of the peaks in HC conversions for the 0.05%-0.2% O_2 feed range at 427 °C. Upon reintroducing the 3000 ppm CO, conversions of CH_4, ethane and propane increased dramatically, and the peaks are present. Feed gas O_2 concentration was incrementally increased so that a precise plot of the reactant conversions could be realized. Alkane conversions decrease dramatically as CO conversion reaches 100%, which may be a clue in deciphering how the inclusion of CO increases the HC conversions.

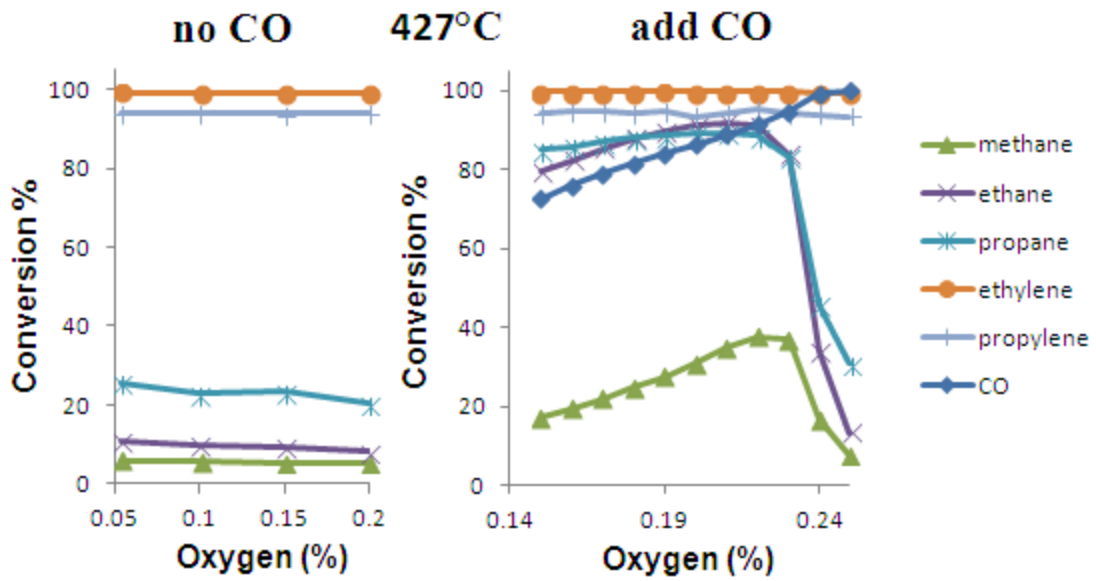

Figure 4.24 Effect of 3000 ppm CO on HC conversions with DOC4 catalyst (T_f = 427 °C, GHSV=60,000 h^{-1})

Finally, the feed mixture was further simplified to include only N_2, 800 ppm CH_4 and varied O_2 to explore the effect with and without 3000 ppm CO. When the other HCs were not present, the CH_4 still had a conversion peak at low O_2 feeds. It was then discovered that the peak existed at even lower O_2 feeds in the absence of CO (Fig. 4.25). The O_2 concentration is in fact the critical parameter; the addition of CO essentially shifts the CH_4 conversion peak to higher O_2 feed concentrations. The CO in the feed stream removes some of the O_2 by reacting with it to form CO_2.

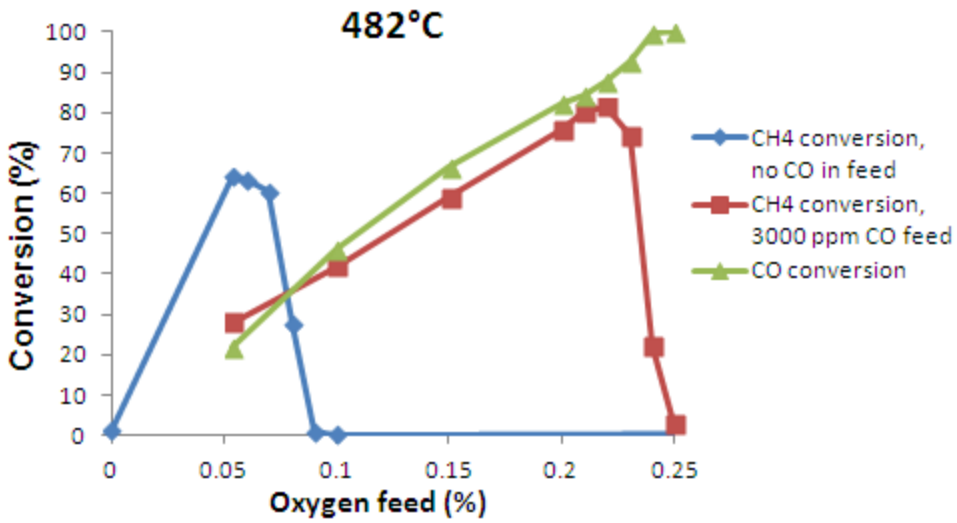

Figure 4.25 CH_4 conversion by DOC4 catalyst with and without CO (T_f = 482 °C, GHSV=60,000 h^{-1})

Another significant finding is the production of CO during conversion of CH_4 at low O_2 feed concentrations in the absence of CO in the feed. Figure 4.26 displays effluent concentrations of CH_4 and CO when there is 3000 ppm CO in the feed and without CO in the feed. The CO production (diamonds) aligns with a dip in effluent CH_4 concentration (aligning with the CH_4 conversion peak in Fig. 4.25). The production of CO indicates that partial oxidation of CH_4 is taking place, and there is likely also H_2 being produced. The H_2 can't be detected by the FTIR, but follow-up studies (Chapter 5) utilize a mass spectrometer to detect and quantify the H_2 production.

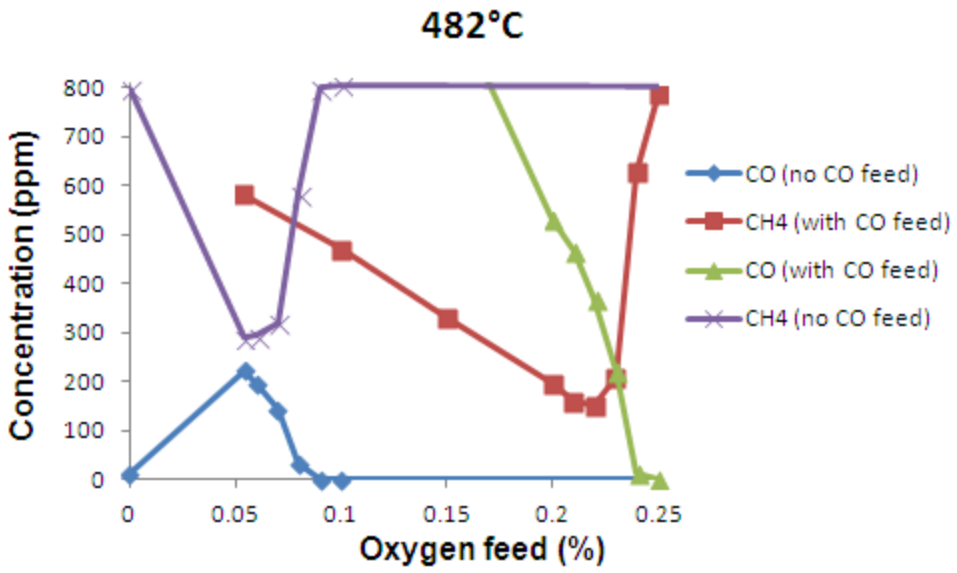

Figure 4.26 CH_4 and CO outlet concentrations (T_f = 482 °C, GHSV=60,000 h^{-1})

4.9 Discussion of Third party NSCR Conditions on DOC4 Catalyst

The performance of the DOC4 catalyst is considered to be good at these specific conditions, as it displayed high conversions for both oxidation and reduction reactions. The third party NSCR conditions included variation of the O_2 feed concentration, a variable that was not present in the third party oxidation catalyst conditions. This variation led to more complex results and interesting behaviors. In addition to the low O_2 concentration feeds used for the third party NSCR experiments, a high 10% O_2 feed condition was also carried out. The high O_2 feed in combination with the high NO feed concentration (3000 ppm instead of 40 ppm) resulted in the measurement of NO conversion, which resulted from the catalytic oxidation of NO with O_2 to form NO_2.

The additional high O_2 feed condition also brought further attention to the peak in conversions at low O_2 feed concentrations. The peak was detected at temperatures of 371 °C through 593 °C, and the HC conversions with 10% O_2 feed were generally lower than the HC conversions at the peak condition. Notably, at temperatures of 482 °C and 538 °C

(Fig. 4.20 – 4.21) the methane conversions were highest at the peak during low O_2 feed but then steeply fell to low conversions as O_2 feed was increased and then conversion rose at the 10% O_2 feed, although not nearly as high as at the peak conversion.

The reactant feed stream was modified by removing NO in order to determine if the presence of NO (or the product NO_2) was a causative factor in the HC conversion peak at low O_2 concentration feeds. As was displayed in Fig. 4.22, the peak was still present in the absence of NO. Experiments were then conducted without H_2O or NO in the feed, but the peaks in conversion persisted (Fig. 4.23).

Finally, CO was removed from the reactant stream and it appeared that the peaks had vanished (Fig. 4.24). After a final simplification of the reactants to only CH_4 and O_2, experiments revealed that a CH_4 conversion peak existed at low O_2 feeds, provided the temperature was high enough and the O_2 feed was low enough (482 °C and 0.05% O_2 in Fig. 4.25). The presence of CO in the feed mixture shifted the location of the peak CH_4 conversion to a higher O_2 feed concentration (Fig. 4.25). The light off temperature for CO is much lower than for methane, so at temperatures where CH_4 oxidation takes place the CO oxidation will also be consuming O_2. The CO competes with CH_4 for O_2, so at very low O_2 feed concentrations the O_2 is the limiting reactant and the CH_4 conversion is lower with CO present than without CO. At increased O_2 feed concentrations, where no CH_4 conversion takes place in the absence of CO, a CO feed and the subsequent oxidation can consume O_2 and enable the oxidation of CH_4 to take place. The oxidant/reductant ratio is apparently a key parameter in the oxidation of CH_4 at low O_2 concentrations and is further explored in Chapter 5.

4.10 Third Party Study Testing Summary

Testing was performed for a third party participant, including a NSCR catalyst under near stoichiometric exhaust conditions and an oxidation catalyst in lean-burn exhaust conditions. For NSCR testing, the optimum O_2 feed to convert both NOx and HC/CO was dependant on temperature. Additionally, NOx was not observed to form across the third party catalysts at any condition, alleviating the client's concerns. The company was satisfied with the results and indicated being open to publication of the results. The TxCEF lab benefitted through increased knowledge, experience and financial support toward continuation of research in the facility laboratory.

The finding of increased CH_4 conversion at low O_2 feed concentrations is of particular interest, given the current trend of increased natural gas usage for vehicle applications. The primary component of natural gas is CH_4 and a portion of the CH_4 does not burn in the engine and "slips" into the exhaust. Since CH_4 is a greenhouse gas, there will be growing interest in catalytic aftertreatment of the CH_4. As displayed in the results of this study, CH_4 is particularly difficult to treat compared to other HCs. For these reasons, further research into the CH_4 conversion at low O_2 feed levels is warranted.

5. Anomalous Steady-State and Spatio-Temporal Features of Methane Oxidation on $Pt/Pd/Al_2O_3$ Monolith Spanning Lean and Rich Conditions

Note: This chapter is reproduced with permission from Elsevier from the article of the same title published in Applied Catalysis B: Environmental 165 (2015) 68-78.

5.1 Abstract

The steady-state and transient features of methane oxidation on a $Pt/Pd/Al_2O_3$ washcoated monolith are reported for a wide range of temperatures and feed gas compositions. Above 400 °C the methane conversion dependence on the O_2 feed concentration exhibits a multiplicity of states. With increasing temperature the multiplicity, in the form of a clockwise hysteresis in the rich regime, expands over an expanding O_2 concentration range. At the highest temperature considered (538 °C) extinction occurs near the rich-lean transition ($O_2/CH_4 = 1.9$) while ignition occurs at $O_2/CH_4 \sim 0.6$. A low conversion state exists for all O_2 concentrations exceeding the ignition concentration at this temperature. In the rich regime, multiple high conversion states are encountered, all of which produce a mixture of CO, CO_2, H_2, and H_2O. Only the lowest conversion branch of this group is a steady-state. Another high conversion branch is encountered for O_2 concentrations spanning a wide lean regime ($2 < O_2/CH_4 < 125$). Spatially resolved capillary-inlet mass spectrometry (SpaciMS) measurements reveal two primary zones within the monolith. In the front zone, complete oxidation of methane to CO_2 is dominant until the O_2 concentration decreases downstream below a critical value. Beyond that point both CO and H_2 are produced, revealing the emergence

of methane partial oxidation, steam reforming, and water gas shift (WGS). Transmission electron microscopy and energy dispersive spectroscopy reveal a distribution of Pt/Pd ratios ranging from 10 (Pt-rich) to 0.2 (Pd-rich), and particles having an average size of ~15-20 nm. Accordingly, the conversion trends and spatiotemporal data are interpreted with a mechanistic model accounting for contributions by Pt, Pd, and PdO phases. For example, methane conversion in the lean regime is likely dominated by an active PdO phase while the rich oxidation behavior is strongly affected by the oxygen self-poisoning on metallic Pd and Pt sites. The low conversion branch is attributed to inhibition by O_2 adsorption occupying the metallic catalyst sites, although the state is unstable in the lean regime as the more active PdO phase forms. The multiple high conversion state branches in the rich regime and the associated slow transient approach to a single stable high conversion branch is attributed to the supply of oxygen from the underlying bulk of PdO which favors methane partial oxidation.

5.2 Introduction

Advances in hydraulic fracturing technology have led to low-price domestic natural gas, increasing the economic incentive for natural gas powered engines [125]. As a result, the use of natural gas (NG) as a transportation fuel in the liquefied (LNG) and compressed (CNG) forms is expected to grow. LNG and CNG vehicles generally have lower emissions of particulate matter (PM), SOx, and non-methane hydrocarbons (NMHC). On the other hand, methane emissions from NG-powered vehicles are much higher than gasoline- and diesel-fueled vehicles. Historically, vehicular emissions regulations have excluded methane from the HC limits, instead placing restrictions on NMHCs or non-methane organic gases (NMOG). While methane does not contribute to

ozone formation, it is a potent greenhouse gas with a global warming potential more than 20 times that of CO_2 [14]. A consequence of this fact is the expected emergence of more stringent methane emissions regulations in the coming years. For this reason there is renewed interest in the development of improved catalytic converters for NG-powered vehicles.

While most hydrocarbons (HCs) and carbon monoxide (CO) emitted from internal combustion engines are readily abated by noble metal (Pt, Pd) catalyzed oxidation, CH_4 is notoriously non-reactive [15, 16]. Stoichiometric (spark-ignited) NG-powered combustion engines have a comparatively low exhaust concentration of O_2 (< 2%) so the three-way catalyst (TWC) is effective in simultaneously oxidizing CO and NMHC's and in reducing NOx. The much less reactive methane passes through a monolith comprising Pt/Al_2O_3 with little conversion at relevant space velocities (> 10k h^{-1}) and temperatures below 400 °C [17]. In contrast, lean-burn NG vehicles generally utilize Pd-based catalysts, and the large excess of oxygen in the exhaust readily forms palladium oxide (PdO), which is quite active for methane oxidation [18, 19]. However, temperature excursions that may occur are problematic since PdO decomposes at temperatures exceeding ~600 °C even under oxidizing conditions [20, 21]. This can lead to a decrease in conversion due to the lower activity of metallic Pd. Indeed, the dynamics of the PdO/Pd interconversion can result in variations in the methane conversion with time-on-stream [22–26]. For example, it was reported that for Pd catalysts the CH_4 conversion depends on the direction of the change in feed composition [27, 28]. The transient behavior is exacerbated by catalyst deactivation primarily through Pd crystallite agglomeration at high temperature. The addition of Pt to Pd/PdO has been reported to

inhibit this sintering [29]. Recent work has shown that bimetallic Pt-Pd catalyst formulations have improved thermal stability compared to Pt- or Pd-only catalysts [30]. Further, the emergence of "dual fuel" CNG + diesel powered engines means that Pt/Pd catalysts will be used for methane oxidation since this is the common composition of diesel oxidation catalysts (DOCs). For these reasons, Pt/Pd formulations are interesting catalyst candidates for methane oxidation in the exhaust of lean-burn vehicles.

It is instructive to provide a mini-review of the extensive literature for the catalytic oxidation of methane on Pt, Pd, and Pt/Pd catalysts. Earlier fundamental research carried out of methane oxidation on Pt and Pd catalysts reveals several notable features. Gelin and Primet [16] reviewed the complete oxidation of methane on noble metal catalysts. In general, Pt is the more active catalyst under rich conditions whereas Pd is the more active catalyst under lean conditions [27, 126]. The reason for the latter is the formation of PdO, the more active form. In comparison, Pt oxide (PtO_2) is unstable above 400 °C, which is the minimal temperature needed to achieve a non-negligible conversion of methane at relevant space velocities. That said, Pt is more likely to exist in metallic form. On Pt and Pd catalysts exposed to rich conditions methane is converted to partially-oxidized products CO and H_2 in addition to CO_2 and H_2O. Enhanced methane conversion at low oxygen feed concentration (fuel-rich) has previously been reported by Oh et al. [27], Subramanian et al. [127, 128], and Lyubovsky et al. [129] over Al_2O_3-supported Pt and Pd. On Pt, methane oxidation exhibits a rate/conversion maximum with respect to O_2 concentration [130, 131]. The maximum demarcates a positive order regime (~1), in which the oxidation rate is limited by O_2 adsorption, from a negative order regime (~ -1), in which the rate is inhibited by chemisorbed oxygen adatoms. The negative-order regime

traverses the $O_2/CH_4 = 2$ stoichiometric ratio. Under lean conditions Pd takes up much more than one monolayer of oxygen atoms. Corresponding to this uptake is an increase in the oxidation activity, clearly indicating that the existence of PdO, probably in a mixture with metallic Pd, is essential to provide activity. Under similar conditions on Pt, methane conversion is negligible due in part to the aforementioned instability of Pt oxide and site blocking by chemisorbed oxygen.

A deeper fundamental understanding of the mechanistic features of methane oxidation is emerging. Epling and Hoflund [132] showed that a mixture of Pd metal and PdO has a higher activity than Pd or PdO alone. They suggest that the Pd metal surface more easily dissociates the methane and that CH_x reaction intermediate surface species migrate to the PdO to be oxidized. Bell and coworkers [133, 134] have advanced a similar mechanism: The dissociative chemisorption of methane is the rate-limiting step and that metallic Pd enhances its rate. The kinetics of lean methane oxidation on Pd at relevant temperatures (400–800°C) show a first-order dependence on methane and zero-order dependence on O_2 [135]. The first-order dependence is consistent with methane adsorption/activation being the rate limiting step. Iglesia and coworkers presented detailed studies of the kinetics of methane oxidation on supported Pt and Pd clusters [131, 136], complementing their earlier studies of methane oxidation by H_2O and CO_2 [137]. Methane activation on Pd clusters is enhanced on a dual site comprising a vacant metal site (*) and an O-occupied site (O-*) [131]. This builds on a similar mechanism proposed by Fujimoto et al. [138] involving the dissociative oxidation of methane on adjacent Pd and PdO sites forming adsorbed CH_3 and OH, respectively. A recent study by Zhang et al. [139] of methane oxidation on PdO using wire microcalorimetry supports

these ideas. Chin and Iglesia [131] argued that CO_2 and H_2O are the only products of oxidation at low conversion due in part to the much higher reactivity of CO with O-*. Methane oxidation on Pd clusters resulted in lower turnover frequencies because the stronger binding of O to high index planes of Pd means that the catalyst is less effective in activating methane. A number of investigators have shown the reversible nature of Pd oxidation by O_2 and PdO reduction by H_2 and CH_4 [133, 140–142]. This can lead to hysteresis behavior and long transients. Datye et al. [141] attributed the hysteresis in PdO reformation during a temperature decrease to inhibition by strongly bound oxygen on the Pd surface. A recent study by Amin et al. [143] shows interesting hysteresis effects for methane oxidation on a Pt/Al_2O_3 monolith catalyst. Finally, a number of studies have reported that partial oxidation products H_2 and CO are generated under O_2 deficient conditions [144, 145]. The aforementioned differences in reactivity of CO and CH_4 suggests that the generation of H_2 and CO follows a sequential mechanism in which CH_4 and O_2 react first to give CO_2 and H_2O, and then CH_4 reacts with H_2O to form CO and H_2, along with the water gas shift (WGS) reaction.

Recent studies of methane oxidation on combined Pt/Pd catalysts lend support to behavior reported on individual Pt, Pd, and PdO catalysts. This is due in part to the sustained existence of PdO as a separate phase in bi-metallic supported catalysts. The mixture of Pt and Pd is beneficial from both durability and activity standpoints. Narui et al. [29] showed that the addition of Pt to PdO inhibits deactivation through particle growth suppression with flattening of individual PdO crystallites. Ozawa et al. [146], using XRD analysis, showed that high temperature (750-800 °C) catalytic oxidation of methane resulted in less particle growth for a supported PdO catalyst containing a small

amount of Pt compared to Pt-free PdO. Morlang et al. [147] examined bimetallic Pt/Pd catalysts after thermal aging and found that PdO and Pt/Pd particles were both present. Further, they showed that the alloyed system resisted sintering. Persson et al. [148] carried out a systematic study of six catalysts for lean methane oxidation. They found that the most active and stable catalysts were $Pd_{67}Pt_{33}$ and $Pd_{50}Pt_{50}$. Based on TEM imaging they concluded that PdO is present in close proximity to Pt/Pd alloyed crystallites. Johns et al. [149] used a combination of spectroscopies to suggest that after high temperature calcination in air PdO is present as a separate phase in the presence of Pt/Pd with no evidence of oxide formation on the Pt/Pd metallic crystallites.

In this study we employ spatially resolved capillary-inlet mass spectrometry (SpaciMS) to follow the catalytic pathways of methane oxidation over a range of conditions. First developed by Partridge and coworkers [94, 95] at Oak Ridge National Lab, SpaciMS has been shown to be a powerful tool for following catalytic reaction pathways by uncoupling the integral nature of monolith reactors. Choi et al. [150–153] studied NOx storage and reduction using SpaciMS determined the amount of catalyst required for storage varied based on sulfur exposure of the storage component and sintering of the precious metal components. Other studies [154–157] have employed SpaciMS to decipher the integral production and consumption of species during the regeneration of lean NOx traps. Schmidt and coworkers [158] showed using SpaciMS that the oxidation and reforming zones depend on the precious metal identity (Pt, Pd, Rh).

Recently, measurements involving a spatio-temporal approach have investigated the effects of the capillary inside the channel of the monolith. In addition to their SpaciMS work [159–163], Epling et al. have used as well a Spaci-FTIR [104, 105, 164]

in spatio-temporal measurements of various reaction systems. More recent work by the Deutschmann group has shown that capillary probe technique may introduce a systematic error due to flow restriction presented by the probe [97]. The restriction may result in a lower flow rate in the probe channel which would tend to lead to a higher conversion as a result of the longer contact time. The presence of the capillary restricts the flow rate in the channel containing the capillary which leads to an increase in flow in adjacent channels. This issue has been debated by Goguet and Partridge [98] who claim that Deutschmann's findings cannot be applied to different systems without considering the configuration, and operating conditions. Deutschmann et al. have presented a response that systematically discusses the concerns proposed by Goguet et al. [99]. While this debate remains unresolved, we believe the SpaciMS technique provides a valuable in situ probe of the integral nature of reaction systems. However, some caution should be exercised in the application of quantitative SpaciMS data.

While a deeper understanding of methane oxidation on individual precious metal catalysts has emerged, studies of methane oxidation on combined Pt/Pd catalysts supported on monoliths has been comparatively sparse. To this end, in this study we investigate the oxidation of methane on a standard Pt/Pd monolithic catalyst. Wide ranges of O_2 feed concentrations and catalyst temperatures are investigated to map the methane conversion and product distribution. We determine the steady-state dependence, differentiate between steady-states and long transients, and identify transitions (bifurcations) between the different branches. SpaciMS measurements provide insight into the interplay between chemical species as they react through the length of the monolith through key trends. Transmission electron microscopy and energy dispersive

spectroscopy measurements provide insight about the size and composition of the metallic nanoparticles. Finally, a phenomenological model of the reaction system is described that is consistent with the measurements.

5.3 Experimental

The bench flow reactor setup (Fig. 5.1) includes mass flow controllers (MKS) for metering of cylinder-supplied gases (Praxair, Matheson), a quartz tube reactor within a tube furnace (Lindberg/Blue) and multiple thermocouples (Omega) for temperature monitoring and control. Heat tracing of post reactor lines minimized condensation. Gas composition analysis was accomplished by FTIR (Thermo Scientific Nicolet 6700) and mass spectrometer (Pfeiffer GSD 301). The FTIR was used to measure CH_4, CO and CO_2 concentrations in the bulk gas reactor effluent, as well as to confirm reactor feed concentrations through the use of a bypass line. The mass spectrometer capillary was connected by a computer-controlled stage (Zaber Technologies Inc.) for spatially-resolved intra-channel measurements (SpaciMS). The fused silica capillary was inserted from the downstream end of the reactor (Fig. 1) and had inner and outer diameters of 150 μm and 363 μm, respectively. SpaciMS measurements were generally not taken at the very end of the monolith sample (2.5 cm) due to difficulty in reinserting the capillary into the channel. The gas concentration measurements enabled the closure of C, O, and H balances within +/-10% during steady-state operation. Custom end pieces were fabricated to accommodate the thermocouple and SpaciMS capillary. Graphite/Vespel™ ferrules were utilized so that capillary measurements could be taken simultaneously with the FTIR effluent gas composition measurements.

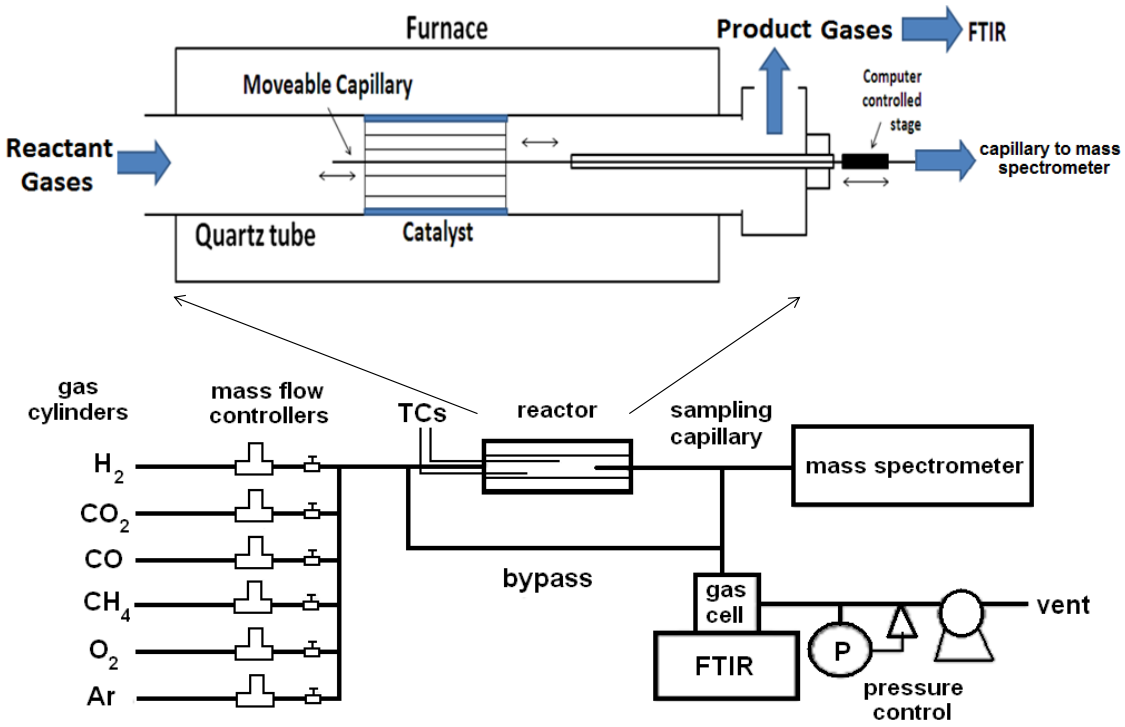

Figure 5.1 Experiment setup and spatially resolved concentration measurement setup

The catalyst used in this study was a washcoated 400 cpsi cordierite monolith containing 60 g/ft^3 Pt/Pd in a 2:1 ratio by weight (~1:1 molar ratio) on γ-Al_2O_3 alumina support with a total washcoat loading of 1.4 g/in^3 (0.085 g/cm^3; supplied by BASF, Iselin, NJ). The sample core was cut to 1.27 cm diameter and 2.54 cm length using a diamond-tip cylindrical drill bit. Experiments were carried out using Ar as the diluent gas with a gas hourly space velocity (GHSV) of 60,000 h^{-1} based on the overall monolith sample volume and standard conditions. Reported experimental temperatures were measured by a type K 0.51 mm o.d. thermocouple positioned 2 mm upstream of the front face of the catalyst. The typical methane concentration was 800 ppm while the O_2 was varied within the range of 100 ppm (0.01%) and 10% (by volume) with balance Ar. The stoichiometric number S_N is used to characterize the oxidant/reductant ratio:

$$S_N = \frac{2C_{O2}}{(4C_{CH4} + C_{CO})}, \quad (5\text{-}1)$$

where C_i is the gas feed concentration of species i. Thus the gas mixture is lean if $S_N > 1$, stoichiometric if $S_N = 1$, and rich if $S_N < 1$. Finally, an estimate of the adiabatic temperature rise for the complete oxidation of 800 ppm CH_4 is ~30 ^oC, so the feed gas temperature was representative of the catalyst temperature.

Transmission electron microscopy (TEM) studies were performed at the Texas Center for Superconductivity at the University of Houston for catalyst characterization. The JEOL 2000FX and JEOL 2010 microscopes are equipped with energy dispersive spectrometers and were operated at 200 kV. Samples were prepared by removing some $Pt/Pd/Al_2O_3$ washcoat from a relatively "fresh" monolith sample, suspending the resulting powder in ethanol, and then ultrasonicating and distributing the mixture onto a 300-mesh carbon-coated copper grid. Conventional and high resolution TEM imaging and energy-dispersive spectroscopy (EDS) methods enabled the analysis of metal particle size and atomic composition.

5.4 Results

The dependence of the methane conversion on the O_2 feed concentration reveals complex behavior. In the experiment represented in Fig. 5.2.a the O_2 feed concentration was varied over a wide range (0.01 to 10 %) while the feed temperature was fixed at 538°C and methane feed concentration fixed at 800 ppm. Fig. 5.2.b shows an expansion of the low concentration range (O_2 concentration < 0.5%). At this methane concentration the O_2 concentration required for complete oxidation is 1600 ppm (0.16%); this corresponds to the $S_N = 1$ value. The behavior in the rich ($S_N < 1$) and lean regimes ($S_N > 1$) are seen to be quite different. The data include a high conversion branch at higher O_2

concentration (S_N > 1), a clockwise hysteresis loop at low concentrations (S_N < 1), and a low conversion state that extends over nearly the entire O_2 concentration range (0.4 < S_N < 65). Each of these is described in more detail next.

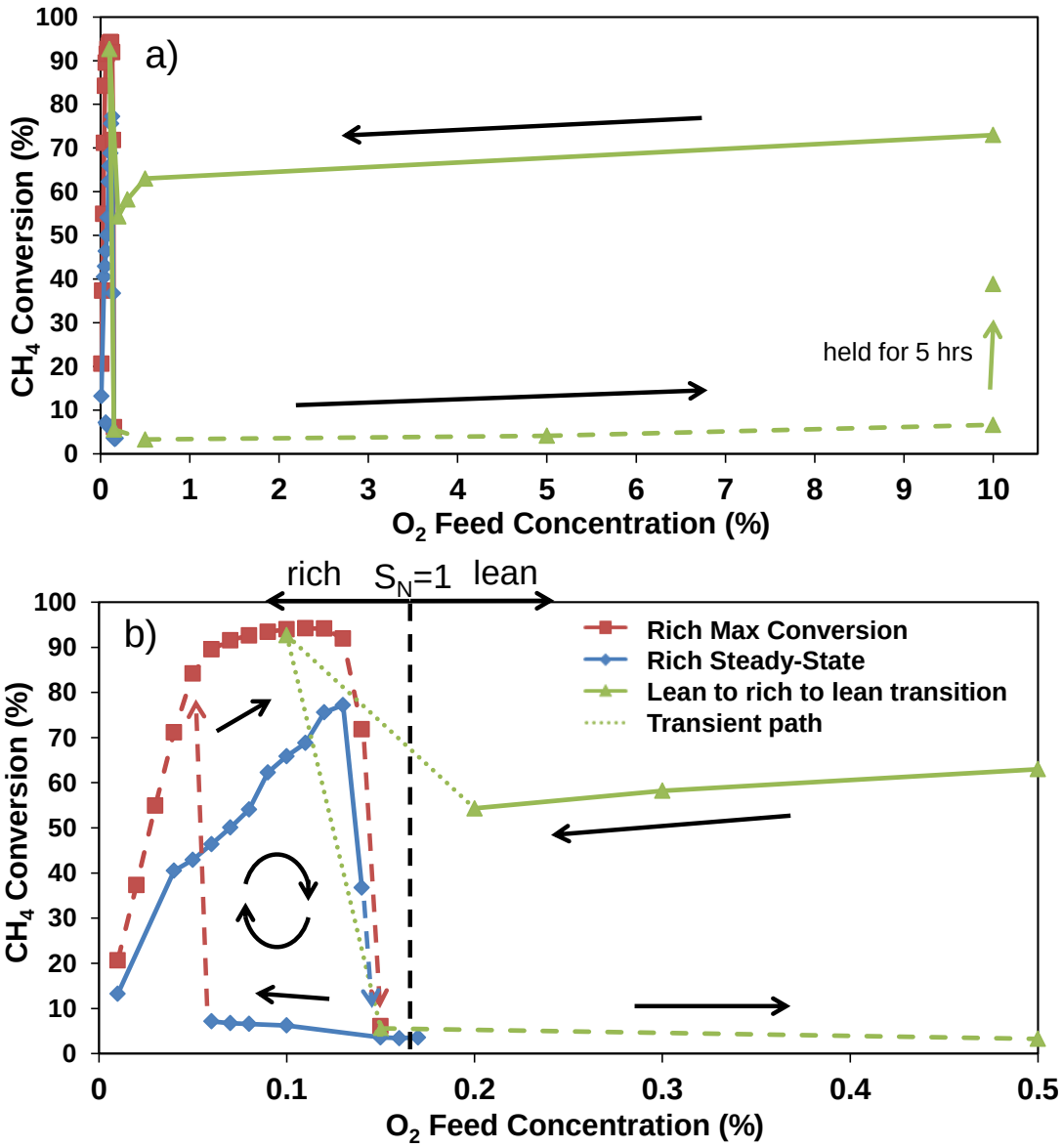

Figure 5.2 Dependence of CH_4 conversion on O_2 feed concentration (T_f = 538 °C, 800 ppm CH_4, GHSV=60,000 h^{-1})

The lean oxidation resulted in a moderately high methane conversion (Fig. 5.2.a). The data point at 10% O_2 and 73% conversion was obtained after ramping the feed temperature at a rate of 5 °C/min from 25 °C to 600 °C while the feed composition was

held at 800 ppm CH_4 in 10% O_2/Ar. The temperature was then lowered to 538 °C and the methane conversion eventually reached the indicated steady-state value of 73%. Several successive temperature ramps (up and down) were carried out to ensure that the catalyst was in the fully oxidized state.

The oxidized catalyst exhibited relatively high activity with the methane conversion dropping slightly from 73% at 10% O_2 to 63% conversion at 0.5% O_2. Decreasing the O_2 feed concentration to 0.2% led to a sharper conversion drop to 54%. A further decrease to 0.1%, which traversed the $S_N = 1$ boundary (0.16%), led to an increase in the methane conversion to over 90%; this transition is indicated by the dotted 'transient path' line in Fig. 5.2.b. A subsequent increase in the O_2 feed concentration from 0.1% to 0.15% resulted in an extinction to a low conversion branch. This was followed by an increase in the O_2 concentration back to the lean regime (0.5%). However, the catalyst remained in a low conversion state. We return to the stability of this low conversion branch later.

Methane conversions exceeding 90% were observed in the rich regime, but these high conversion levels were mostly of a transient nature and were manifested as multiple branches of states. By "transient" we imply time-dependent or non-steady-state. In a typical experiment, methane oxidation was initiated from ambient temperature to the final temperature of interest, and then successive increases and decreases in the O_2 feed concentration were carried out while holding the temperature constant. Figure 5.3 shows the results at an O_2 feed concentration of 0.05% (rich regime) and feed temperature of 538 ^{o}C, which was achieved with a 5 ^{o}C/min ramp. One hour after the ramp was stopped the temperature settled at 538 °C while the CH_4 conversion settled at ~80%. The O_2 feed

concentration was then increased to 0.17%, causing an extinction, then decreased to 0.05% to achieve ignition and re-establish the high conversion state, shown as the 84% conversion value at 0.05% O_2 in Fig. 5.3. The O_2 feed concentration was then increased in 0.01% increments to 0.15% which traced out the highest methane conversion branch shown in Fig. 5.3. The peak methane conversion of 94% was observed at 0.11% O_2. It is noted that this highest conversion branch was of a transient nature; i.e., without a temporary increase in the O_2 concentration to the lean regime the methane conversion gradually decreased over time. We return to this point later.

The low methane conversion branch was encountered when the O_2 feed concentration was increased to 0.15%, which resulted in extinction from the high conversion branch to a low conversion branch. A subsequent gradual decrease in the O_2 concentration from 0.15% to 0.05%, while the catalyst was in the low conversion state, resulted in an ignition with the methane conversion increasing to 84%. Both the extinction and ignitions were reproducible in terms of the O_2 feed concentrations of 0.15% and 0.05%, respectively. The low conversion steady-state, at least for O_2 concentrations less than ~0.2%, appeared to be stable.

The hysteresis loop existing in the rich regime was characterized by more than one high conversion branch which spanned O_2 feed concentrations approaching ~0% to a concentration near the stoichiometric limit (S_N = 1: 0.16% O_2). More than one high conversion branch was obtained depending on the starting point and history. It is interesting to note that some of the CH_4 conversion points obtained at a low O_2 feed concentration (<0.2% O_2) exceeded the highest methane conversion in the lean regime which had O_2 concentrations up to 10%. The multiple high conversion branches were

obtained through various strategies of adjusting the O_2 feed concentration. For example, starting in the lean regime (~0.5%), the O_2 feed concentration was lowered to just below 0.05%, prompting an ignition, then lowered briefly to 0.02%, and then increased to 0.1%. These steps resulted in a methane conversion that approached the indicated 70% (Fig. 5.3). If the same initial sequence of steps was followed but the O_2 concentration was instead increased just after ignition, the methane conversion followed a different locus of values.

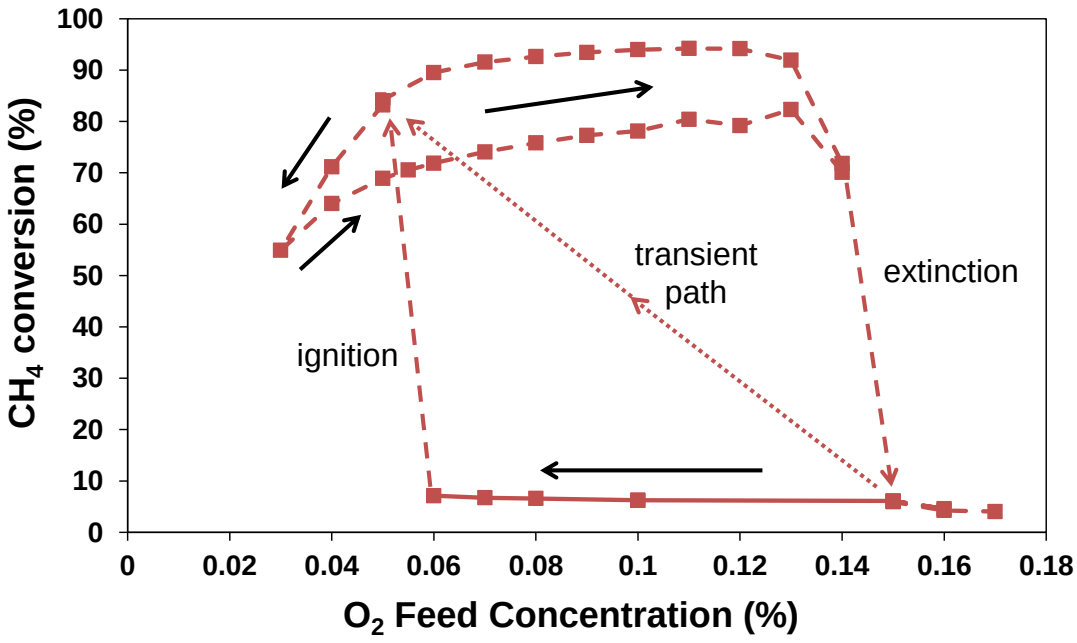

Figure 5.3 Methane conversion dependence on O_2 feed concentration. The arrows show the directions of increases and decreases in the O_2 feed concentration. (T_f = 538 °C, 800 ppm CH_4, GHSV=60,000 h^{-1})

The lower of the two high conversion branches in Fig. 5.3 was obtained upon decreasing the O_2 concentration after ignition from the low conversion branch. The methane conversion dropped to 71% at an O_2 feed concentration of 0.04%, and to 55% as the O_2 was decreased further to 0.03%. Increases in O_2 feed from this point traced the lower of the high conversion branches in Fig. 5.3. As described earlier, the higher of the two high conversion branches was obtained by ignition from the extinguished branch.

After reaching a lower conversion branch, the higher transient methane conversion branch in the rich regime could be recovered by briefly exposing the catalyst to a stoichiometric excess of O_2 then lowering the O_2 to 0.05% to achieve ignition.

Extensive operation of the reaction in the high conversion rich regime led to the conclusion that there was only one truly stable high methane conversion branch. Fig. 5.4 depicts the transient trend of the higher conversion states of gradual approach to a lower bound high conversion branch. The transient approach to the stable branch was rather slow, taking on the order of several hours. As we expand upon later, we speculate that the long transients are symptomatic of a depleting supply of oxygen from the bulk of the PdO phase of the bimetallic crystallites. The transient approach to steady-state was faster at lower O_2 feed concentrations. We exploited this feature to systematically converge on the ultimate steady-state conversion branch through repeated O_2 feed decreases and increases.

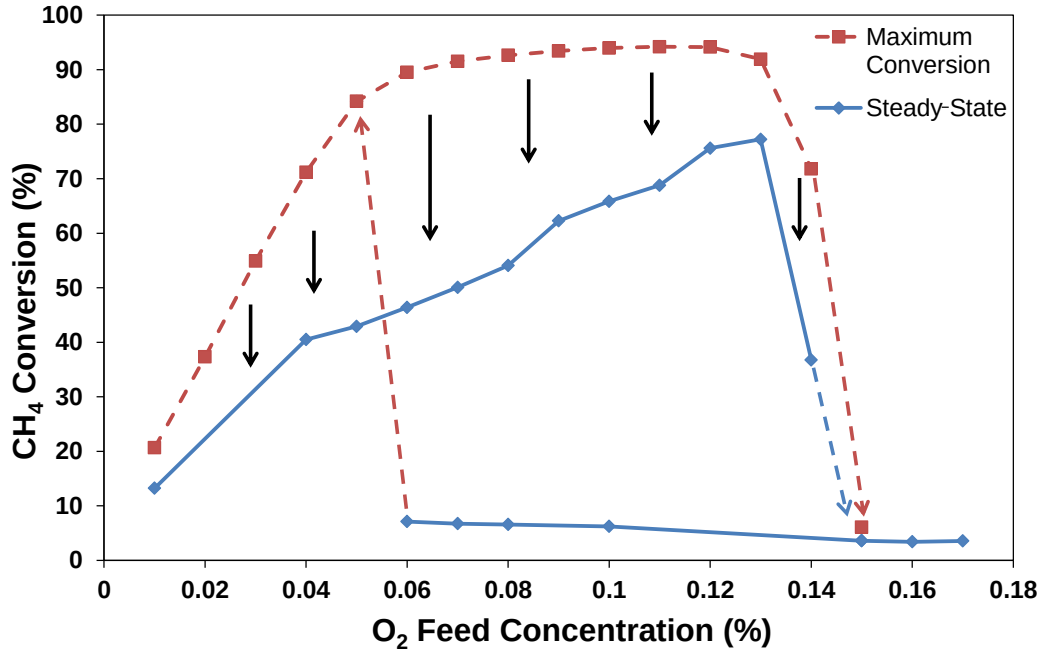

Figure 5.4 Maximum conversion after light-off (red squares, ■) will eventually decrease to steady-state (blue diamonds, ♦) (T_f = 538 °C, 800 ppm CH_4, GHSV=60,000 h^{-1})

The response of the catalyst at O_2 feed concentrations beyond the rich regime exhibited complex behavior. Instead of decreasing the O_2 feed concentration after extinction at 0.15% in the 538 °C experiment the O_2 concentration was increased into the lean regime (> 0.16%). This resulted in the methane conversion remaining quite low (<5%), resulting in a low conversion branch that spanned O_2 concentrations from 0.06% up to the highest value of 10% (Fig. 5.2.a). However, we found upon further investigation that there was evidence for the low conversion branch becoming unstable in the lean regime. Fig. 5.5 shows typical data of a slow increase in the methane conversion when the O_2 feed concentration was held at 10%. We did not pinpoint the exact O_2 feed concentration above which this low branch became unstable, but it was within the lean regime.

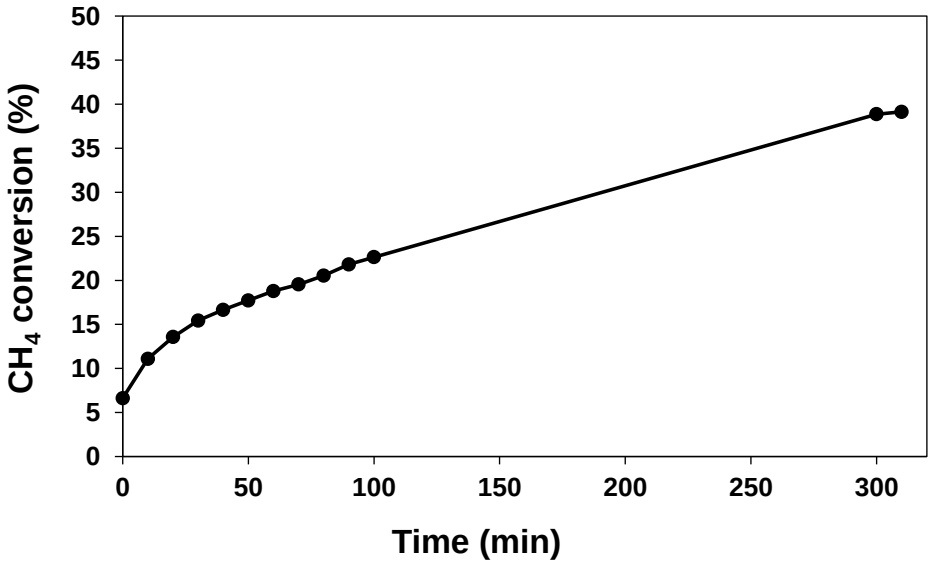

Figure 5.5 Transient increase in the CH_4 conversion from low conversion branch under lean conditions (T_f = 538 °C, 800 ppm CH_4, 10% O_2, GHSV=60,000 h^{-1})

Selectivities of the carbon-containing oxidation products (S_{CO},S_{CO_2}) and the O_2 conversion were quantified in the rich regime. Fig. 5.6 shows the S_{CO} and S_{CO_2} selectivities (defined as the percentage of CH_4 converted to either CO or CO_2,

respectively) along two of the upper branches. Note that no other C-containing species were detected, so necessarily $S_{CO} + S_{CO_2} = 100$. In addition, the O_2 conversion was 100% (complete) for all of the points along the upper branches reported in the earlier figures and in Fig. 5.6. This was confirmed by the lack of any measureable O_2 peaks in the mass spectrometer. The data show that CO selectivity decreases with increased O_2 feed concentration, with a corresponding increase in CO_2 selectivity. In addition, at a fixed O_2 feed concentration, S_{CO} increases with increasing methane conversion. This latter observation is consistent with the fact that a higher methane conversion infers a higher ratio of the C consumed to O consumed. Finally, along the low methane conversion branch CO_2 was the only C-containing product; i.e. $S_{CO_2} = 100\%$.

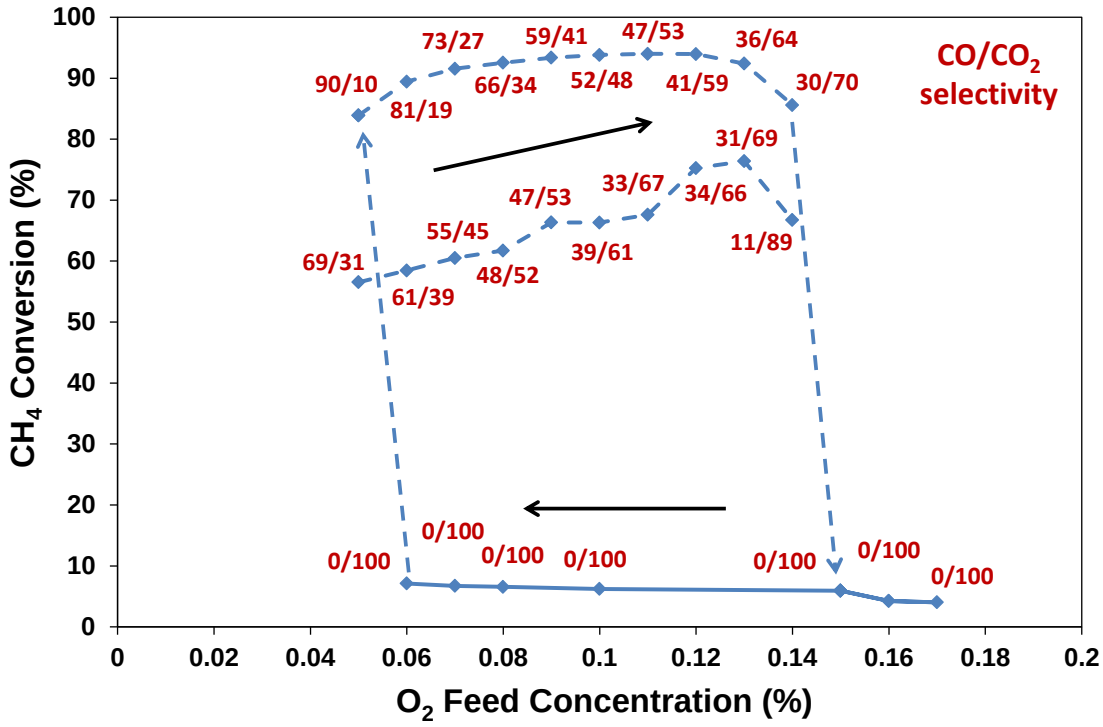

Figure 5.6 Carbon selectivity for methane conversion to CO and CO_2 (T_f = 538 °C, 800 ppm CH_4, GHSV=60,000 h^{-1})

Experiments carried out with lower feed temperatures revealed a similar clockwise hysteresis behavior in the rich regime. Fig. 5.7 shows the results for three

different temperatures spanning 427 to 538 °C. The size of the hysteresis loops decreased with decreasing temperature, as determined by the magnitude of the maximum methane conversion and the range of O_2 feed concentrations over which multiple states were observed. At higher catalyst temperatures there was an increase in the maximum conversion and a broadening of the range of O_2 concentration over which a high methane conversion could be sustained. While the qualitative behavior is similar, the methane conversion decreased notably with decreasing feed temperature. For example, the maximum methane conversion was 25% at 0.025% O_2 for 427 °C and 62% at 0.06% O_2 for 482 °C, in comparison to 94% obtained at 0.11% for 538 °C.

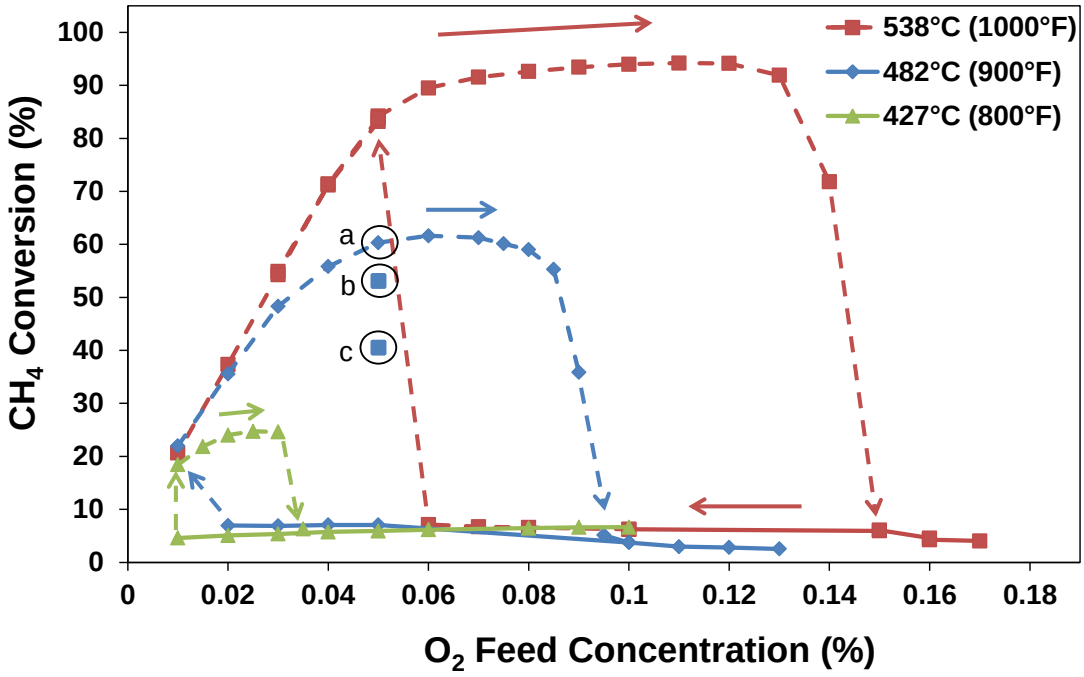

Figure 5.7 Methane conversion dependence on O_2 feed concentration at 538, 482, and 427 °C (800 ppm CH_4, GHSV=60,000 h^{-1}). Note: points a, b, and c are referred to in Fig. 5.10

Transmission electron microscopy (TEM) combined with energy dispersive spectroscopy (EDS) provided important insight into the nature of the Pt/Pd particles. Fig. 5.8 displays a representative micrograph showing Pt-Pd nanoparticles appearing as dark

dots in the grayish transparent particles of the alumina support. Some of the alumina particles have an elongated shape. Metallic particle sizes range from 10 to 40 nm, with a mean size of ~15-20 nm. The figure includes arrows with black, gray, and white shade; these respectively correspond to Pt-Pd particles having compositions corresponding to Pt-rich (Pt/Pd > 1.5), PtPd (Pt/Pd = 0.67 to 1.50), and Pd-rich (Pt/Pd < 0.67). The size and morphology of the nanoparticles does not appear to depend on the composition. No monometallic Pt or Pd particles were identified; however, the bimetallic compositions did cover a wide range.

A total of 55 particles were analyzed from three separate locations on the grid, with each location yielding a different average Pt/Pd molar ratio. The first location contained many Pd-rich particles, with 8 out of 25 analyzed containing >60% Pd, with the maximum being an 83% Pd particle. The average composition of the first location was 52:48 Pt:Pd, which is very near the catalyst manufacturer's stated ~50:50 composition. Two additional locations analyzed were Pt-rich, with average compositions of 78:21 Pt:Pd and 64:36 Pt:Pd. The overall average atomic composition of the particles analyzed from the three locations came to 64:36 Pt:Pd. This make-up differs from the manufacturer's stated composition, however it is likely that a larger sampling would lead to an average closer to the expected Pt/Pd = 1 ratio.

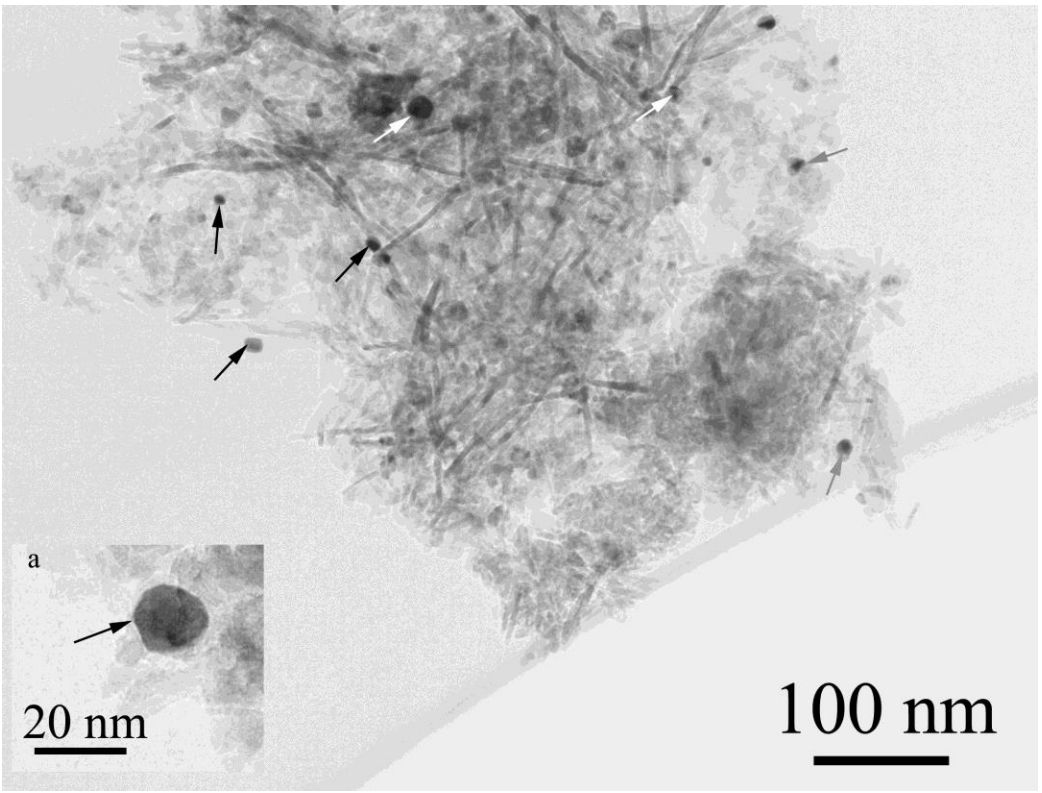

Figure 5.8 Conventional bright field TEM image of the Pt-Pd nanoparticles embedded into alumina. One nanoparticle is shown at the higher magnification in the insert a. Shaded arrows indicate particles with composition Pt-rich (gray), Pd-rich (white), or equimolar (black)

Spatially resolved concentration measurements provide detailed insight about the evolution of reaction pathways within the reactor. This is of particular interest in the rich regime in which products from both partial and complete oxidation of methane were observed. Fig. 5.9 shows concentration profile data for three different O_2 feed concentrations spanning lean (Fig. 5.9.a: 10% O_2) and rich feeds (Fig. 5.9.b: 0.1%; Fig. 5.9.c: 0.05%) for a feed temperature fixed at 538°C. The spatial position indicates the axial distance from the front face of the monolith; i.e., the front and rear faces of the monolith are at the 0.0 and 2.54 cm positions, respectively.

With a feed containing excess O_2 only complete oxidation occurs. (This is indicated by the green bar denoting complete oxidation.) Fig. 5.9.a. displays the

concentration profiles through the catalyst under the conditions that produced the data point at 10% O_2 and ~70% CH_4 conversion in Fig. 5.2. The CH_4 concentration decreases monotonically from its feed value of 800 ppm while expectedly the CO_2 increases, such that C_{CH4}+ $C_{CO2} \approx 800$ ppm. The H_2O:CO_2 = 2 stoichiometry is evident from the H_2O profile beyond the 0.75 cm mark. At the 2.25 cm mark the SpaciMS measurement gave a CH_4 concentration of 353 ppm, which corresponds to a CH_4 conversion of 56%. Simultaneous measurement of the effluent CH_4 concentration by the FTIR was 258 ppm (68% conversion). The decrease in CH_4 concentration between measurement points (Δz = 0.25 cm) is ~50 ppm (an incremental 6.3% in methane conversion). Extrapolating this to what might be measured by the SpaciMS at the outlet (2.54 cm mark) gives 295 ppm (63% conversion), which is comparable to the aforementioned 68%, indicating good agreement between the FTIR and SpaciMS measurements. The FTIR essentially measures the cup-mixing average outlet concentration, while the SpaciMS obviously only measures the composition in one channel. Differences between single channel and overall conversions may be explained in part by potential variations between channels in temperature, catalyst loading, washcoat thickness, and dilution effects, among other factors.

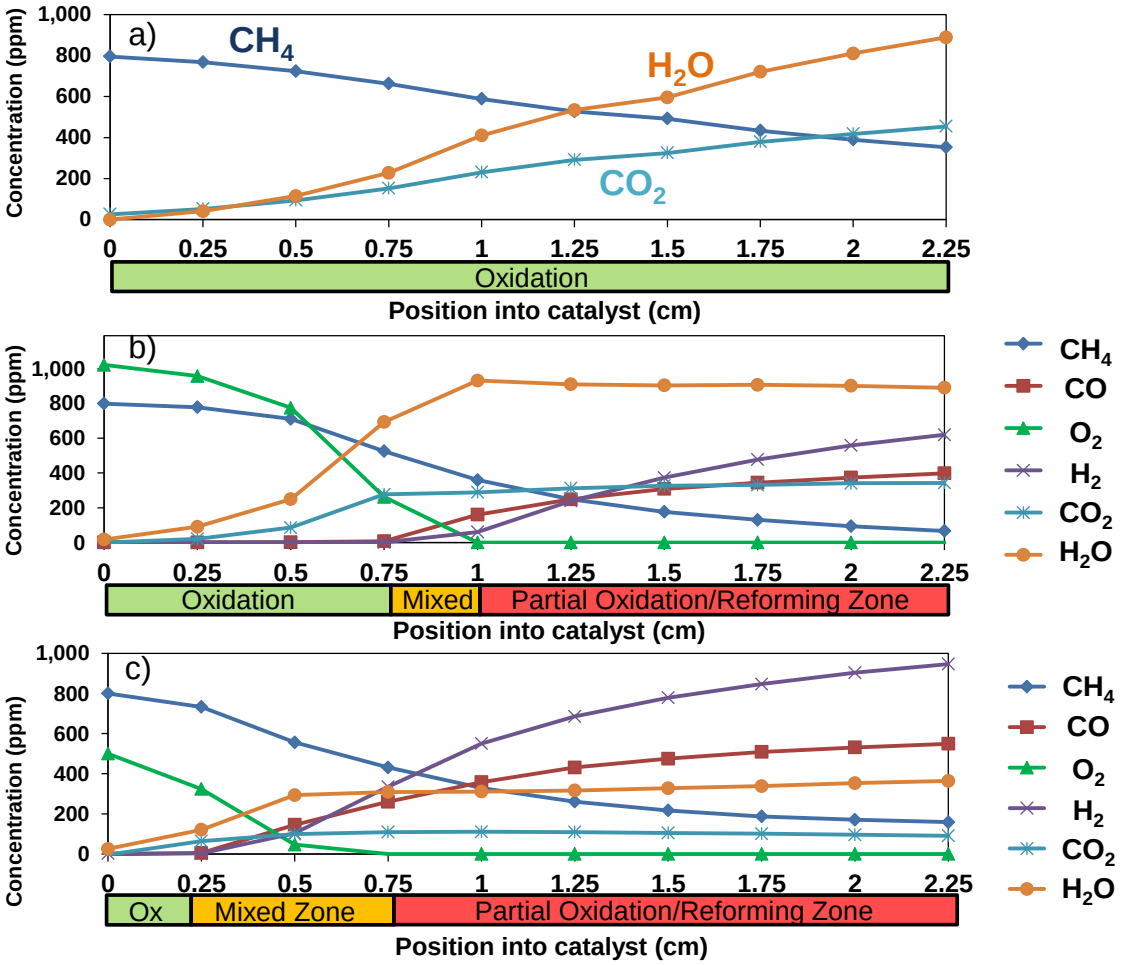

Figure 5.9 Spatially resolved concentration profiles during methane oxidation in (a) the lean regime (10% O_2), and rich regime (b: 0.1% O_2; c: 0.05% O_2). All other conditions were fixed (T_f = 538 °C, 800 ppm CH_4, GHSV=60,000 h^{-1})

The spatially resolved concentration measurements uncover more complex features under rich conditions. Figs. 5.9.b and 5.9.c show the reacting species concentrations for O_2 feed concentrations of 0.1% (1000 ppm) and 0.05% (500 ppm), respectively. These profiles were obtained when the catalyst was oxidizing methane near the maximum conversion, depicted as the 0.1% O_2, ~90% conversion and at 0.05% O_2, ~80% conversion in Fig. 5.2. Both profiles display similar features. In the front section of the reactor mainly complete oxidation of CH_4 occurs as evidenced by the co-production of H_2O and CO_2 in a ratio slightly exceeding 2; notable is the absence of H_2 and CO.

Moving further down the channel, the CH_4 and O_2 concentrations decrease more sharply with O_2 vanishing completely at the 1 cm mark for the 0.1% O_2 feed and at the 0.75 cm mark for 0.05% O_2 feed. Just upstream of the O_2 depletion point for the 0.05% O_2 feed both H_2 and CO are detected, albeit in rather small concentrations. Beyond the O_2 depletion point, the H_2 concentration in particular increases sharply. The appearance of CO and H_2 is evidence for a combination of methane steam reforming, methane partial oxidation, and WGS reactions. The zone between the front total oxidation zone (green) and the back reforming zone (red) is a transition zone wherein all of the chemistries may be occurring. We address the mechanism in more detail in the Discussion section.

Figs. 5.10.a-c shows the concentration profiles for a lower feed temperature (T_f = 482 °C) and fixed O_2 and CH_4 feed concentration of 0.05% and 800 ppm, respectively. The profiles were obtained along three different high conversion branches. The highest conversion branch in Fig. 5.10.a was obtained shortly after ignition from the lowest steady-state of the quenched catalyst, which had been exposed to an excess O_2 concentration. A complete oxidation zone is clearly seen in the 0.75 cm upstream section and a rather wide transition zone between 0.75 and 1.25 cm wherein complete oxidation to $CO_2 + H_2O$ and partial oxidation/reforming to $CO + H_2$ occur simultaneously. A partial oxidation/reforming zone is observed in the downstream "anaerobic" section beyond the O_2 depletion point. Note that while the gas phase O_2 has been depleted, a supply of oxygen from the catalyst enables continued oxidation. We return to this point later. The CO and H_2 continue to moderately increase while CH_4 continues to moderately decrease, while the CO_2 profile is flat. With time on-stream there is a notable decline in the CH_4 conversion and a corresponding qualitative change in the spatial profile (Figs. 5.10.b and

5.10.c). Collectively, these trends suggest an apparent transient decline in the integral methane conversion rate. While the complete oxidation of methane to CO_2 is sustained, the reforming activity to CO drops off, affecting the selectivity ratio. With longer time on-stream, reforming activity continues to fall, seen in Fig. 5.10.c, such that negligible CH_4 reacts after the first 1 cm. There appears to be two main distinguishing features of these lower temperature data compared to the higher temperature data shown in Fig. 5.9. The first feature is the more pronounced transition region wherein both complete and partial oxidation occurs; i.e. section in which the H_2 and O_2 are both nonzero. The second feature is the slower chemistry occurring in the anaerobic section. In fact, the lowest methane conversion branch (Fig. 5.10.c) shows virtually no methane or CO conversion beyond the O_2 depletion point. The reforming activity appeared to nearly halt, indicating that the rates of the reforming and WGS reactions are considerably slower at the lower temperature. The data also display a slight shift in the reaction front toward the inlet, with one possible explanation being the formation of a small amount of more active PdO near the catalyst inlet where gaseous oxygen is present.

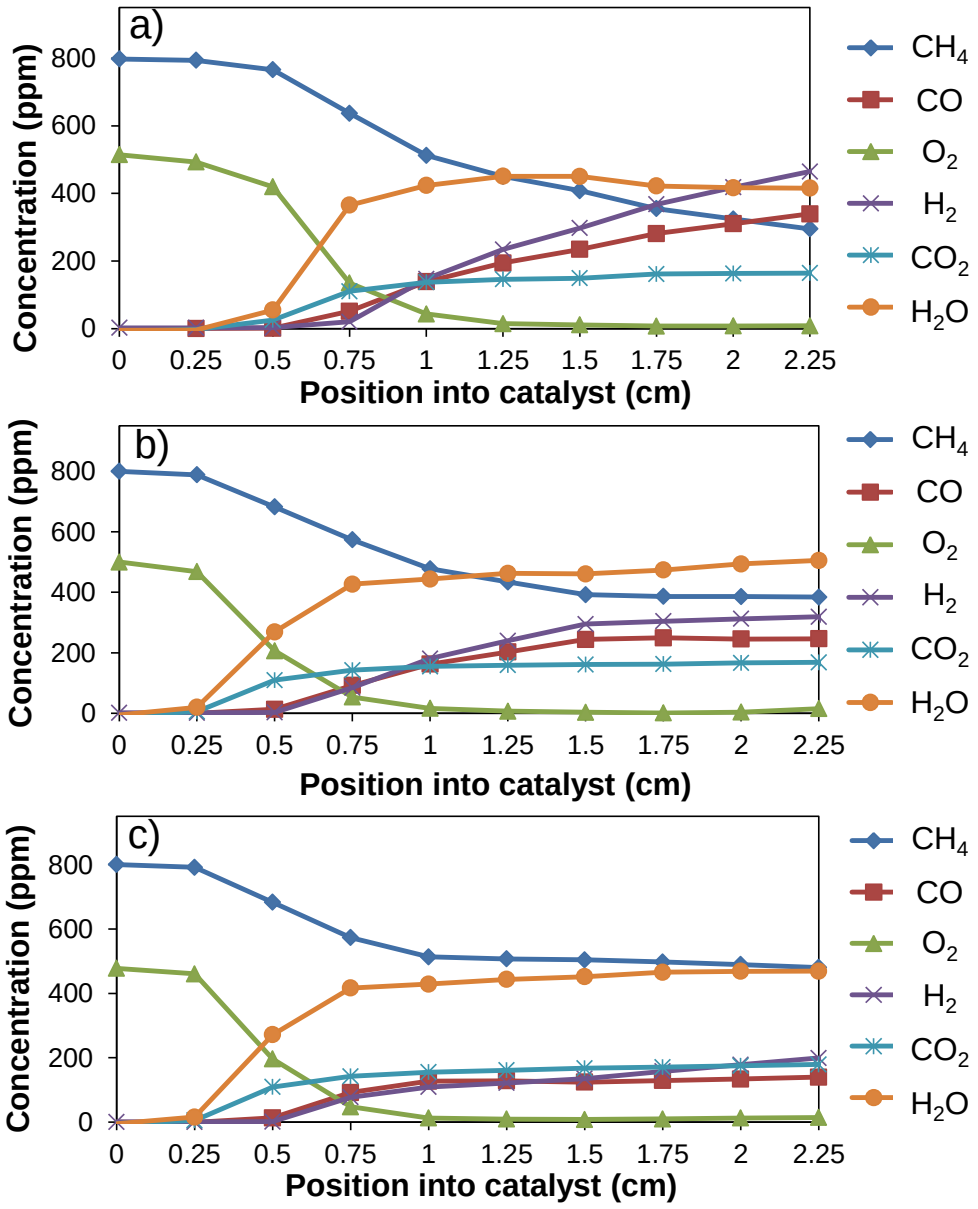

Figure 5.10 Spatially resolved concentration profiles at three different outlet conversion points for a fixed feed O_2 concentration of 0.05%. Final CH_4 conversion for a) 63%, b) 52%, c) 40% as shown in Fig. 5.7. All other conditions were fixed (T_f = 482 °C, 800 ppm CH_4, GHSV=60,000 h^{-1})

The relative reactivities of CO and CH_4 were evaluated in co-feed experiments. This comparison provides useful insight about the reaction mechanism and pathway evolution. Fig. 5.11 shows the effluent concentrations of CO and CH_4 when a feed containing 800 ppm CH_4, 4000 ppm CO and 0.2% O_2 (S_N = 0.56, a rich feed) was fed to

the Pt/Pd catalyst during a 10 °C/min temperature ramp. The catalyst was initially exposed to 450°C in 10% O_2 then cooled down before starting this experiment. The light-off and complete conversion of CO occurred in a temperature range (200-275 °C), well below the commencement of any measureable methane conversion. The complete conversion of CO should consume all of the O_2 since the feed ratio $CO/O_2 = 2$ is equal to the stoichiometric requirement. That methane reacts and even produces CO at higher temperature (~350 °C) could indicate that methane is competing with CO for O_2. But without spatially resolved data this is not conclusive. On the other hand, given the reactivity of CO at the lower temperature and SpaciMS measurements, its re-appearance at high temperature is clearly the result of anaerobic chemistry. This was confirmed in a subsequent experiment that is described next.

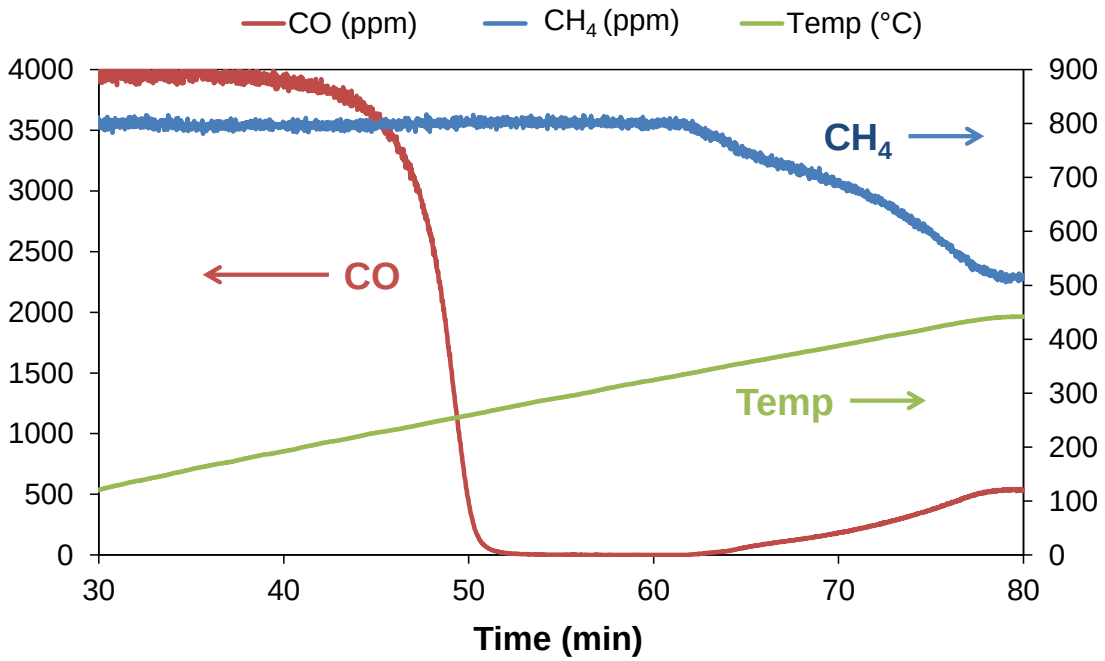

Figure 5.11 Temperature ramp with feed containing 800 ppm CH_4, 4000 ppm CO, and 0.2% O_2 (GHSV=60,000 h^{-1})

Utilizing the intra-channel concentration measurements enables the reaction progression to be tracked during a co-feed of CH_4, CO and O_2. Fig. 5.12 shows the results of an experiment in which the feed gas temperature was held at 538 °C and the feed concentrations were 800 ppm CH_4, 1400 ppm CO, and 0.2% O_2. The spatial profiles reveal that CO reacts first, consuming O_2 and generating CO_2. The CH_4 does not begin to react appreciably until the CO concentration is less than ~100 ppm. This occurs at rather low levels of gas phase O_2 (~700 ppm). Note that the O_2 feed concentration (0.2%) is above the value that led to methane conversion extinction (0.15%, Fig. 5.3), but the co-feed of CO enables the methane conversion light-off at higher O_2 feed concentration. The CO reacts with O_2 to produce CO_2 which decreases the gas phase O_2 concentration to a level in which methane ignition occurs. Continuing downstream where O_2 levels are further depleted, the partial oxidation and reforming reactions commence, generating H_2 and CO. At the point of O_2 depletion, anaerobic reforming and WGS chemistries take over. The intra-channel generation of CO essentially decreases the overall CO conversion when comparing the feed and effluent concentrations.

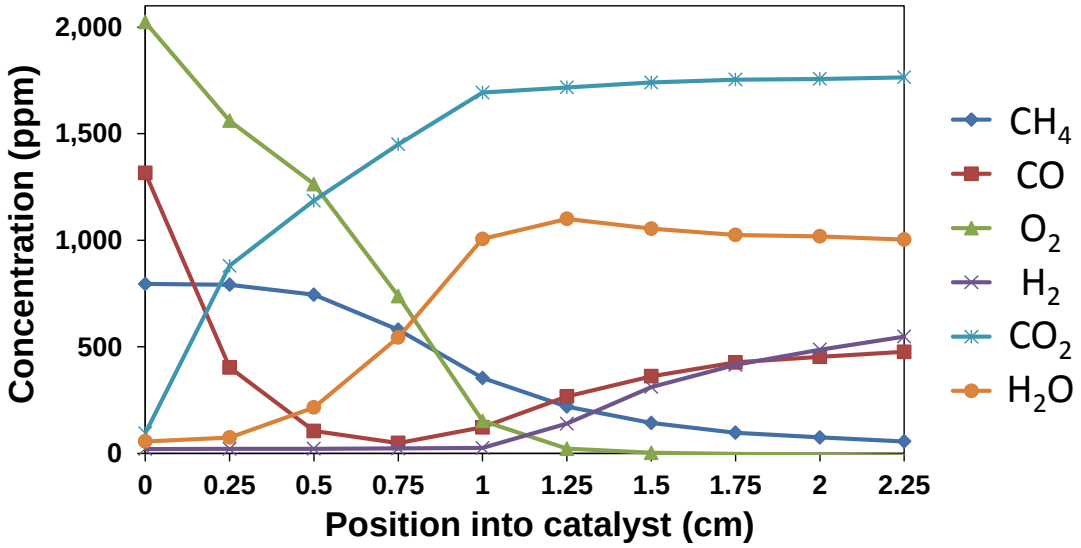

Figure 5.12 Spatially resolved concentration measurements at 538 °C with 1400 ppm CO and 0.02% O_2 (GHSV=60,000 h^{-1})

5.5 Discussion

The experiments revealed several notable features in the dependence of the methane conversion on O_2 concentration spanning rich and lean feed compositions, represented schematically in Fig. 5.13; these are:

Feature A: *Clockwise hysteresis loop comprising low and high steady-state conversion branches over a range of* p_{O_2}/p_{CH_4} *in the rich regime bounded below (above) by ignition (extinction) points;*

Feature B: *Existence of multiple transient high CH_4 conversion branches and single steady-state high CH_4 conversion branch in the rich regime;*

Feature C: *Metastable low CH_4 conversion branch in the lean regime;*

Feature D: *Nearly flat high CH_4 conversion branch in the lean regime.*

Oh et al. [27] reported a sharp transition at the stoichiometric point (part of Feature A) and a high methane conversion in the lean regime (Feature D) during methane oxidation on Pd/Al_2O_3 at high temperature. Interpretation of the steady-state, transient, and spatio-temporal features of methane oxidation on the Pt/Pd monolith catalyst should account for the literature-established differences in the catalytic activities of Pt and Pd. The TEM + EDS measurements indicated the presence of Pt-rich, Pd-rich, and PtPd (with Pt/Pd ~ 1) crystallites. We therefore interpret the main features based on the established understanding of the underlying catalytic chemistry and kinetics of Pt, Pd, and PdO. Our analysis is aided by the detailed insight afforded by the spatially resolved data.

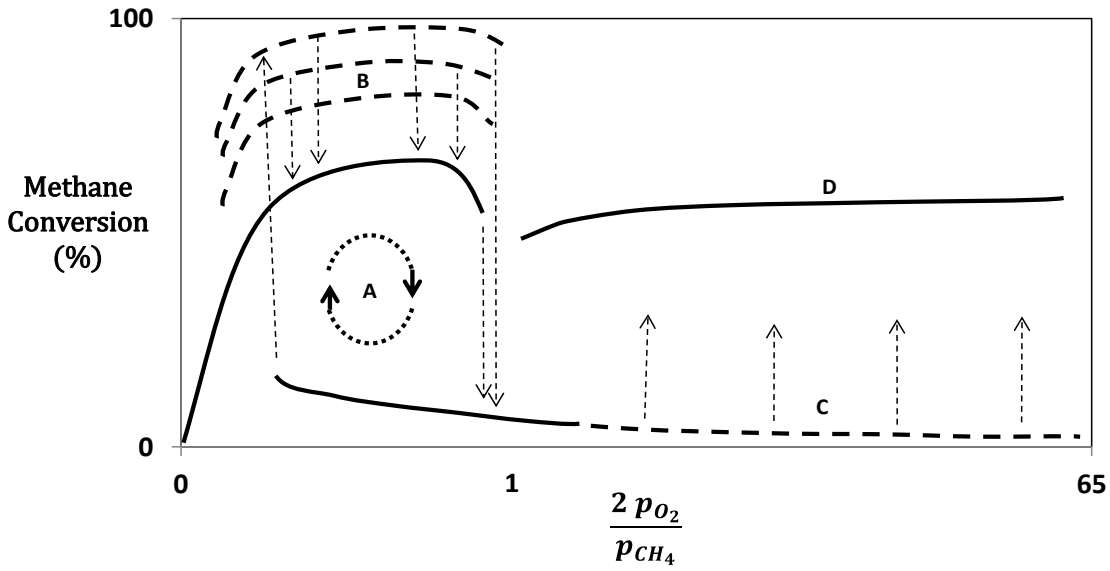

Figure 5.13 Schematic of the methane conversion dependence on O_2 feed concentration at elevated temperature

The clockwise hysteresis loop (**Feature A**, Fig. 5.13) reveals the existence of at least two distinct rate controlling regimes during oxygen-limited methane oxidation on Pt/Pd. Under reducing conditions there is a concomitant formation of metallic Pt, Pd, and/or Pt/Pd alloy phases. As indicated by the formation of H_2 and CO, several overall reactions occur along the high conversion branch (Figs. 5.9, 5.10, 5.12). The spatially resolved data indicate the complete consumption of O_2, which defines aerobic and anaerobic sections in the reactor (Fig. 5.9). In the aerobic section both complete and partial oxidation of methane occur, while methane steam reforming occurs in the anaerobic section, and the ubiquitous WGS reaction occurs throughout:

R1: $CH_4 + 2\,O_2 \rightarrow CO_2 + 2\,H_2O$ $\Delta H = -802$ kJ/mole;

R2: $CH_4 + 0.5\,O_2 \rightarrow CO + H_2$ $\Delta H = -36$ kJ/mole;

R3: $CH_4 + H_2O \leftrightarrow CO + 3\,H_2$ $\Delta H = +206$ kJ/mole;

R4: $CO + H_2O \leftrightarrow CO_2 + H_2$ $\Delta H = -41$ kJ/mole.

We expand on the occurrence of multiple reactions within the monolith in more detail below.

The sharp fall-off in the conversion that occurs at high temperature near the $S_N \sim 1$ stoichiometric point indicates inhibition of methane activation by oxygen. As mentioned, Oh et al. [27] reported in an earlier study a similar fall-off in conversion during methane oxidation on Pd/Al_2O_3 at 550 °C. Oxygen inhibition is known to occur on both Pt and Pd. Chin et al. [136] reported a single-valued, nonmonotonic rate dependence on O_2/CH_4 for methane oxidation on Pt/Al_2O_3 at 600 °C. For $O_2/CH_4 < 0.08$ the investigators showed that the rate is independent of excess methane and proportional to O_2 pressure; they further noted that CO was detected under O_2-starved conditions and that the CO/CO_2 ratio is dictated by the WGS equilibrium. For $O_2/CH_4 > 0.08$ the rate was shown to be second-order in methane and -1 order with respect to O_2. The negative-order dependence on O_2 partial pressure was attributed to site blocking by chemisorbed oxygen adatoms. In a similar study on Pd/Al_2O_3, Chin and Iglesia [131] reported a more gradual decline in the oxidation rate with O_2 partial pressure. The methane conversion (Fig. 5.2) shows a rather broad range of O_2 concentrations in which a high methane conversion exists. The broad range may indicate the contribution of both Pt and Pd metal sites on the alloyed particles of varying compositions.

The overlap of the high conversion, complete O_2 consumption state and the oxygen-inhibited, low conversion state, i.e. isothermal steady-state multiplicity, is the likely consequence of strongly nonlinear kinetics. Isothermal multiplicity has been reported for simpler reaction systems such as Pt-catalyzed CO oxidation, which has been attributed to the intrinsic kinetics or to coupling of the kinetics with transport; e.g., see

Harold and Garske [165, 166]. So-called isothermal rate multiplicity in which more than one steady-state rate exists at a given feed condition is the consequence of two or more controlling processes spanning a range of conditions. For example, the intrinsic rate of Pt-catalyzed CO oxidation is limited by CO adsorption at low CO/O_2 and by O_2 adsorption at high CO/O_2. In some reports the two regimes overlap in the form of a clockwise hysteresis loop [66, 67]. Eigenberger [167] showed for several generic reaction systems how the intrinsic kinetics can admit multiple solutions for some parameter values. Kevrekedis et al.[168] examined cases involving nonideal adsorption/desorption processes which leads additional nonlinearities. Harold and Garske showed for CO oxidation how the presence of external mass transport limitations can expand the multiplicity region [166] and that the extinction point locus occurs near the stoichiometric point. The situation in the current study is clearly more complicated for the methane oxidation reaction system given the occurrence of multiple reactions and at least two different types of metal sites. That said, there are clearly two regimes; a high conversion regime in which O_2 is depleted within the monolith and a low conversion regime in which the rate is inhibited by O_2. This is the essential ingredient for multiple states to exist. We conjecture that the overlap or steady-state multiplicity may be the result of contributions from Pd-rich and Pt-rich sites. That is Pd may sustain the high conversion state at higher O_2 concentrations because the inhibition is not as dramatic as on Pt, whereas the Pt may sustain the low conversion state at lower O_2 concentrations because of its more intense inhibition features.

The existence of multiple transient high conversion branches in the rich regime (**Feature B**, Fig. 5.13) is attributed to the redox behavior of the Pd-rich crystallites on the

bimetallic catalyst. The measured methane conversions exceeding the lower bound, stable steady-state branch (Fig. 5.4) are transient values that likely correspond to different extents of oxidation of the Pd catalyst. The conditions with which the Pd/Pt catalyst was initially exposed, a temperature of 550 °C and excess O_2, leads to a fraction of the Pd phase of the alloyed crystallites existing in oxidized form; i.e. PdO [19]. On the other hand, since PtO_2 is unstable at these elevated temperatures, Pt is present in metallic form [16, 169–171]. The extent of Pd oxidation depends on the exposure time, temperature, and gas phase O_2 concentration. The methane oxidation experiments involved a series of O_2 feed concentration increases and decreases that commenced at different initial conditions – or initial fractions of PdO. This resulted in what appeared to be an arbitrary number of high conversion branches within the rich regime (Fig. 5.3). For example, if the experiments started with a feed composition well into the lean regime ($S_N >> 1$), a subsequent decrease in the feed composition to a S_N value less than 1 resulted in methane conversion substantially higher than the eventual steady-state value. Since complete O_2 conversion is achieved for all of the branches including the (stable) steady-state branch, the CO/CO_2 selectivity ratio varies from branch to branch for a fixed O_2 feed concentration. With time-on-stream, the methane conversion slowly decreases while the CO/CO_2 selectivity ratio also decreases until the system reaches a steady-state. These observations point to the effect of a transient supply of oxygen from PdO, which is eventually completely consumed in the rich regime. Ultimately a steady-state level of Pd/PdO is established at a given O_2 feed concentration in the front section of the catalyst. This steady-state corresponds to the lowest of the high conversion branches.

The transient behavior of the catalyst depends its initial state and the path taken from that state. Consider that the bimetallic catalyst is initially in the high methane conversion state but still within the rich regime ($S_N < 1$). A decrease in the O_2 feed concentration results in the traversing of a distinct path in the methane conversion versus O_2 concentration plane. The decrease in O_2 concentration results in the Pd phase of the PtPd alloyed particles undergoing reduction which results in a higher fraction of metallic Pd. Upon a subsequent increase in the O_2 feed concentration, chemisorbed oxygen blocks active catalytic sites, but the Pd does not quickly form the more catalytically active PdO phase. This transient response is consistent with the observed hysteresis in the decomposition of PdO to metallic palladium and re-formation of PdO, as reported by others [133, 140–142]. The temperatures of thermal decomposition and re-oxidization of Pd are dependent on the gas composition (e.g., O_2 concentration), temperature, and Pt/Pd ratio [20]. Bell and coworkers [27, 28] showed that the Pd/PdO redox features proceed via a shrinking/expanding core mechanism.

Now consider starting with the catalyst in the low conversion state having just experienced extinction. This low conversion state persists well into the $S_N > 1$ feed composition regime. At a high enough O_2 feed concentration the low conversion state becomes unstable. That is, the low methane conversion branch in the lean regime (**Feature C**, Fig. 5.13) gradually shifts to higher conversion, taking several hours. For example, for a feed containing 10% O_2 the methane conversion increased from ~5 to ~40% in 300 minutes (Fig. 5.5). This transient is indicative of a slow modification of a relatively inactive PtPd catalyst inhibited by O adatoms (O-Pt/O-Pd) gradually transforming to a more active catalyst comprising PdO and still-poisoned Pt crystallites;

i.e., O-PtPdO This metastability of the low conversion branch in the lean regime is consistent with previous works, if one assumes that the Pd crystallites on the PtPd particles behave like their monometallic counterparts. For example, Burch and coworkers [172] measured the O_2 uptake on an initially-reduced Pd/Al_2O_3 catalyst exposed to a feed gas containing 9 torr O_2 and at 300 °C. They showed an initial rapid uptake of a single monolayer of O followed by a much slower uptake until an O/Pd ratio of ~4 at which point the methane conversion reached ~50%. Oh et al. [27] reported a low conversion branch beyond the stoichiometric point and noted "A transition from the low conversion branch in the net-oxidizing regime could not be achieved simply by varying the O_2 concentration in the feed." They speculated that an observed dependence on temperature in affecting the shift from the low conversion to high conversion branch could be related to bulk Pd oxide formation. Building on this explanation, we speculate that oxygen adatoms occupy surface sites and are effective in blocking methane adsorption as the O_2 concentration is increased, leading to the sharp drop in the conversion just into the rich regime. Then over time the oxygen-covered Pd crystallites transform to a more active PdO phase. The rate of the transformation process apparently increases at temperatures below ~500 °C. From this point alone, more research is needed to understand the catalyst composition and structural changes that affect the observed slow transition to a higher activity. In addition, this behavior raises some interesting issues about methane conversion during the anticipated transients encountered.

The fourth feature (**Feature D**, Fig. 5.13) in the methane conversion versus O_2 concentration plot is the existence of a stable methane conversion branch in the lean regime. In this regime the conversion is rather insensitive to the O_2 concentration and was

obtained either by starting the reaction at a high (> 10%) or low but still lean (~0.2%) O_2 concentration. This branch appears to be the classical lean methane oxidation on PdO, likely on the Pd-rich nanoparticles. Many previous studies have shown the very good activity of PdO and Pt/Pd catalysts, noting that for the latter PdO has been shown to be present as a separate phase (refer to Introduction). Moreover, the kinetics of lean methane oxidation in the 450 – 600 ^{o}C temperature range have been reported to be near unity order for methane and zero order for O_2 [135].

The SpaciMS measurements provide insight on the competing catalytic reactions. As mentioned earlier, there is evidence for complete oxidation, partial oxidation, steam reforming, and WGS chemistries. The complete oxidation of CH_4 is the lone overall reaction for a lean feed (reaction R1 above). Fig. 5.9.a shows this conventional consumption of CH_4 and formation of CO_2 and H_2O for a feed containing 800 ppm CH_4 and 10% O_2 (S_N = (2 x 100,000)/(4 x 800 + 0) = 62.5) and feed temperature of 538°C. Complete oxidation also occurs at the front part of the reactor when the feed is overall net rich (S_N < 1). For example, for the feed containing 800 ppm CH_4 and 500 ppm O_2 (Fig. 5.9.c) (S_N = (2 x 500)/(4 x 800 + 0) = 0.31) CO_2 and H_2O are the only products in the front 0.25 cm section of the reactor. Evidence for partial oxidation of methane is the presence of CO and/or H_2 (reaction R2). These products consistently appeared in the absence of gas phase O_2. For a net-reducing feed (S_N < 1) and a sufficiently high temperature, complete conversion of gas phase O_2 was observed. At the point in the reactor in which O_2 was depleted there was an emergence and increase in the incremental production of H_2 in particular and CO to a lesser extent. At high temperatures there was some evidence for methane steam reforming (R3) or WGS (R4) due to a reduction in the

H_2O concentration along the reactor length (see Fig. 5.9.b). The incremental production of H_2 and CO is not expected to be equal due to the H_2:CO = 3 ratio during partial oxidation as well as potential consumption of CO in favor of H_2 by the WGS reaction. It is noted that the extent of methane steam reforming was not that significant at the temperatures considered in this study. At the highest temperature (538 °C) and after steady-state (stored oxygen depletion) was established, only a few percent of CH_4 continued to react in the back section of the reactor in the absence of O_2.

The spatial profiles provide evidence for partial oxidation of methane by oxygen supplied from the catalyst. The three different methane conversion levels obtained at 482 °C correspond to different degrees of approach to steady-state (Fig. 5.10). The highest conversion state (Fig. 5.9.a) was obtained shortly after the catalyst had been exposed to an increased level of O_2. The methane profile clearly shows continued conversion even after depletion of gas phase O_2 within the reactor ($z > 1.25$ cm). The increasing CO profile in this region suggests sustained partial oxidation in the absence of O_2. In comparison, the profiles obtained after steady-state was reached (Fig. 5.10.c) show a much less pronounced methane consumption and CO production. This would seem to rule out any significant contribution of steam reforming at this temperature. Thus, the change in methane partial oxidation/reforming activity in the back portion of the catalyst is attributed to stored (bulk) oxygen which diffuses to the PdO phase of the bimetallic catalyst surface during rich conditions. As the stored oxygen becomes depleted over time, less methane reacts. This helps to explain why in the back portion of the catalyst the SpaciMS measurements show continued reaction of CH_4 to produce CO and H_2, even after all O_2 was consumed while not showing the corresponding consumption of H_2O. By

extinguishing the reaction with excess oxygen, the lattice oxygen is replenished and the maximum conversion may be restored upon light-off.

Further evidence for the enhancement of CH_4 conversion through reaction with stored oxygen can be gleaned from the oxygen material balance. In the experiment in which a constant O_2 concentration of 500 ppm (total of 1000 ppm oxygen atoms) was supplied three spatial profiles were obtained at different times on stream (Fig. 5.10). With increasing time-on-stream the total oxygen contained in the gaseous products decreased as evidenced by analysis of the CO, CO_2 and H_2O concentrations at the 2.25 cm position in the reactor. Shortly after oxygen replenishment (Fig. 5.10.a), the product stream contained 1083 ppm O (416 ppm H_2O + 339 ppm CO + 2 x 164 ppm CO_2), which is a level well above the feed value of 1000 ppm O. After some time (Fig. 10.c) the total oxygen contained in the products at the 2.25 cm position was 967 ppm O (469 ppm H_2O + 140 ppm CO + 2 x 179 ppm CO_2). Moreover, considerably less CO was formed, a more likely product from reaction between CH_4 and oxygen supplied from PdO. This analysis reinforces the existence of the direct partial oxidation of CH_4 by stored oxygen occurring in the back portion of the catalyst.

The spatial concentration profiles obtained with the co-feed of CO and CH_4 (Fig. 5.12) helps to decipher the methane oxidation mechanism. The conversion of 1400 ppm of CO is nearly complete in the front 0.75 cm section whereas the conversion of 800 ppm of CH_4 does not exceed 90% until the point of O_2 depletion at the 1.25 cm mark. The oxidation of CO in the front part of the catalyst serves to reduce the gas phase O_2 concentration enabling the light-off of methane oxidation. That the CO concentration does not completely vanish suggests CO and CH_4 oxidations have comparable rates at

higher temperature. Clearly, the temperature ramp experiment (Fig. 5.11) shows that CO oxidation is much faster than methane oxidation at lower temperature.

5.6 Conclusions

An experimental study of methane oxidation by $Pt/Pd/Al_2O_3$ washcoated monolith was carried out at oxygen feed concentrations spanning fuel lean to fuel rich. The effects of temperature and feed conditions on methane conversion and existence of axial zones in the catalyst have been systematically explored. A plot of the CH_4 conversion versus O_2/CH_4 feed ratio demonstrates features of methane oxidation that are both complex and interesting. The plot shows a clockwise hysteresis loop consisting of two stable steady-states of methane conversion. The high steady-state conversion branch is eclipsed by multiple higher methane conversion branches that are transient in nature. Within the rich regime, the methane conversion is to complete (CO_2, H_2O) and partial (CO, H_2) oxidation products with O_2 serving as the limiting reactant. The methane consumption observed under lean conditions is insensitive to the oxygen concentration and is classical lean methane oxidation on PdO.

An attempt is made to conjecture on the root causes of the various features of the conversion dependence on O_2 concentration, noting that the catalyst consists of a mixture of Pt and Pd. TEM-EDS results reveal a wide range of compositions for the PtPd alloyed particles, suggesting that the Pt, Pd, and PdO all contribute to the catalyst performance. We utilize conversion and selectivity measurements together with literature information on the behavior of Pt, Pd, and Pt/Pd catalysts during methane oxidation. The broad range of O_2 feed concentrations over which isothermal multiplicity occurs is likely the result of the nonlinear coupling between oxygen adsorption inhibition, PdO formation and

methane conversion. The formation of PdO appears responsible for the transient supra-steady-state conversion values that were observed when transitioning from lean to rich conditions. Finally, the slow increase in conversion that occurs in the lean regime is attributed to the modification of inactive metallic Pd crystallites into active PdO with Pt still-poisoned by oxygen.

Spatially resolved intrachannel concentration measurements show an intriguing interplay between multiple chemical reactions and their spatial evolution. The measurements show the existence of different zones based on the availability of oxygen in the gas phase or on the catalyst. The complete oxidation of methane occurs under both lean and rich conditions. During operation in the rich regime, a front oxidative zone and downstream partial oxidation/reforming zone co-exist. A middle mixed transition zone was also detected in which production of CO and H_2 occurs prior to complete consumption of the gas phase O_2. The partial oxidation of CH_4 during rich phase leads to our speculation that lattice oxygen diffuses to the catalyst surface thereby continuing the production of CO and H_2 + H_2O even after all of the available oxygen has been consumed without any corresponding consumption of H_2O. Measurements taken during different high conversion states in the rich regime corroborate the existence of the direct partial oxidation of CH_4 by stored oxygen that takes place in the rear section of the catalyst, as well as the subsequent decline in conversion and shift in selectivity as stored oxygen is depleted. Spatial concentration profiles obtained during a co-feed of CO and CH_4 reveal the fast oxidation of CO in the front portion of the catalyst, which reduces the gas phase O_2 concentration downstream and enabled the light-off of methane oxidation.

The findings from this study have two notable implications to the practice of methane emission control. First, the hysteresis and slow transients will have a definite impact on the emission control during the inherently transient vehicle operation, as the exhaust composition, temperature, and flow rate are all time dependent. The results show that the history of the catalyst will affect its performance, with the potential for dramatic conversion differences. This undoubtedly complicates the design of the catalytic converter and the associated control system to achieve a requisite level of emissions reduction over a drive cycle and underscores the need to develop a fundamental understanding of the kinetics and to capture that understanding in a predictive model. This is the subject of ongoing research. Second, the results indicate that high methane conversion can be achieved at sufficiently high temperature and relevant space velocities on a Pt/Pd monolith catalyst. The methane conversion is more effective and facile for a lean feed due to the higher activity of PdO. On the other hand, methane conversion can be achieved for a rich feed but the catalyst is very sensitive to the O_2 feed concentration and the byproducts include CO and H_2. While the formation of CO and H_2 is undesirable, they could be removed in a downstream converter using supplemental air.

6. Conclusions and Recommendations for Future Work

6.1 Conclusions

The behavior of Pt/Pd monolithic oxidation catalysts has been investigated for HC emission control through performance studies. This was accomplished through several related yet distinct studies.

6.2 Impact of zeolite beta

Experimental studies were carried out to investigate the effects of zeolite beta incorporation into the washcoat of Pt/Pd diesel oxidation catalysts on hydrocarbon storage, light-off temperatures, and conversion of stored HC to CO_2. Increasing the loading of zeolite subsequently increased the amount of dodecane storage capacity. The addition of zeolite did not have a notable effect on the light-off behavior for single component feeds of either CO or C12. Pre-storing HC had an inhibitory effect on the CO-light-off and the co-feed of C12 and CO increased the CO light-off temperatures even further, a trend that was consistent across all three catalysts studied.

During co-feed and pre-storage experiments the medium loading of zeolite displayed a beneficial effect on the CO light-off, compared to the baseline zeolite-free catalyst, which is attributed to the zeolite providing alternative storage sites for the HC and therefore reducing the inhibition on CO oxidation. The catalyst with high loading of zeolite, however, resulted in no significant change in CO light-off during co-feed experiments compared to the baseline zeolite-free catalyst, and in fact showed a negative effect on CO light-off during HC pre-storage experiments. This adverse effect of high zeolite loading is ascribed to the further increase in HC storage, which has an inhibitory effect on the CO light-off, overwhelming the beneficial effect of zeolite observed for the

medium loading zeolite. The catalyst with high zeolite loading did, however, demonstrate the largest percentage conversion of stored HC to CO_2 during the pre-store experiments.

These results illustrate that the zeolite loading level can be an important parameter to be mindful of during commercialization of real world applications. Demonstrated was a need to optimize the zeolite loading so that improvements in HC storage/conversion do not result in unacceptable light-off performance for other reactant species.

6.3 Propylene Oxidation and SpaciMS construction

The construction of a spatially resolved capillary-inlet sampling system for in-channel concentration measurements was successfully completed. A study of propylene oxidation was conducted, which included both light-off measurements by temperature ramp as well as steady-state measurements to acquire kinetic parameters. Using the Pt/Pd catalyst, the reaction was found to be self-inhibited with respect to propene concentration with a negative reaction order (~ -0.5). The newly built sampling technique was then utilized to measure the propene concentration through the length of the catalyst at various temperatures and propene feed concentrations. The negative-order reaction behavior was observed along the length of the monolith channel. Finally, a low-dimensional (LD) model was adapted in order to simulate the propylene effluent conversions and then modified without any further parameter fitting to produce the propene concentration profiles through the catalyst. The comparison between the model results and the experimentally obtained data fit relatively well and provides further evidence of the merits of the LD model and the veracity of the sampling method.

6.4 Complex feed mixtures over proprietary and model catalysts

Testing was performed for a third party participant, including a NSCR catalyst under near stoichiometric exhaust conditions and an oxidation catalyst in lean-burn exhaust conditions. For NSCR testing, the optimum O_2 feed to convert both NOx and HC/CO was dependent on temperature. Additionally, NOx was not observed to form across the third party catalysts at any condition, alleviating the client's concerns. The company was satisfied with the results and indicated being open to publication of the results. The TxCEF lab benefitted through increased knowledge, experience and financial support toward continuation of research in the facility laboratory.

The finding of increased CH_4 conversion at low O_2 feed concentrations is of particular interest, given the current trend of increased natural gas usage for vehicle applications. Since CH_4 is a greenhouse gas, there will be growing interest in catalytic aftertreatment of the CH_4. As displayed in the results of this study, CH_4 is particularly difficult to treat compared to other HCs. For these reasons, further research into the CH_4 conversion at low O_2 feed levels is warranted.

6.5 Methane oxidation spanning lean and rich conditions

An experimental study of methane oxidation by $Pt/Pd/Al_2O_3$ washcoated monolith was carried out at oxygen feed concentrations spanning fuel lean to fuel rich. The effects of temperature and feed conditions on methane conversion and existence of axial zones in the catalyst have been systematically explored. A plot of the CH_4 conversion versus O_2/CH_4 feed ratio demonstrates features of methane oxidation that are both complex and interesting. The plot shows a clockwise hysteresis loop consisting of two stable steady-states of methane conversion. The high steady-state conversion branch is eclipsed by

multiple higher methane conversion branches that are transient in nature. Within the rich regime, the methane conversion is to complete (CO_2, H_2O) and partial (CO, H_2) oxidation products with O_2 serving as the limiting reactant. The methane consumption observed under lean conditions is insensitive to the oxygen concentration and is classical lean methane oxidation on PdO.

Explanations as to the root causes of the various features of the conversion dependence on O_2 concentration are based on the catalyst consisting of a mixture of Pt and Pd. TEM-EDS results reveal a wide range of compositions for the PtPd alloyed particles, suggesting that the Pt, Pd, and PdO all contribute to the catalyst performance. Conversion and selectivity measurements were utilized together with literature information on the behavior of Pt, Pd, and Pt/Pd catalysts during methane oxidation. The broad range of O_2 feed concentrations over which isothermal multiplicity occurs is likely the result of the nonlinear coupling between oxygen adsorption inhibition, PdO formation and methane conversion. The formation of PdO appears responsible for the transient supra-steady-state conversion values that were observed when transitioning from lean to rich conditions. Finally, the slow increase in conversion that occurs in the lean regime is attributed to the modification of inactive metallic Pd crystallites into active PdO with Pt still-poisoned by oxygen.

Spatially resolved intrachannel concentration measurements show an intriguing interplay between multiple chemical reactions and their spatial evolution. The measurements show the existence of different zones based on the availability of oxygen in the gas phase or on the catalyst. The complete oxidation of methane occurs under both lean and rich conditions. During operation in the rich regime, a front oxidative zone and

downstream partial oxidation/reforming zone co-exist. A middle mixed transition zone was also detected in which production of CO and H_2 occurs prior to complete consumption of the gas phase O_2. The partial oxidation of CH_4 during rich phase leads to our speculation that lattice oxygen diffuses to the catalyst surface thereby continuing the production of CO and H_2 + H_2O even after all of the available oxygen has been consumed without any corresponding consumption of H_2O. Measurements taken during different high conversion states in the rich regime corroborate the existence of the direct partial oxidation of CH_4 by stored oxygen that takes place in the rear section of the catalyst, as well as the subsequent decline in conversion and shift in selectivity as stored oxygen is depleted. Spatial concentration profiles obtained during a co-feed of CO and CH_4 reveal the fast oxidation of CO in the front portion of the catalyst, which reduces the gas phase O_2 concentration downstream and enabled the light-off of methane oxidation.

The findings from this study have two notable implications to the practice of methane emission control. First, the hysteresis and slow transients will have a definite impact on the emission control during the inherently transient vehicle operation, as the exhaust composition, temperature, and flow rate are all time dependent. The results show that the history of the catalyst will affect its performance, with the potential for dramatic conversion differences. This undoubtedly complicates the design of the catalytic converter and the associated control system to achieve a requisite level of emissions reduction over a drive cycle and underscores the need to develop a fundamental understanding of the kinetics and to capture that understanding in a predictive model. This is the subject of ongoing research. Second, the results indicate that high methane conversion can be achieved at sufficiently high temperature and relevant space velocities

on a Pt/Pd monolith catalyst. The methane conversion is more effective and facile for a lean feed due to the higher activity of PdO. On the other hand, methane conversion can be achieved for a rich feed but the catalyst is very sensitive to the O_2 feed concentration and the byproducts include CO and H_2. While the formation of CO and H_2 is undesirable, they could be removed in a downstream converter using supplemental air.

6.6 Recommendations for Future Work

As part of this dissertation, the impact of zeolite loading level on the HC storage capacity and the light-off performance of monolithic Pt/Pd DOC catalysts were studied. In addition to the varied zeolite loadings, the series of BASF DOC catalysts prepared for this study also included variation in the precious metal content. This opens the door to further, complementary investigations on the impact of precious metal loading on light-off temperatures. This work could cover single component, co-feed, and pre-storage experiments as was done in the current study. This extension of the work would determine if similar trends hold true, namely that the moderate addition of zeolite enhances the oxidation activity during co-feed and pre-storage experiments but high zeolite loading negatively affects the light-off temperature. The efficient use of expensive precious metals is always a motivating factor, so a sensitivity study on the PGM loading can be beneficial.

The hydrocarbon trapping experiments utilized a feed gas stream lacking water (H_2O) and carbon dioxide (CO_2); however these components would be present in combustion exhaust. Real exhaust also contains a complicated mixture of hydrocarbons. Dodecane, a relatively lengthy alkane, was utilized here, but using an aromatic HC such as toluene would add breadth to the investigation on HC trapping. Further

experimentation including more complex reactant feeds may reveal additional contributing factors of importance to real world applications.

While Pt/Pd catalysts are used in commercial catalysts due to their synergistic effects, comparative experiments could potentially be run using Pt-only and/or Pd-only catalysts. This would perhaps yield a better understanding of which component is primarily contributing to certain observed behavior. This is especially pertinent to the methane oxidation study, as the Pd to PdO transformation is believed to play a major role in the trends reported here.

There are many avenues for further utilization of the capillary probe. One application in particular is the detection of the HC front as it moves through the catalyst sample during adsorption/storage and desorption/light-off experiments. This may result in a better fundamental understanding of the processes; however it would be a lengthy undertaking. The experiments are time consuming and there is only a single capillary probe necessitating repeating the experiment for each position, and likely repeats at each position.

Another potential future work is durability/aging tests on the catalysts. While the catalysts in this study were run at reaction conditions until repeatability was attained, this is considered "de-greening" of the catalyst. The conditions were not harsh enough or long enough to cause significant decreases in activity. Catalyst aging is likely to occur in the real world application, so a study involving aging the present catalysts can investigate if there is an impact of the zeolite on the Pt/Pd durability and also how the HC storage property is impacted with aging.

References

1. U.S. Energy Information Administration. (2015). "Monthly Energy Review March 2015". Retrieved from http://www.eia.gov/totalenergy/data/monthly/pdf/mer.pdf

2. US EPA. (2014). "Regulations and Standards: Light Duty". Retrieved from http://www.epa.gov/oms/climate/regs-light-duty.htm

3. US EPA. (2014). "Regulations and Standards: Heavy-Duty". Retrieved from http://www.epa.gov/oms/climate/regs-heavy-duty.htm

4. US EPA. (2014). "Emission Standards Reference Guide | US EPA". Retrieved July 16, 2014, from http://www.epa.gov/otaq/standards/

5. European Commission. (2015). "Transport and Environment". Retrieved from http://ec.europa.eu/environment/air/transport/road.htm

6. Russell, A., & Epling, W. S. (2011). Diesel Oxidation Catalysts. *Catalysis Reviews*, *53*(4), 337–423. doi:10.1080/01614940.2011.596429

7. Kozlov, A., Harris, T., & Salyards, C. (2010). Engine Test for DOC Quenching in DOC-DPF System for Non-Road Applications. *SAE Int. J. Fuels Lubr.*, *3*(1), 397–405.

8. Johnson, T. (2014). Vehicular Emissions in Review. *SAE Int. J. Engines*, *7*(3), 1207–1227.

9. Bohac, S. V, Assanis, D. N., & Holmes, H. L. S. (2004). Speciated hydrocarbon emissions and the associated local ozone production from an automotive gasoline engine. *International Journal of Engine Research (Professional Engineering Publishing)*, *5*, 53–70. Retrieved from 10.1243/146808704772914246

10. Yamamoto, S., Matsushita, K., Etoh, S., & Takaya, M. (2000). In-line Hydrocarbon (HC) Adsorber System for Reducing Cold-Start Emissions. *SAE Technical Paper*, *2000-01-08*.

11. Siegl, W. O., McCabe, R. W., Chun, W., Kaiser, E. W., Perry, J., Henig, Y. I., Trinkler, F. H., & Anderson, R. W. (1992). Speciated Hydrocarbon Emissions from the Combustion of Single Component Fuels. I. Effect of Fuel Structure. *Journal of the Air & Waste Management Association*, *42*(7), 912–921.

12. Atkinson, R. (2000). Atmospheric chemistry of VOCs and NOx. *Atmospheric Environment*, *34*(12-14), 2063–2101. doi:10.1016/S1352-2310(99)00460-4

13. Jacob, D. (2000). Heterogeneous chemistry and tropospheric ozone. *Atmospheric Environment*, *34*(12-14), 2131–2159. doi:10.1016/S1352-2310(99)00462-8

14. Boucher, O., Friedlingstein, P., Collins, B., & Shine, K. (2009). The indirect global warming potential and global temperature change potential due to methane oxidation. *Environmental Research Letters*, *4*, 044007. doi:10.1088/1748-9326/4/4/044007

15. Anderson, R. B., Stein, K. C., Feenan, J. J., & Hofer, L. J. E. (1961). Catalytic Oxidation of Methane. *Industrial & Engineering Chemistry*, *53*(10), 809–812. doi:10.1021/ie50622a024

16. Gelin, P., & Primet, M. (2002). Complete oxidation of methane at low temperature over noble metal based catalysts: a review. *Applied Catalysis B: Environmental*, *39*(1), 1–37. doi:http://dx.doi.org/10.1016/S0926-3373(02)00076-0

17. Lampert, J. K., Kazi, M. S., & Farrauto, R. J. (1997). Palladium catalyst performance for methane emissions abatement from lean burn natural gas vehicles. *Applied*

Catalysis B: Environmental, *14*(3-4), 211–223. doi:http://dx.doi.org/10.1016/S0926-3373(97)00024-6

18. Hicks, R. F., Qi, H., Young, M. L., & Lee, R. G. (1990). Effect of catalyst structure on methane oxidation over palladium on alumina. *Journal of Catalysis*, *122*(2), 295–306. doi:http://dx.doi.org/10.1016/0021-9517(90)90283-P
19. Ciuparu, D., Lyubovsky, M. R., Altman, E., Pfefferle, L. D., & Datye, A. (2002). Catalytic Combustion of Methane over Palladium-Based Catalysts. *Catalysis Reviews*, *44*(4), 593–649. doi:10.1081/cr-120015482
20. Castellazzi, P., Groppi, G., & Forzatti, P. (2010). Effect of Pt/Pd ratio on catalytic activity and redox behavior of bimetallic Pt-Pd/Al2O3 catalysts for CH4 combustion. *Applied Catalysis B: Environmental*, *95*(3-4), 303–311. doi:http://dx.doi.org/10.1016/j.apcatb.2010.01.008
21. McCarty, J. G. (1995). Kinetics of PdO combustion catalysis. *Catalysis Today*, *26*(3-4), 283–293. doi:http://dx.doi.org/10.1016/0920-5861(95)00150-7
22. Hicks, R. F., Qi, H., Young, M. L., & Lee, R. G. (1990). Structure sensitivity of methane oxidation over platinum and palladium. *Journal of Catalysis*, *122*(2), 280–294. doi:http://dx.doi.org/10.1016/0021-9517(90)90282-O
23. Baldwin, T. R., & Burch, R. (1990). Catalytic combustion of methane over supported palladium catalysts: I. Alumina supported catalysts. *Applied Catalysis*, *66*(1), 337–358. doi:http://dx.doi.org/10.1016/S0166-9834(00)81648-6
24. Baldwin, T. R., & Burch, R. (1990). Catalytic combustion of methane over supported palladium catalysts: II. Support and possible morphological effects. *Applied Catalysis*, *66*(1), 359–381. doi:http://dx.doi.org/10.1016/S0166-9834(00)81649-8

25. Briot, P., & Primet, M. (1991). Catalytic oxidation of methane over palladium supported on alumina : Effect of aging under reactants. *Applied Catalysis*, *68*(1), 301–314. doi:http://dx.doi.org/10.1016/S0166-9834(00)84110-X

26. Klingstedt, F., Neyestanaki, A. K., Byggningsbacka, R., Lindfors, L.-E., Lunden, M., Petersson, M., Tengstrom, P., Ollonqvist, T., & Vayrynen, J. (2001). Palladium based catalysts for exhaust aftertreatment of natural gas powered vehicles and biofuel combustion. *Applied Catalysis A: General*, *209*(1-2), 301–316. doi:http://dx.doi.org/10.1016/S0926-860X(00)00768-7

27. Oh, S. H., Mitchell, P. J., & Siewert, R. M. (1991). Methane oxidation over alumina-supported noble metal catalysts with and without cerium additives. *Journal of Catalysis*, *132*(2), 287–301. doi:http://dx.doi.org/10.1016/0021-9517(91)90149-X

28. Centi, G. (2001). Supported palladium catalysts in environmental catalytic technologies for gaseous emissions. *Journal of Molecular Catalysis A: Chemical*, *173*(1-2), 287–312. doi:http://dx.doi.org/10.1016/S1381-1169(01)00155-8

29. Narui, K., Yata, H., Furuta, K., Nishida, A., Kohtoku, Y., & Matsuzaki, T. (1999). Effects of addition of Pt to PdO/Al2O3 catalyst on catalytic activity for methane combustion and TEM observations of supported particles. *Applied Catalysis A: General*, *179*(1-2), 165–173. doi:http://dx.doi.org/10.1016/S0926-860X(98)00306-8

30. Kim, C. H. (2011). The Effect of Pt-Pd Ratio on Oxidation Catalysts Under Simulated Diesel Exhaust. *SAE International, SP-2318*, 9. doi:10.4271/2011-01-1134

31. Brunauer, S., Emmett, P. H., & Teller, E. (1938). Adsorption of Gases in Multimolecular Layers. *Journal of the American Chemical Society, 60*(2), 309–319. doi:10.1021/ja01269a023

32. International, Z. (2015). Zeolyst International: Zeolite Beta. Retrieved from http://www.zeolyst.com/our-products/standard-zeolite-powders/zeolite-beta.aspx

33. Joshi, S. Y., Ren, Y., Harold, M. P., & Balakotaiah, V. (2011). Experimental and Theoretical Investigation of Controlling Regimes during Lean Oxidation of Methane and Propylene on Pt/Al2O3 Monolithic Reactors. *Industrial & Engineering Chemistry Research*. doi:10.1021/ie201653e

34. Bugosh, G. S., Easterling, V. G., Rusakova, I. A., & Harold, M. P. (2014). Anomalous Steady-State and Spatio-Temporal Features of Methane Oxidation on Pt/Pd/Al2O3 Monolith Spanning Lean and Rich Conditions. *Applied Catalysis B: Environmental*. doi:10.1016/j.apcatb.2014.09.058

35. Tourtellotte, J., Negra, J., Warshaw, A., & Villiers-Fisher, J. (1972). Engine Exhaust Emission Control System. (U. S. P. Office, Ed.). US: U.S.

36. Otto, K., Montreuil, C. N., Todor, O., McCabe, R. W., & Gandhi, H. S. (1991). Adsorption of hydrocarbons and other exhaust components on silicalite. *Industrial & Engineering Chemistry Research*, *30*(10), 2333–2340. doi:10.1021/ie00058a013

37. Minami, T., & Nagase, T. (1992). Exhaust Gas Purification Device in Variable Combinations of Absorbent and Catalyst According to Gas Temperature. U.S.

38. Heimrich, M., Smith, L., & Kitowski, J. (1992). Cold-Start Hydrocarbon Collection for Advanced Exhaust Emission Control. *SAE Technical Paper*, *920847*.

39. Engler, B. H., Lindner, D., Lox, E. S., & Muller, W. (1993). Reduction of Exhaust Gas Emissions by Using Hydrocarbon Adsorber Systems. *SAE International*, (SAE 930738). doi:10.4271/930738

40. Ballinger, T. H., Manning, W. A., & Lafyatis, D. S. (1997). Hydrocarbon Trap Technology for the Reduction of Cold-Start Hydrocarbon Emissions. *SAE Technical Paper*, *970741*.

41. Lafyatis, D. S., Ballinger, T. H., Lammey, G., & Frost, J. C. (1998). Ambient Temperature Light-off Aftertreatment System for Meeting ULEV Emission Standards. *SAE Technical Paper*, *980421*.

42. Lafyatis, D. S., Ansell, G. P., Bennett, S. C., Frost, J. C., Millington, P. J., Rajaram, R. R., Walker, A. P., & Ballinger, T. H. (1998). Ambient temperature light-off for automobile emission control. *Applied Catalysis B: Environmental*, *18*(1-2), 123–135.

43. Kollman, K., Abthoff, J., & Zahn, W. (1994). Concepts for Ultra Low Emission Vehicles. *SAE Technical Paper*, *940469*.

44. Burk, P. L., Hochmuth, J. K., Anderson, D. R., Sung, S., Tauster, S. J., Tolentino, C. O., Rogalo, J., Miles, G., Niejako, M., Punke, A., & Dahle, U. (1995). Cold Start Hydrocarbon Emissions Control. *SAE Technical Paper*, *950410*.

45. Patil, M., Hertl, W., Williams, J., & Nagel, J. (1996). In-Line Hydrocarbon Adsorber System for ULEV. *SAE Technical Paper*, *960348*.

46. Noda, N., Takahashi, A., & Mizuno, H. (1997). In-line Hydrocarbon (HC) Adsorber System for Cold Start Emissions. *SAE Technical Paper*, *970266*.

47. Buhrmaster, C. L., Locker, R. J., Patil, M., Nagel, J., & Socha, L. (1997). Evaluation of In-line Adsorber Technology. *SAE Technical Paper, 970267*.

48. Silver, R., Dou, D., Kirby, C., Richmond, R., Balland, J., & Dunne, S. (1997). A Durable In-Line Hydrocarbon Adsorber for Reduced Cold Start Exhaust Emissions. *SAE Technical Paper*, *972843*.

49. Abthoff, J., Kemmler, R., Klein, H., Matt, M., Robota, H., Wolsing, W., Wiehl, J., & Dunne, S. (1998). Application of In-Line Hydrocarbon Adsorber Systems. *SAE Technical Paper*, *980422*.

50. Kaiser, E. W., Siegl, W. O., Henig, Y. I., Anderson, R. W., & Trinker, F. H. (1991). Effect of fuel structure on emissions from a spark-ignited engine. *Environmental Science & Technology*, *25*(12), 2005–2012. doi:10.1021/es00024a004

51. Nishizawa, K., Mitsuichi, S., Mori, K., & Yamamoto, S. (2001). Development of Second Generation of Gasoline P-ZEV Technology. *SAE Technical Paper, 2001-01-13*.

52. Kamijo, M., Kamikubo, M., Akama, H., & Matsushita, K. (2001). Study of an oxidation catalyst system for diesel emission control utilizing HC adsorption. *JSAE Review*, *22*(277-280).

53. Hiramoto, Y., Takaya, M., Yamamoto, S., & Okada, A. (2003). Development of a New HC-Adsorption Three-Way Catalyst System for Partial-ZEV Performance. *SAE Technical Paper*, *2003-01-18*.

54. Mukai, K., Kanesaka, H., Akama, H., & Ikeda, T. (2004). Adsorption and Desorption Characteristics of the Adsorber to Control the HC Emission from a Gasoline Engine. *SAE Technical Paper*, *2004-01-29*.

55. Goralski, C., Chanko, T., Lupescu, J., & Ganti, G. (2000). Experimental and Modeling Investigation of Catalyzed Hydrocarbon Trap Performance. *SAE Technical Paper, 2000-01-06*.

56. Lupescu, J., Chanko, T., Richert, J., & Mauti, A. (2009). The effect of spark timing on engine-out hydrocarbon speciation and hydrocarbon trap performance. *SAE Technical Paper, 2009-01-10*.

57. Kanazawa, T., & Sakurai, K. (2001). Development of the Automotive Exhaust Hydrocarbon Adsorbent. *SAE Technical Paper, 2001-01-06*.

58. Kanazawa, T. (2004). Development of hydrocarbon adsorbents, oxygen storage materials for three-way catalysts and NOx storage-reduction catalyst. *Catalysis Today*, *96*(3), 171–177.

59. Kidokoro, T., Hoshi, K., Hiraku, K., Satoya, K., Watanabe, T., Fujiwara, T., & Suzuki, H. (2003). Development of PZEV Exhaust Emission Control System. *SAE Technical Paper, 2003-01-08*.

60. Liu, X., Lampert, J. K., Arendarskiia, D. A., & Farrauto, R. J. (2001). FT-IR spectroscopic studies of hydrocarbon trapping in Ag+-ZSM-5 for gasoline engines under cold-start conditions. *Applied Catalysis B: Environmental*, *35*(2), 125–136.

61. Ballinger, T. H., & Andersen, P. J. (2002). Vehicle Comparison of Advanced Three-Way Catalysts and Hydrocarbon Trap Catalysts. *SAE Technical Paper, 2002-01-07*.

62. Higashiyama, K., Nagayama, T., Nagano, M., & Nakagawa, S. (2003). A catalyzed Hydrocarbon Trap Using Metal-impregnated Zeolite for SULEV Systems. *SAE Technical Paper, 2003-01-08*.

63. Nakagawa, S., Minowa, T., Katogi, K., Higashiyama, K., Nagano, M., & Hamada, I. (2003). A New Catalyzed Hydrocarbon Trap Control System for ULEV/SULEV Standard. *SAE Technical Paper*, *2003-01-05*.

64. Yamazaki, H., Endo, T., & Ueno, M. (2004). Research on HC Adsorption Emission System. *SAE International*, *2004-01-12*.

65. Li, H. X., Donohue, J. M., Chrmier, W. E., & Chu, Y. F. (2005). Application of zeolites as hydrocarbon traps in automotive emission controls. In *Studies in Surface Science and Catalysis* (Vol. Volume 158, pp. 1375–1382). Elsevier.

66. Choi, S., Youn, Y. K., In, C., & Yeo, G. K. (2006). Development of Exhaust System for Post-SULEV. *SAE Technical Paper*, *2006-01-08*.

67. Corbo, P., Migliardini, F., Aiello, R., Crea, F., Caputo, D., Colella, C., & Lucolano, F. (2001). Abatement of automotive cold start hydrocarbon emissions. *SAE Technical Paper*, *2001-01-06*.

68. Seo, H.-K., Oh, J.-W., Lee, S.-C., Sung, J.-Y., & Choung, S.-J. (2001). Adsorption characteristics of HCA(Hydrocarbon Adsorber) catalysts for hydrocarbon and NOx removals under cold-start engine conditions. *Korean Journal of Chemical Engineering*, *18*(5), 698–703. doi:10.1007/bf02706389

69. Czaplewski, K. F., Reitz, T. L., Kim, Y. J., & Snurr, R. Q. (2002). One-dimensional zeolites as hydrocarbon traps. *Microporous and Mesoporous Materials*, *56*(1), 55–64.

70. Burke, N. R., Trimm, D. L., & Howe, R. F. (2003). The effect of silica:alumina ratio and hydrothermal ageing on the adsorption characteristics of BEA zeolites for cold start emission control. *Applied Catalysis B: Environmental*, *46*(1), 97–104.

Retrieved from http://www.sciencedirect.com/science/article/pii/S0926337303001814

71. Elangovan, S. P., Ogura, M., Davis, M. E., & Okubo, T. (2004). SSZ-33: A Promising Material for Use as a Hydrocarbon Trap. *The Journal of Physical Chemistry B*, *108*(35), 13059–13061. doi:10.1021/jp047394r

72. Kim, D. J., Kim, J. M., Yie, J. E., Seo, S. G., & Kim, S.-C. (2004). Adsorption and conversion of various hydrocarbons on monolithic hydrocarbon adsorber. *Journal of Colloid and Interface Science*, *274*(2), 538–542. Retrieved from http://www.sciencedirect.com/science/article/pii/S0021979704000165

73. Elangovan, S. P., Ogura, M., Zhang, Y., Chino, N., & Okubo, T. (2005). Silicoaluminophosphate molecular sieves as a hydrocarbon trap. *Applied Catalysis B: Environmental*, *57*(1), 31–36. Retrieved from http://www.sciencedirect.com/science/article/pii/S0926337304006010

74. Kryl, D., Koci, P., Kubicek, M., Marek, M., Maunula, T., & Harkonen, M. (2005). Catalytic Converters for Automobile Diesel Engines with Adsorption of Hydrocarbons on Zeolites. *Industrial & Engineering Chemistry Research*, *44*(25), 9524–9534. doi:10.1021/ie050249v

75. Elangovan, S. P., Ogura, M., Ernst, S., Hartmann, M., Tontisirin, S., Davis, M. E., & Okubo, T. (2006). A comparative study of zeolites SSZ-33 and MCM-68 for hydrocarbon trap applications. *Microporous and Mesoporous Materials*, *96*, 210–215. Retrieved from http://www.sciencedirect.com/science/article/pii/S1387181106002563

76. Park, J.-H., Park, S. J., Nam, I.-S., Yeo, G. K., Kil, J. K., & Youn, Y. K. (2007). A fast and quantitative assay for developing zeolite-type hydrocarbon trap catalyst. *Microporous and Mesoporous Materials*, *101*, 264–270.

77. Iliyas, A., Zahedi-Niaki, M. H., Eic, M., & Kaliaguine, S. (2007). Control of hydrocabon cold-start emissions: A search for potential adsorbents. *Microporous and Mesoporous Materials*, *102*, 171–177.

78. Zhang, Y., Su, Q., Wang, Z., Yang, Y., Xin, Y., Han, D., Yang, X., Wang, H., Gao, X., & Zhang, Z. (2008). Synthesis and Toluene Adsorption/Desorption Property of Beta Zeolite Coated on Cordierite Honeycomb by an In Situ Crystallization Method. *Chemical Engineering & Technology*, *31*(12), 1856–1862. doi:10.1002/ceat.200800260

79. Inoue, K., & Mitsuishi, S. (2009). Development of Atmospheric Air-level Emission Vehicle Technology for Gasoline Engines. *SAE International*, (2009-01-1076), 53–60.

80. Raux, S., Frobert, A., & Jeudy, E. (2009). Low Temperature Activity of Euro4 Diesel Oxidation Catalysts: Comprehensive Material Analyses and Experimental Evaluation of a Representative Panel. *Topics in Catalysis*, *52*(13), 1903–1908. doi:10.1007/s11244-009-9367-1

81. Luo, J.-Y., Yezerets, A., Henry, C., Hess, H., Kamasamudram, K., Chen, H.-Y., & Epling, W. S. (2012). Hydrocarbon Poisoning of Cu-Zeolite SCR Catalysts. *SAE Technical Paper*, *2012-01-10*.

82. Kumar, A., Kamasamudram, K., & Yezerets, A. (2013). Hydrocarbon Storage on Small-Pore Cu-Zeolite SCR Catalyst. *SAE Technical Paper*, *2013-01-05*. doi:10.4271/2013-01-0508

83. López, J. M., Navarro, M. V, García, T., Murillo, R., Mastral, A. M., Varela-Gandía, F. J., Lozano-Castelló, D., Bueno-López, A., & Cazorla-Amorós, D. (2010). Screening of different zeolites and silicoaluminophosphates for the retention of propene under cold start conditions. *Microporous and Mesoporous Materials*, *130*(1-3), 239–247. Retrieved from http://www.sciencedirect.com/science/article/B6TH4-4XPP13T-1/2/4df72610e87bbe62d3b180a9fc795899

84. Global Polypropylene Market Capacity to see 5.8% CAGR. (2014). *PR Newswire*. Retrieved January 21, 2015, from http://finance.yahoo.com/news/global-polypropylene-market-capacity-see-170000813.html

85. Muncrief, R. L., Kabin, K. S., & Harold, M. P. (2004). NOx Storage and Reduction with Propylene on Pt/BaO/Alumina. *AIChE Journal*, *50*(10), 2526–2540.

86. Perng, C. C. Y., Easterling, V. G., & Harold, M. P. (2014). Fast lean-rich cycling for enhanced NOx conversion on storage and reduction catalysts. *Catalysis Today*, *231*, 125–134. doi:10.1016/j.cattod.2014.01.026

87. Raj, R., Harold, M. P., & Balakotaiah, V. (2013). NO Inhibition Effects During Oxidation of Propylene on Cu-Chabazite Catalyst: A Kinetic and Mechanistic Study. *Industrial & Engineering Chemistry Research*, *52*(44), 15455–15465. doi:10.1021/ie4009343

88. Raj, R., Harold, M. P., & Balakotaiah, V. (2014). Kinetic modeling of NO selective reduction with C3H6 over Cu-SSZ13 monolithic catalyst. *Chemical Engineering Journal*, *254*, 452–462. doi:10.1016/j.cej.2014.05.105

89. Zheng, Y., Li, M., Harold, M. P., & Luss, D. (2015). Enhanced Low-Temperature NOx Conversion by High-Frequency Hydrocarbon Pulsing on a Dual Layer LNT-SCR Catalyst. *SAE Technical Paper*, (2015-01-0984).

90. Zheng, Y., Luss, D., & Harold, M. (2014). Optimization of LNT-SCR Dual-Layer Catalysts for Diesel NOx Emission Control. *SAE Technical Paper*, (2014-01-1544).

91. Joshi, S. Y., Harold, M. P., & Balakotaiah, V. (2009). Low-dimensional models for real time simulations of catalytic monoliths. *AIChE Journal*, *55*(7), 1771–1783. doi:10.1002/aic.11794

92. Joshi, S. Y., Harold, M. P., & Balakotaiah, V. (2010). Overall mass transfer coefficients and controlling regimes in catalytic monoliths. *Chemical Engineering Science*, *65*(5), 1729–1747. Retrieved from http://www.sciencedirect.com/science/article/pii/S0009250909008227

93. Joshi, S. Y., Ren, Y., Harold, M. P., & Balakotaiah, V. (2011). Determination of kinetics and controlling regimes for H2 oxidation on Pt/Al2O3 monolithic catalyst using high space velocity experiments. *Applied Catalysis B: Environmental*, *102*(3-4), 484–495. Retrieved from http://www.sciencedirect.com/science/article/B6TF6-51S25DJ-2/2/e373f8c980438e3d526e0194a1c4f4d1

94. Partridge, W. P., Storey, J., Lewis, S., Smithwick, R., Devault, G., & Cunningham, M. (2000). Time-Resolved Measurements of Emission Transients By Mass Spectrometry. *SAE Technical Paper*, *2000-01-29*. doi:10.4271/2000-01-2952

95. West, B., Huff, S., Parks, J., Lewis, S., Choi, J.-S., Partridge, W. P., & Storey, J. (2004). Assessing Reductant Chemistry During In-Cylinder Regeneration of Diesel Lean NOx Traps. *SAE Technical Paper, 2004-01-30*. doi:10.4271/2004-01-3023

96. Clayton, R. D., Harold, M. P., & Balakotaiah, V. (2008). NOx storage and reduction with H2 on Pt/BaO/Al2O3 monolith: Spatio-temporal resolution of product distribution. *Applied Catalysis B: Environmental*, *84*(3-4), 616–630. doi:10.1016/j.apcatb.2008.05.018

97. Hettel, M., Diehm, C., Torkashvand, B., & Deutschmann, O. (2013). Critical evaluation of in situ probe techniques for catalytic honeycomb monoliths. *Catalysis Today*, *216*, 2–10. doi:10.1016/j.cattod.2013.05.005

98. Goguet, A., Partridge, W. P., Aiouche, F., Hardacre, C., Morgan, K., Stere, C., & Sá, J. (2014). Comment on "The Critical evaluation of in situ probe techniques for catalytic honeycomb monoliths" by Hettel, Diehm, Torkashand, & Deutschmann. *Catalysis Today*, *236*, 206–208. doi:10.1016/j.cattod.2014.02.034

99. Hettel, M., Diehm, C., & Deutschmann, O. (2014). Answer to the Comment from Goguet, Partridge, Aiouche, Hardacre, Morgan, Stere, & Sá to the paper "The Critical evaluation of in situ probe techniques for catalytic honeycomb monoliths" by Hettel, Diehm, Torkashand, & Deutschmann. *Catalysis Today*, *236*, 209–213. doi:10.1016/j.cattod.2014.02.033

100. Horn, R., Degenstein, N., Williams, K., & Schmidt, L. (2006). Spatial and temporal profiles in millisecond partial oxidation processes. *Catalysis Letters*, *110*(3-4), 169–178. doi:10.1007/s10562-006-0117-8

101. Degenstein, N. J. (2007). *Spatially Resolved Species and Temperature Profiles in the Catalytic Partial Oxidation of Methane and Ethane*. University of Minnesota.

102. Donazzi, A., Michael, B. C., & Schmidt, L. D. (2008). Chemical and geometric effects of Ce and washcoat addition on catalytic partial oxidation of CH4 on Rh probed by spatially resolved measurements. *Journal of Catalysis*, *260*(2), 270–275. Retrieved from http://www.sciencedirect.com/science/article/pii/S002195170800376X

103. Michael, B. C., Donazzi, A., & Schmidt, L. D. (2009). Effects of H2O and CO2 addition in catalytic partial oxidation of methane on Rh. *Journal of Catalysis*, *265*(1), 117–129. Retrieved from http://www.sciencedirect.com/science/article/pii/S0021951709001286

104. Luo, J.-Y., Oh, H., Henry, C., & Epling, W. (2012). Effect of C3H6 on selective catalytic reduction of NOx by NH3 over a Cu/zeolite catalyst: A mechanistic study. *Applied Catalysis B: Environmental*, *123-124*(0), 296–305. doi:http://dx.doi.org/10.1016/j.apcatb.2012.04.038

105. Luo, J.-Y., Hou, X., Wijayakoon, P., Schmieg, S. J., Li, W., & Epling, W. S. (2011). Spatially resolving SCR reactions over a Fe/zeolite catalyst. *Applied Catalysis B: Environmental*, *102*(1-2), 110–119. Retrieved from http://www.sciencedirect.com/science/article/pii/S0926337310005199

106. Hiden Analytical. (2015). spatially resolved capillary inlet MS. Retrieved from http://www.hidenanalytical.com/en/49-products/catalyst-characterisation/73-spacims-spatially-resolved-capillary-inlet-ms

107. Maupin, I., Mijoin, J., Barbier Jr, J., Bion, N., Belin, T., & Magnoux, P. (2011). Improved oxygen storage capacity on CeO2/zeolite hybrid catalysts. Application to VOCs catalytic combustion. *Catalysis Today*, *176*(1), 103–109. Retrieved from http://www.sciencedirect.com/science/article/pii/S0920586111000976

108. Balakotaiah, V., & West, D. H. (2002). Shape normalization and analysis of the mass transfer controlled regime in catalytic monoliths. *Chemical Engineering Science*, *57*(8), 1269–1286. doi:10.1016/S0009-2509(02)00059-3

109. Pratt, A. S., & Cairns, J. A. (1977). Noble Metal Catalysts on Metallic Substrates: A New Generation of Cellular Monoliths for Emission Control. *Platinum Metals Review*, *21*(3), 74–83.

110. Avila, P., Montes, M., & Miró, E. E. (2005). Monolithic reactors for environmental applications: A review on preparation technologies. *Chemical Engineering Journal*, *109*(1-3), 11–36. Retrieved from http://www.sciencedirect.com/science/article/B6TFJ-4FWSDVB-1/2/9edf3a2e4b519ef5e59ab97a7e515b46

111. Barbero, B. P., Costa-Almeida, L., Sanz, O., Morales, M. R., Cadus, L. E., & Montes, M. (2008). Washcoating of metallic monoliths with a MnCu catalyst for catalytic combustion of volatile organic compounds. *Chemical Engineering Journal*, *139*(2), 430–435. doi:10.1016/j.cej.2007.12.033

112. Valentini, M., Groppi, G., Cristiani, C., Levi, M., Tronconi, E., & Forzatti, P. (2001). The deposition of γ-Al2O3 layers on ceramic and metallic supports for the preparation of structured catalysts. *Catalysis Today*, *69*(1-4), 307–314. doi:10.1016/S0920-5861(01)00383-2

113. Hensel, C., Konieczny, R., & Brück, R. (2000). Recycling Technology for Metallic Substrates: A Closed Cycle. *SAE International*, (2000-01-0596). doi:10.4271/2000-01-0596

114. Kakaee, A.-H., Paykani, A., & Ghajar, M. (2014). The influence of fuel composition on the combustion and emission characteristics of natural gas fueled engines. *Renewable and Sustainable Energy Reviews*, *38*, 64–78.

115. McTaggart-Cowan, G. P., Rogak, S. N., Munshi, S. R., Hill, P. G., & Bushe, W. K. (2010). The influence of fuel compositions on a heavy-duty, natural-gas direct-injection engine. *Fuel*, *89*, 752–759.

116. Karavalakis, G., Durbin, T. D., Villela, M., & Miller, W. (2012). Air pollutant emissions of light-duty vehicles operating on various natural gas compositions. *Journal of Natural Science and Engineering*, *4*, 8–16.

117. Karavalakis, G., Hajbabaei, M., Durbin, T. D., Johnson, K. C., Zheng, Z., & Miller, W. (2013). The effect of natural gas composition on the regulated emissions, gaseous toxic pollutants, and ultrafine particle number emissions from a refuse hauler vehicle. *Energy*, *50*, 280–291.

118. Hajbabaei, M., Karavalakis, G., Johnson, K. C., Lee, L., & Durbin, T. D. (2013). Impact of natural gas fuel composition on criteria, toxic, and particle emissions from transit buses equipped with lean burn and stoichiometric engines. *Energy*, *62*, 425–434.

119. McTaggart-Cowan, G. P., Reynolds, C. C. O., & Bushe, W. K. (2006). Natural gas fuelling for heavy-duty on-read use: current trends and future direction. *International Journal of Environmental Studies*, *63*(4), 421–440.

120. Yao, Y.-F. Y. (1980). Oxidation of Alkanes over Noble Metal Catalysts. *Industrial & Engineering Chemistry Product Research and Development*, *19*(3), 293–298. doi:10.1021/i360075a003

121. Carter, W. (1994). Development of Ozone Reactivity Scales for Volatile Organic Compounds. *Air & Waste*, *44*(7).

122. Lizarraga, L., Souentie, S., Boreave, A., George, C., D'Anna, B., & Vernoux, P. (2011). Effect of diesel oxidation catalysts on the diesel particulate filter regeneration process. *Environmental science & technology*, *45*(24), 10591–7. doi:10.1021/es2026054

123. Jeguirim, M., Tschamber, V., & Ehrburger, P. (2007). Catalytic effect of platinum on the kinetics of carbon oxidation by NO2 and O2. *Applied Catalysis B: Environmental*, *76*(3-4), 235–240. doi:10.1016/j.apcatb.2007.05.029

124. Stanmore, B. R., Tschamber, V., & Brilhac, J.-F. (2008). Oxidation of carbon by NOx, with particular reference to NO2 and N2O. *Fuel*, *87*(2), 131–146. doi:10.1016/j.fuel.2007.04.012

125. U.S. Energy Information Administration. (2013). *Annual Energy Outlook 2013*. Washington, DC. Retrieved from http://www.eia.gov/forecasts/aeo/pdf/0383(2013).pdf

126. Burch, R., & Loader, P. K. (1994). Investigation of Pt/Al2O3 and Pd/Al2O3 catalysts for the combustion of methane at low concentrations. *Applied Catalysis B: Environmental*, *5*(1-2), 149–164. doi:10.1016/0926-3373(94)00037-9

127. Subramanian, S., Kudla, R. J., & Chattha, M. S. (1992). Removal of methane from compressed natural gas fueled vehicle exhaust. *Industrial & Engineering Chemistry Research*, *31*(11), 2460–2465. doi:10.1021/ie00011a009

128. Subramanian, S., Kudla, R., & Chattha, M. S. (1993). Treatment of Natural Gas Vehicle Exhaust. *SAE International*, (930223). doi:10.4271/930223

129. Lyubovsky, M., Karim, H., Menacherry, P., Boorse, S., LaPierre, R., Pfefferle, W. C., & Roychoudhury, S. (2003). Complete and partial catalytic oxidation of methane over substrates with enhanced transport properties. *Catalysis Today*, *83*(1-4), 183–197. doi:http://dx.doi.org/10.1016/S0920-5861(03)00231-1

130. Oh, S. H., & Mitchell, P. J. (1994). Effects of rhodium addition on methane oxidation behavior of alumina-supported noble metal catalysts. *Applied Catalysis B: Environmental*. doi:10.1016/0926-3373(94)00034-4

131. Chin, Y. H., & Iglesia, E. (2011). Elementary steps, the role of chemisorbed oxygen, and the effects of cluster size in catalytic CH4-O2 reactions on palladium. *Journal of Physical Chemistry C*, *115*, 17845–17855. doi:10.1021/jp203324y

132. Epling, W. S., & Hoflund, G. B. (1999). Catalytic Oxidation of Methane over ZrO2-Supported Pd Catalysts. *Journal of Catalysis*, *182*(1), 5–12. doi:http://dx.doi.org/10.1006/jcat.1998.2341

133. Su, S. C., Carstens, J. N., & Bell, A. T. (1998). A Study of the Dynamics of Pd Oxidation and PdO Reduction by H2 and CH4. *Journal of Catalysis*, *176*(1), 125–135. doi:http://dx.doi.org/10.1006/jcat.1998.2028

134. Carstens, J. N., Su, S. C., & Bell, A. T. (1998). Factors Affecting the Catalytic Activity of Pd/ZrO2 for the Combustion of Methane. *Journal of Catalysis*, *176*(1), 136–142. doi:http://dx.doi.org/10.1006/jcat.1998.2029

135. Zhu, G., Han, J., Zemlyanov, D. Y., & Ribeiro, F. H. (2005). Temperature Dependence of the Kinetics for the Complete Oxidation of Methane on Palladium and Palladium Oxide. *The Journal of Physical Chemistry B*, *109*(6), 2331–2337. doi:10.1021/jp0488665

136. Chin, Y.-H., Buda, C., Neurock, M., & Iglesia, E. (2011). Selectivity of chemisorbed oxygen in C-H bond activation and CO oxidation and kinetic consequences for CH4-O2 catalysis on Pt and Rh clusters. *Journal of Catalysis*, *283*(1), 10–24. doi:http://dx.doi.org/10.1016/j.jcat.2011.06.011

137. Yamaguchi, A., & Iglesia, E. (2010). Catalytic activation and reforming of methane on supported palladium clusters. *Journal of Catalysis*, *274*, 52–63. doi:10.1016/j.jcat.2010.06.001

138. Fujimoto, K., Ribeiro, F. H., Avalos-Borja, M., & Iglesia, E. (1998). Structure and Reactivity of PdOx/ZrO2Catalysts for Methane Oxidation at Low Temperatures. *Journal of Catalysis*, *179*(2), 431–442. doi:http://dx.doi.org/10.1006/jcat.1998.2178

139. Zhang, T., Xin, Y., Ren, Z., Qi, F., & Law, C. K. (2013). Catalytic oxidation of methane over PdO in wire microcalorimetry. *Combustion and Flame*, *160*, 149–154. doi:10.1016/j.combustflame.2012.09.004

140. Wolf, M. M., Zhu, H., Green, W. H., & Jackson, G. S. (2003). Kinetic model for polycrystalline Pd/PdOx in oxidation/reduction cycles. *Applied Catalysis A: General*, *244*(2), 323–340. doi:http://dx.doi.org/10.1016/S0926-860X(02)00604-X

141. Datye, A. K., Bravo, J., Nelson, T. R., Atanasova, P., Lyubovsky, M., & Pfefferle, L. (2000). Catalyst microstructure and methane oxidation reactivity during the Pd↔PdO transformation on alumina supports. *Applied Catalysis A: General*, *198*(1-2), 179–196. doi:http://dx.doi.org/10.1016/S0926-860X(99)00512-8

142. Farrauto, R. J., Lampert, J. K., Hobson, M. C., & Waterman, E. M. (1995). Thermal decomposition and reformation of PdO catalysts; support effects. *Applied Catalysis B: Environmental*, *6*(3), 263–270. doi:http://dx.doi.org/10.1016/0926-3373(95)00015-1

143. Amin, A., Abedi, A., Hayes, R., Votsmeier, M., & Epling, W. (2014). Methane oxidation hysteresis over Pt/Al2O3. *Applied Catalysis A: General*, *478*, 91–97. doi:10.1016/j.apcata.2014.03.032

144. Schmidt, L. D., Huff, M., & Bharadwaj, S. S. (1994). Catalytic partial oxidation reactions and reactors. *Chemical Engineering Science*, *49*(24, Part A), 3981–3994. doi:http://dx.doi.org/10.1016/S0009-2509(05)80002-8

145. Bharadwaj, S. S., & Schmidt, L. D. (1995). Catalytic partial oxidation of natural gas to syngas. *Fuel Processing Technology*, *42*(2-3), 109–127. doi:http://dx.doi.org/10.1016/0378-3820(94)00098-E

146. Ozawa, Y., Tochihara, Y., Watanabe, A., Nagai, M., & Omi, S. (2004). Deactivation of Pt·PdO/Al2O3 in catalytic combustion of methane. *Applied Catalysis A: General*, *259*(1), 1–7. doi:http://dx.doi.org/10.1016/j.apcata.2003.09.029

147. Morlang, A., Neuhausen, U., Klementiev, K. V, Schütze, F. W., Miehe, G., Fuess, H., & Lox, E. S. (2005). Bimetallic Pt/Pd diesel oxidation catalysts: Structural characterisation and catalytic behaviour. *Applied Catalysis B: Environmental*, *60*(3-

4), 191–199. Retrieved from http://www.sciencedirect.com/science/article/B6TF6-4G0496C-1/2/77326cba371bbe8e5ae58e3b65061fb6

148. Persson, K., Ersson, A., Jansson, K., Fierro, J. L. G., & Jaras, S. G. (2006). Influence of molar ratio on Pd-Pt catalysts for methane combustion. *Journal of Catalysis*, *243*(1), 14–24. doi:http://dx.doi.org/10.1016/j.jcat.2006.06.019

149. Johns, T. R., Gaudet, J. R., Peterson, E. J., Miller, J. T., Stach, E. A., Kim, C. H., Balogh, M. P., & Datye, A. K. (2013). Microstructure of Bimetallic Pt-Pd Catalysts under Oxidizing Conditions. *ChemCatChem*, *5*(9), 2636–2645. Retrieved from 10.1002/cctc.201300181

150. Choi, J.-S., Partridge, W. P., & Daw, C. S. (2005). Spatially resolved in situ measurements of transient species breakthrough during cyclic, low-temperature regeneration of a monolithic Pt/K/Al2O3 NOx storage-reduction catalyst. *Applied Catalysis A: General*, *293*, 24–40. Retrieved from http://www.sciencedirect.com/science/article/pii/S0926860X05004850

151. Choi, J.-S., Partridge, W. P., Epling, W. S., Currier, N. W., & Yonushonis, T. M. (2006). Intra-channel evolution of carbon monoxide and its implication on the regeneration of a monolithic Pt/K/Al2O3 NOx storage-reduction catalyst. *Catalysis Today*, *114*(1), 102–111. doi:http://dx.doi.org/10.1016/j.cattod.2006.02.011

152. Choi, J.-S., Partridge, W. P., & Daw, C. S. (2007). Sulfur impact on NOx storage, oxygen storage, and ammonia breakthrough during cyclic lean/rich operation of a commercial lean NOx trap. *Applied Catalysis B: Environmental*, *77*(1-2), 145–156. Retrieved from http://www.sciencedirect.com/science/article/pii/S0926337307002226

153. Choi, J.-S., Partridge, W. P., Pihl, J. A., & Daw, C. S. (2008). Sulfur and temperature effects on the spatial distribution of reactions inside a lean NOx trap and resulting changes in global performance. *Catalysis Today*, *136*(1â€“2), 173–182. Retrieved from http://www.sciencedirect.com/science/article/pii/S0920586108000254

154. Partridge, W. P., & Choi, J.-S. (2009). NH3 formation and utilization in regeneration of Pt/Ba/Al2O3 NOx storage-reduction catalyst with H2. *Applied Catalysis B: Environmental*, *91*(1-2), 144–151. doi:http://dx.doi.org/10.1016/j.apcatb.2009.05.017

155. Forzatti, P., Lietti, L., & Gabrielli, N. (2010). A kinetic study of the reduction of NOx stored on Pt-Ba/Al2O3 catalyst. *Applied Catalysis B: Environmental*, *99*(1-2), 145–155. doi:http://dx.doi.org/10.1016/j.apcatb.2010.06.011

156. Choi, J.-S., Partridge, W. P., Pihl, J. A., Kim, M.-Y., Koci, P., & Daw, C. S. (2012). Spatiotemporal distribution of NOx storage and impact on NH3 and N2O selectivities during lean/rich cycling of a Ba-based lean NOx trap catalyst. *Catalysis Today*, *184*(1), 20–26. doi:http://dx.doi.org/10.1016/j.cattod.2011.11.007

157. Easterling, V., Ji, Y., Crocker, M., Dearth, M., & McCabe, R. W. (2012). Application of spaciMS to the study of ammonia formation in lean NOx trap catalysts. *Applied Catalysis B: Environmental*, *123-124*(0), 339–350. doi:http://dx.doi.org/10.1016/j.apcatb.2012.05.002

158. Michael, B. C., Nare, D. N., & Schmidt, L. D. (2010). Catalytic partial oxidation of ethane to ethylene and syngas over Rh and Pt coated monoliths: Spatial profiles of

temperature and composition. *Chemical Engineering Science*, *65*(12), 3893–3902. doi:http://dx.doi.org/10.1016/j.ces.2010.03.033

159. Shakir, O., Yezerets, A., Currier, N. W., & Epling, W. S. (2009). Spatially resolving concentration and temperature gradients during the oxidation of propylene on Pt/Al2O3. *Applied Catalysis A: General*, *365*(2), 301–308. Retrieved from http://www.sciencedirect.com/science/article/pii/S0926860X09004633
160. Al-Harbi, M., Radtke, D., & Epling, W. S. (2010). Regeneration of a model NOX storage/reduction catalyst using hydrocarbons as the reductant. *Applied Catalysis B: Environmental*, *96*(3-4), 524–532. doi:http://dx.doi.org/10.1016/j.apcatb.2010.03.014
161. Russell, A., Henry, C., Currier, N. W., Yezerets, A., & Epling, W. S. (2011). Spatially resolved temperature and gas species concentration changes during C3H6 oxidation over a Pt/Al2O3 catalyst following sulfur exposure. *Applied Catalysis A: General*, *397*(1-2), 272–284. Retrieved from http://www.sciencedirect.com/science/article/pii/S0926860X11001323
162. Luo, J.-Y., Al-Harbi, M., Pang, M., & Epling, W. S. (2011). Spatially resolving LNT desulfation: re-adsorption induced by oxygen storage materials. *Applied Catalysis B: Environmental*, *106*(3-4), 664–671. doi:http://dx.doi.org/10.1016/j.apcatb.2011.06.033
163. Abedi, A., Luo, J.-Y., & Epling, W. S. (2013). Improved CO, hydrocarbon and NO oxidation performance using zone-coated Pt-based catalysts. *Catalysis Today*, *207*(0), 220–226. doi:http://dx.doi.org/10.1016/j.cattod.2012.04.012

164. Hou, X., Schmieg, S. J., Li, W., & Epling, W. S. (2012). NH3 pulsing adsorption and SCR reactions over a Cu-CHA SCR catalyst. *Catalysis Today*, *197*(1), 9–17. doi:http://dx.doi.org/10.1016/j.cattod.2012.05.041

165. Harold, M. P., & Garske, M. E. (1991). Kinetics and multiple rate states of CO oxidation on Pt I. Model development and multiplicity analysis. *Journal of Catalysis*, *127*(2), 524–552. doi:10.1016/0021-9517(91)90182-4

166. Harold, M. P., & Garske, M. E. (1991). Kinetics and multiple rate states of CO oxidation on Pt II. Linking UHV and atmospheric pressure kinetic behavior. *Journal of Catalysis*, *127*(2), 553–575. doi:10.1016/0021-9517(91)90183-5

167. Eigenberger, G. (1978). Kinetic instabilities in heterogeneously catalyzed reactions—I. *Chemical Engineering Science*, *33*(9), 1255–1261. doi:10.1016/0009-2509(78)85091-X

168. Kevrekidis, I., Schmidt, L. D., & Aris, R. (1984). Rate multiplicity and oscillations in single species surface reactions. *Surface Science*, *137*(1), 151–166. doi:10.1016/0039-6028(84)90682-4

169. Bradley Shumbera, R., Kan, H. H., & Weaver, J. F. (2007). Oxidation of Pt(100)-hex-R0.7° by gas-phase oxygen atoms. *Surface Science*, *601*(1), 235–246. doi:10.1016/j.susc.2006.09.040

170. Kaneeda, M., Iizuka, H., Hiratsuka, T., Shinotsuka, N., & Arai, M. (2009). Improvement of thermal stability of NO oxidation Pt/Al2O3 catalyst by addition of Pd. *Applied Catalysis B: Environmental*, *90*(3-4), 564–569. Retrieved from http://www.sciencedirect.com/science/article/pii/S092633730900143X

171. Kinnunen, N. M., Hirvi, J. T., Suvanto, M., & Pakkanen, T. A. (2012). Methane combustion activity of Pd–PdOx–Pt/Al2O3 catalyst: The role of platinum promoter. *Journal of Molecular Catalysis A: Chemical*, *356*, 20–28. doi:10.1016/j.molcata.2011.12.023

172. Burch, R., & Urbano, F. J. (1995). Investigation of the active state of supported palladium catalysts in the combustion of methane. *Applied Catalysis A: General*, *124*(1), 121–138. doi:http://dx.doi.org/10.1016/0926-860X(94)00252-5